university of groningen / faculty of science and engineering / kapteyn astronomical institute

**Master's Thesis**

June 13, 2024

# 3DMTO – a source-extraction tool for optical IFU datacubes with the prospect of detecting Ly$\alpha$ emitters in the WEAVE Cosmological Clusters Survey

**Supervisors:**
Primary: Prof. Dr. Scott C. Trager
Secondary: Dr. Michael H.F. Wilkinson

**2nd Examiner:**
Prof. Dr. Reynier F. Peletier

**MSc thesis coordinator:**
Prof. Dr. Eline Tolstoy

**Student:**
Filip van der Mooren (S3804011)

**Abstract:** Over the coming years, the new large integral field unit (LIFU) from the William Herschel telescope Enhanced Area Velocity Explorer (WEAVE) will facilitate the unbiased serendipitous discovery of Ly$\alpha$ emitters (LAEs) in addition to the primary science objectives. Specifically faint LAEs are probed through lensing by galaxy clusters, from which the LAE luminosity function can be constructed. To detect and extract the LAEs from 3D IFU datacubes, we developed 3DMTO by adapting the 2D source-extraction tool max-tree objects (MTObjects) to 3D optical (L)IFU data. We additionally compute descriptive attributes for each detection. To evaluate the performance of 3DMTO, we compare its detections with a catalog produced from the same datacube of the MUSE eXtremely Deep Field. 3DMTO achieves a purity of 97.75 % over the whole catalog, but only detects about $\sim$ 30 % of the LAEs through Ly$\alpha$. Moreover, 3DMTO fails to recover a significant fraction of the flux for the LAEs it does detect. We found that 3DMTO is robust in the sense that the attributes of a detection do not depend on the detection parameter, and Ly$\alpha$ has distinguishing attributes with respect to the total sample of detections. Nevertheless, in its current state, 3DMTO is not suitable for detecting or extracting LAEs from IFU data.

# Contents

# List of Figures

**Page**

# List of Tables

**Page**

# 1 Introduction

The Lyman-$\alpha$ (hereafter Ly$\alpha$; Lyman, 1906) transition of hydrogen at 1215.67 Å with a photon energy of 10.2 eV is expected to intrinsically be the brightest emission feature for young actively star forming galaxies (SFGs) (Partridge & Peebles, 1967; Herenz, 2016). Partridge and Peebles theorized that high-redshift galaxies should be detectable by their strong Ly$\alpha$ emission, with luminosities up to $L_{\mathrm{Ly}\alpha} \sim 2 \times 10^{45}\,\mathrm{erg\,s^{-1}}$ at $z \sim 10 - 30$. This constitutes $\sim 6 - 7\,\%$ of a galaxies bolometric luminosity and may even be "boosted" to $\sim 20 - 40\,\%$ for specific initial mass functions and low metallicities at high redshift (Raiter et al., 2010).

Ly$\alpha$ occurs in emission when an ionized hydrogen atom de-excites from either the $2\mathrm{P}_{1/2}$ or $2\mathrm{P}_{3/2}$ to the $1\mathrm{S}_{1/2}$ ground state as a radiative doublet transition (Dijkstra, 2014). The mechanisms that facilitate these transitions are either collisions or recombination. Collisional excitation exchanges the kinetic energy of the free electron for a temporary excitation of the hydrogen atom that will subsequently emit a Ly$\alpha$ photon as "cooling" radiation. On the whole, collisionally excited Ly$\alpha$ emission is subdominant for galaxies but may become relevant at higher redshifts (Dijkstra, 2014). The most common production mechanism for Ly$\alpha$ emission is recombination, in which a hydrogen atom is excited to any permitted quantum state by capture of an electron, and subsequently emits a Ly$\alpha$ photon depending on the radiative cascade. For Ly$\alpha$-emitting galaxies, the physical conditions are generally such that $\sim 68\,\%$ of cascades result in Ly$\alpha$ emission, so called *Case B* recombination (Dijkstra, 2014). For case B recombination, there exists a balance between Ly$\alpha$ emission and absorption leading to resonant scattering (Herenz, 2016; Dijkstra et al., 2019).

In galaxies, Ly$\alpha$ is predominantly emitted through recombination in HII regions in the interstellar medium (ISM), unlike ultraviolet (UV)-continuum emission that originates in stellar atmospheres (Dijkstra, 2014). Ly$\alpha$ is so bright because the Lyman continuum (LyC) emission from O/B stars that ionize the HII regions is recycled into the Ly$\alpha$ through recombination (Partridge & Peebles, 1967; Herenz, 2016). Another significant source of LyC photons can be nuclear activity in active galactic nuclei (AGN), which undergo the same fate of being converted into Ly$\alpha$ (Ouchi et al., 2020). Ly$\alpha$ is also prevalently observed coming from the circumgalactic medium (CGM) or intergalactic medium (IGM) in the vicinity of galaxies through various processes (Dijkstra et al., 2019, Ch. 1), which may not directly correlate with stellar properties (Kerutt et al., 2022). Through resonant scattering, this emission manifests as a low surface brightness Ly$\alpha$ halo (LAH) around these galaxies. Ly$\alpha$ emitters (LAEs) are more formally defined in Section 1.1, but essentially represent galaxies that have considerable Ly$\alpha$ emission. Despite the predicted strong Ly$\alpha$ emissions, LAE remained elusive until the mid-1990s due to limited sensitivity of available telescopes and instruments at those times, and a likely overestimate of the brightest $L_{\mathrm{Ly}\alpha}$ an LAE can attain. The brightest non-AGN luminosity observed to date is $L_{\mathrm{Ly}\alpha} \simeq 10^{44}\,\mathrm{erg\,s^{-1}}$ (Marques-Chaves et al., 2020), more than an order of magnitude fainter than originally predicted.

In astronomy, sources and their components are often superimposed. This is because the 3D volume + spectral dimension imaged on the sky is projected down onto a 2D Charge Coupled Device (CCD), quantified by intensity. With a single photometric observation, one can only image the spatial extent on the sky and the spectral contents are lost. However, spectroscopy additionally retains the spectral dimension, which through redshift can also aid in recovering the distance. With integral field units (IFUs) (Bershady, 2010), one can construct a 3D hyperspectral datacube with two spatial dimensions (on sky) and a third spectral dimension. An unresolved source will then be represented by a 3D point spread function (PSF) that can be decomposed into a spatial 2D field spread function (FSF) and 1D spectral line spread function (LSF) (Figure 1.1).

LAEs can be searched for using various instruments like IFUs, slit spectroscopy, and the most popular method, photometric narrowband (NB) surveys, in which a narrow filter that covers a specific redshift is compared to a broadband filter (Pritchet, 1994). If there is an excess flux in the NB filter, the galaxy is strongly emitting within that spectral range, but spectroscopic follow up is always required to confirm which

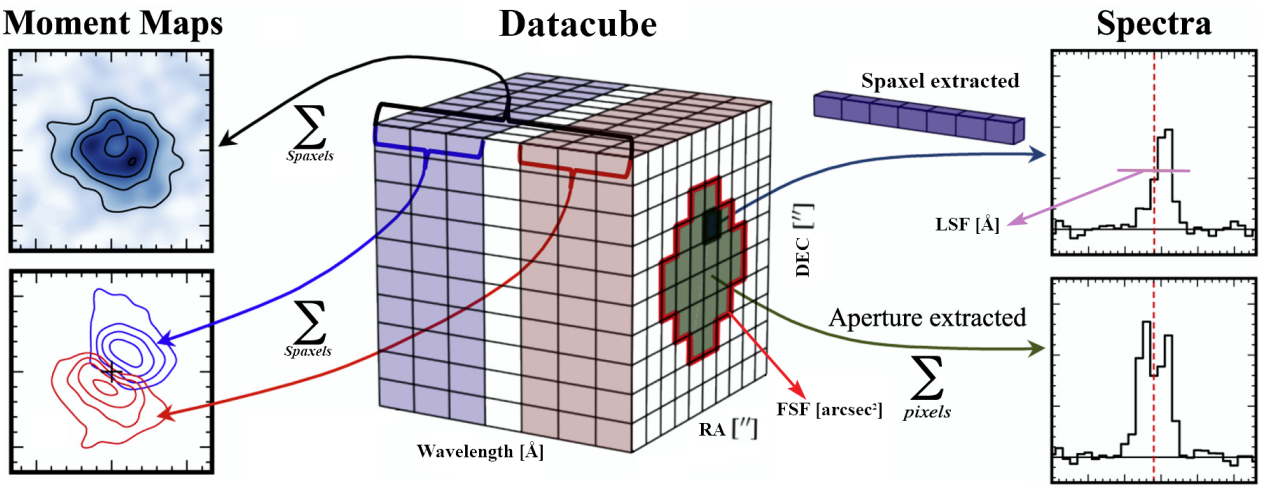


Figure 1.1: Illustrative explanation of a datacube. The **Datacube** (center) consists of a spectral wavelength axis and two spatial axes, namely the right ascension (RA) and declination (DEC). One cuboid in the datacube corresponds to a spatial–spatial–spectral resolution element, and is referred to as a voxel. A spaxel corresponds to the spectrum contained within a pixel. **Moment Maps** (left) integrate all spaxels over a certain range of the spectrum. The **Spectra** (right) are shown for a single spaxel (top) and integrated over an aperture (bottom) that corresponds FSF. The extent of the emission line along the spectrum (pink/purple horizontal line in top right panel) is referred to as the LSF, which combined with the FSF describes the 3D PSF of a signal in the datacube. The red dashed line coincides with the line center. (Figure adapted from Loomis et al., 2018).

emission line produces the excess. Moreover, NB surveys might miss flux if the part of the emission line falls outside of the transmission filter (Vieuville et al., 2019). NB surveys can cover large survey areas but are limited to redshifts within which the spectral window is not dominated by skylines, whereas spectroscopy can cover essentially the entire redshift range in between the skylines at high-enough resolution. Van Breukelen et al., 2005 were among the first to show the capability of blind IFU observations in the search for the elusive LAEs (Eisenhauer, 2010). The use of an IFU ensures that no flux is lost, whereas for slit based spectroscopy the aperture may not capture all the flux if the LAH is very extended (Vieuville et al., 2019; Lemaux et al., 2021) or offset with respect to the host galaxy (Lemaux et al., 2021). Moreover, when observing crowded regions like clusters, the slit aperture likely overlaps with multiple objects, blending their spectra. This may be mitigated somewhat by rotating the aperture, but remains difficult to avoid. In addition, compared to NB surveys, IFUs eliminate the need for spectroscopic follow-up, and can better filter out contaminants. Furthermore, the IFU's spatial information also enables it to search considerably larger survey areas compared to slit based spectroscopy, probing much more statistically significant co-moving volumes.

The 4.2 m William Herschel Telescope (WHT;[1] Boksenberg, 1985), located at the Observatorio del Roque de los Muchachos on La Palma, Spain,[2] was recently equipped with the wide-field spectroscopic WHT Enhanced Area Velocity Explorer (WEAVE;[3] Jin et al., 2024) instrument. WEAVE has an IFU mode and aims to complement current and upcoming major space- and ground-based programs in the Northern Hemisphere through eight independent surveys. The WEAVE Cosmological Clusters Survey (WCCS; Jin et al., 2024) – which main purpose is the study of galaxy evolution in cluster cores – provides an opportunity for serendipitous discovery of LAEs (through lensing) using the large IFU (LIFU) instrument mode. Serendipitous discovery is important to mitigate the bias from any sort of pre-selection.

In order to detect the LAEs within the datacube, we utilize Mathematical Morphology (Najman and Talbot, 2010; Serra, 2022; and references within both), introduced as a probabilistic framework in the 1960s to

[1] https://www.ing.iac.es/astronomy/telescopes/wht.
[2] https://www.iac.es/en/observatorios-de-canarias/roque-de-los-muchachos-observatory.
[3] https://www.ing.iac.es/weave.

efficiently provide quantitative analysis of geometrical structures. It quickly became applicable in binary image analysis, which shortly thereafter was extended to multiple dimensions and gray-scale morphology (Sternberg, 1986), and eventually generalized to a robust foundation in the algebraic theory of complete latices (Ronse, 1990). This foundation makes for a versatile theory, suitable for both continuous and discontinuous spaces (Najman & Cousty, 2014), with diverse applications in many disciplines like (medical) data visualization (Westenberg et al., 2007), feature extraction (Li et al., 2019) and image classification (Ghamisi et al., 2015) in geosciences, and astronomical object detection (Teeninga et al., 2016; Nguyen et al., 2021). For an overview see for example the book by Najman and Talbot, 2010.

For clarity, we make a distinction between a "source" and an "object". A source refers to an astrophysical emitter (e.g., an LAE) in its entirety, whereas an object *may* correspond to an entire astrophysical emitter, but also any prominent spatial–spectral emission component of said emitter (e.g., Ly$\alpha$ from an LAE). Formulated in the theory of Mathematical Morphology, a max-tree (Salembier et al., 1998) represents the datacube as an assortment of nodes, which either represent collections of regions as objects or noise, hierarchically ordered based on intensity. In this thesis we will adapt the 2D Max-Tree Objects (MTObjects or MTO;[4] Teeninga et al., 2013, 2016) object detection code to be applied 3D optical IFU datacubes. Haigh et al., 2021 compared commonly utilized 2D source-extraction tools, and have shown that MTObjects most accurately captures the fainter emission near the ambiguous boundaries commonly defining astrophysical sources. This property makes it compelling for the detection and extraction of faint diffuse emission lines like high redshift Ly$\alpha$ from LAEs.

## 1.1 Definition and characteristics of LAEs

In order to determine the LAE detection performance of 3DMTO, we need to describe what defines an LAE. The equivalent width EW(Ly$\alpha$) expresses the strength of the Ly$\alpha$ emission line as the ratio between the Ly$\alpha$ line flux, $F^{\text{line}}_{\text{Ly}\alpha}$ $\left[\text{erg s}^{-1}\,\text{cm}^{-2}\right]$, and the surrounding assumed constant UV continuum flux density, $f^{\text{cont}}_{\text{UV}}$ $\left[\text{erg s}^{-1}\,\text{cm}^{-2}\,\text{Å}^{-1}\right]$,

$$\text{EW(Ly}\alpha\text{)}\ \left[\text{Å}\right] = \int_{\lambda_0}^{\lambda_1} \frac{f^{\text{cont}}_{\text{UV}} - f^{\text{line}}_{\text{Ly}\alpha}(\lambda)}{f^{\text{cont}}_{\text{UV}}} \mathrm{d}\lambda \approx \frac{-F^{\text{line}}_{\text{Ly}\alpha}}{f^{\text{cont}}_{\text{UV}}} \qquad \text{for} \qquad f^{\text{line}}_{\text{Ly}\alpha} \gg f^{\text{cont}}_{\text{UV}}, \tag{1.1}$$

where $f^{\text{line}}_{\text{Ly}\alpha}(\lambda)$ $\left[\text{erg s}^{-1}\,\text{cm}^{-2}\,\text{Å}^{-1}\right]$ is the line flux density integrated over the spectral extent of the Ly$\alpha$ line from $\lambda_0$ to $\lambda_1$. In order to obtain the intrinsic equivalent width, we take the rest-frame EW: $\text{EW}_0(\text{Ly}\alpha) = \text{EW(Ly}\alpha)/(1+z_{\text{Ly}\alpha})$. There seems to be no strong consensus on what selection defines an LAE, but convention dictates an arbitrary $\text{EW}_0(\text{Ly}\alpha) \lesssim -20$ Å cut (Ouchi et al., 2020). LAEs are therefore not representative of a physical class of objects and moreover are biased towards high-redshift galaxies with high Ly$\alpha$ escape fractions along the line of sight (Östlin, 2009); but exceptions exist, with some researchers opting to make a different cut in $\text{EW}_0(\text{Ly}\alpha)$ (e.g. Ouchi et al., 2020; Kerutt et al., 2022).

Ly$\alpha$ inside LAEs originates from star forming regions and/or AGN activity (Dijkstra et al., 2019, Sec. 3.2.2), whereas once the Ly$\alpha$ photons escape to the CGM and IGM, Ly$\alpha$ is ubiquitously found to resonantly scatter, forming the low surface brightness LAH (Leclercq et al., 2017; Wisotzki et al., 2018; Kikuchihara et al., 2022; Niemeyer et al., 2022). The $\text{EW}_0(\text{Ly}\alpha)$ is intrinsically determined by the metallicity and star formation history of the LAE (Schaerer, 2003; Raiter et al., 2010). However, due to the various processes that may contribute Ly$\alpha$ photons and their radiative transfer, it is difficult to uncover which processes contributed to the observed EW(Ly$\alpha$) (Dijkstra et al., 2019). Recombination is expected to dominate within the galaxy, with collisional excitation possibly becoming important at higher redshifts (Dijkstra, 2014) and in the *in-situ* CGM (Mitchell et al., 2021).

[4] In this thesis we respectively refer to MTO and MTObjects as the technique and implementation presented in Teeninga et al., 2016, and 3DMTO as the version developed in this thesis for optical IFU data.

There appears to be a dichotomy in the population of LAEs, as they are either SFGs or AGNs (Konno et al., 2016; Spinoso et al., 2020), with a sharp transition at $2 \times L^*_{\mathrm{Ly}\alpha}$, where $L^*_{\mathrm{Ly}\alpha}$ is the "characteristic" luminosity (Sobral et al., 2018). LAEs below this transition are typically compact (half-light radius $\sim 1{-}2.5$ pkpc), young (age<100 Myr) SFGs with low dust content ($E(B-V) \sim 0-0.3$), low mass (stellar mass $\sim 10^8 - 10^9\,\mathrm{M}_\odot$), are metal poor ($Z \sim 0.1 - 0.3\,Z_\odot$), and have high stellar formation rates (SFRs), inhabiting the starburst region of the $\mathrm{M}_*$–SFR plane (see, e.g., Guaita et al., 2011; Nakajima et al., 2011; Bond et al., 2012; Matthee et al., 2021; Iani et al., 2023, and see Ouchi et al., 2020 for a review). These findings are largely corroborated by a recent study that stacked 50,000 LAEs at $\langle z \rangle \sim 2.6$ (Davis et al., 2023a). However, some LAEs may be older, with statistically different characteristics, populating the main-sequence in the $\mathrm{M}_*$–SFR plane as opposed to the starburst region (Iani et al., 2023).

At the time of the review by Ouchi et al., 2020, the number of LAEs, range of constrained luminosities, and maximum redshift was limited to $\gtrsim 1000$ (20000) spectroscopic (photometric) LAEs, $10^{41} \lesssim L^{\mathrm{SFG}}_{\mathrm{Ly}\alpha} \lesssim 10^{44}$, and $z = 8.68$ (Zitrin et al., 2015) respectively. Since then, drastic advancements have taken place with the onset of massive photometric and spectroscopic surveys that single-handedly push the number of detections far beyond prior findings, both photometrically (J-PLUS, 14564; Spinoso et al., 2020; SILVERRUSH, 20,567; Kikuta et al., 2023) and spectroscopically (HETDEX, $\sim$520K at $S/N > 5$; Weiss et al., 2024). Moreover, studies probed much fainter luminosities $\gtrsim 10^{39}\mathrm{erg\,s^{-1}}$ (Thai et al., 2023) and for the first time the higher-luminosity AGN regime $10^{43.5} \lesssim L^{\mathrm{AGN}}_{\mathrm{Ly}\alpha} \lesssim 10^{45.9}\,\mathrm{erg\,s^{-1}}$ (Spinoso et al., 2020; Liu et al., 2022). And with the advent of the *James Webb Space Telescope* (JWST), Ly$\alpha$ emission has even been observed in multiple sources out to $z \gtrsim 11$ (Bunker et al., 2023; Nakane et al., 2023). This is surprising given the belief that Ly$\alpha$ is expected to be absorbed by the highly neutral IGM at these redshifts, and instead favoring a patchy reionization of the Universe (Wise, 2019; Ouchi et al., 2020).

Nevertheless, the number of LAEs with "high" resolution spectra at high redshifts remain limited. This is where WEAVE and specifically WCCS can aid in serendipitously discovering such LAEs through lensing from galaxy clusters.

## 1.2 Origin of the Ly$\alpha$ line profile

The discovery of an LAE is dependent on the detected flux of the Ly$\alpha$ emission line. At the limiting temperature for which a HI cloud is neutral, assuming a column density of $N_{\mathrm{HI}} \approx 3{\times}10^{13}\,\mathrm{cm^{-2}}$, and ISM density of 1 atom per cubic cm, Ly$\alpha$ is already optically thick ($\tau(\mathrm{Ly}\alpha) \sim 1$) for a cloud diameter of just 2 AU (Hayes, 2015). A typical HII region has $N_{\mathrm{HI}} \sim 1.6 \times 10^{17}\,\mathrm{cm^{-2}}$ (Verhamme et al., 2015), and entire nearby galaxies commonly exhibit $N_{\mathrm{HI}} \sim 10^{19} - 10^{21}\,\mathrm{cm^{-2}}$, corresponding to $\tau(\mathrm{Ly}\alpha) \sim 10^7 - 10^8$ (Dijkstra et al., 2019). Additionally, noting that Ly$\alpha$ is completely absorbed by dust, the chance for which increases with more resonant scatters, Ly$\alpha$ photons have difficulty escaping their host galaxy. Nonetheless, escape is still made possible through geometric effects, or resonant scattering. Geometrically, the relative motion between the Ly$\alpha$ photon and the neutral HI medium can shift the absorption cross-section outside of the rest-frame wavelength of Ly$\alpha$, or Ly$\alpha$ may be scattered to a region of lower density and optical depth that allows it to escape (Hayes, 2015). Moreover, Ly$\alpha$ may also escape through the damping wings of the absorption profile where the cross-section is low, and the medium effectively becomes transparent (Osterbrock, 1962). This effect is very pronounced because the Ly$\alpha$ absorption cross-section is very large (Dijkstra et al., 2019), and common because the timescales of ground-state transitions are very short (Ouchi et al., 2020).

The escape of a Ly$\alpha$ photon may depend on many factors in the ISM like dust contents (Scarlata et al., 2009; Gazagnes et al., 2020), HI distribution and kinematics (Wofford et al., 2013), porosity (Gazagnes et al., 2020), galaxy viewing-angle (Smith et al., 2022; Blaizot et al., 2023), and many more (in)direct factors (Dijkstra et al., 2019, Sec. 4.7.2). Ly$\alpha$ close to the galaxy is either powered by star formation or an AGN, whereas in the LAH scattering dominates. Leclercq et al., 2020 found that properties of $\sim 40\,\%$ of Ly$\alpha$ lines in LAHs showed small-scale variation with respect to the galaxy core and/or within the LAHs themselves,

although Ly$\alpha$ line parameters remain largely consistent over the redshift range 3 – 6.

The resulting Ly$\alpha$ emission line morphology can thus be varied (Runnholm et al., 2021), but largely categorized into three groups: P Cygni profiles, singly-peaked, or doubly-peaked (see, e.g., Verhamme et al., 2006; Blaizot et al., 2023), with P Cygni profiles generally found in somewhat more evolved galaxies (Dijkstra et al., 2019). The complex radiative transfer makes it difficult to infer which intrinsic physical properties correspond to what Ly$\alpha$ line morphology (Dijkstra et al., 2019). Ly$\alpha$ lines and properties produced by radiative transfer models show a remarkable resemblance with observed profiles, but their parameters are difficult to relate to galaxies' physical conditions (Blaizot et al., 2023). Moreover, simulations have yet to produce realistic Ly$\alpha$ line profiles, owing to the requirement of high-resolutions in order to resolve the short Ly$\alpha$ mean-free path, yet also the need to account for physical effects at both the ISM and CGM scale (Blaizot et al., 2023).

This redistribution of Ly$\alpha$ photons in both space and frequency (Osterbrock, 1962) results in a complex Ly$\alpha$ line morphology which varies spectrally and spatially in the galaxy vicinity. The intrinsic single centrally peaked emission profile gets redistributed into two peaks by the ISM bluewards and redwards from the line center. The blue peak typically gets suppressed by the neutral CGM and IGM (Bosman et al., 2020) – which gets more pronounced with increasing redshift (Laursen et al., 2011; Gurung-López et al., 2020) – with the resulting observed line predominantly dominated by a red peak (Blaizot et al., 2023), as shown in Figure 1.2. When the blue peak dominates (Furtak et al., 2022; Mukherjee et al., 2023), it may indicate the presence of inflowing gas that is unresolved at current survey depths (Blaizot et al., 2023).

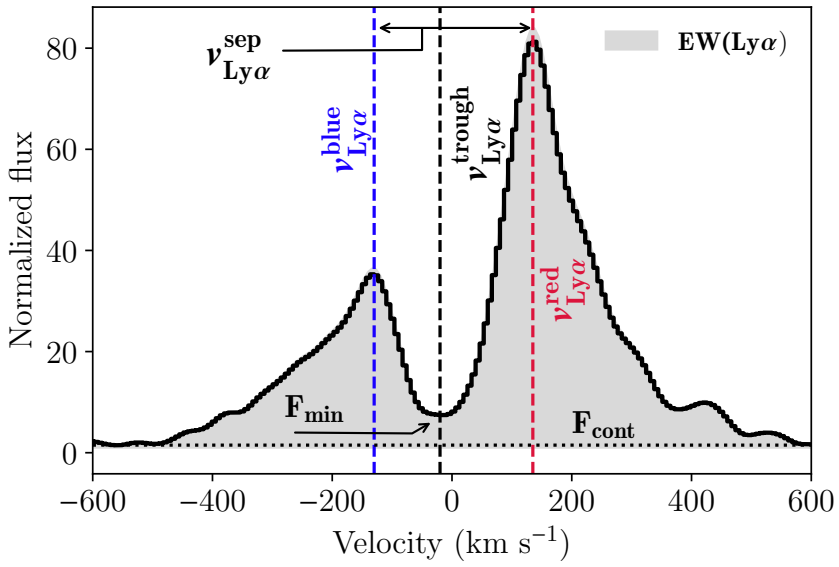


Figure 1.2: Taxonomy of the observed Ly$\alpha$ line morphology. The intrinsic single peak profile centered at 0 km s$^{-1}$ is resonantly scattered into two peaks at velocities $v^{blue}_{Ly\alpha}$ and $v^{red}_{Ly\alpha}$, separated by velocity $v^{sep}_{Ly\alpha}$. The minimum line flux $F_{min}$ defines the through velocity $v^{trough}_{Ly\alpha}$, which need not be at the intrinsic line center. The gray shaded region represents the equivalent width (EW(Ly$\alpha$); Equation 1.1), which is defined with respect to the continuum flux $F_{cont}$. (Figure from Gazagnes et al., 2020, © ESO 2020).

Even though the two peaks are spectrally offset with respect to the systemic redshift due to scattering, it remains possible to recover the systemic redshift (Verhamme et al., 2018). Moreover, its distinctive profile allows it to be distinguished from other emission lines when there is no other prominent lines to provide a confident redshift solution. A detection method does need to account for this distinctive nature, both spatially and spectrally, in order to adequately extract all the Ly$\alpha$ flux from a galaxy. Currently, 3DMTO may not capture all flux correctly because the two peaks are not connected, but 3DMTO could be adapted to detect the line as one (Section 6.5).

## 1.3 Science enabled by LAEs

The Ly$\alpha$ line harbors information about its environment through its resonant nature, and being so prevalent at virtually all redshifts makes it a very versatile tool that enables science on many scales (for a recent review see, e.g., Ouchi et al., 2020). LAEs specifically make up a considerable fraction of the galaxy population over a large redshift range, therefore making them important for both galaxy evolution and their contribution to (re)ionization of the Universe (Hayes, 2015; Ouchi et al., 2020).

This may be quantified through the LAE luminosity function (LF), the number of galaxies per co-moving volume as a function of luminosity. The LAE LF provides strong observational constraints on theoretical models of galaxy formation (Kobayashi et al., 2007) and cosmological simulations (Katz et al., 2023). Weinberger et al., 2018 recommend studying the *faint* end of the LAE LF, for it is a more robust tracer of the average ionization state of the IGM compared to the rapidly evolving environments seen in more massive halos. The following two subsections will elaborate on the (faint end) of the LAE LF and escaping ionizing radiation in the context of the WCCS.

### 1.3.1 LAE Luminosity Function

The most common parameterization of the LAE LF is a Schechter function (Schechter, 1976),

$$\phi(L_{\mathrm{Ly}\alpha})\ \left[\mathrm{Mpc}^{-3}\,\mathrm{dex}^{-1}\right] = \phi^*_{\mathrm{Ly}\alpha}\left(\frac{L_{\mathrm{Ly}\alpha}}{L^*_{\mathrm{Ly}\alpha}}\right)^{\alpha} \exp\left(-\frac{L_{\mathrm{Ly}\alpha}}{L^*_{\mathrm{Ly}\alpha}}\right) \mathrm{d}\left(\frac{L_{\mathrm{Ly}\alpha}}{L^*_{\mathrm{Ly}\alpha}}\right), \tag{1.2}$$

where $\alpha$ is the faint end slope of the LAE LF, and $\phi^*_{\mathrm{Ly}\alpha}$ and $L^*_{\mathrm{Ly}\alpha}$ are the characteristic number density and the luminosity of the "knee" of the LF respectively. The knee indicates a transition luminosity, before which the shape of the LF is governed by the faint end slope, and beyond which the exponential term becomes increasingly important.

It is important to know how the LAE LF evolves with redshift, for any evolution puts constraints on changes in galaxy formation and their properties (Kobayashi et al., 2007; Samui et al., 2009; Morales et al., 2021). The LAE LF is shown in Figure 1.3 for various redshifts and monotonically increases in the range $0 \lesssim z \lesssim 3$, is constant for $3 \lesssim z \lesssim 6$, and abruptly drops at higher redshifts, indicative of a late reionization history (Ouchi et al., 2020). LAEs with $L^*_{\mathrm{Ly}\alpha}$ at $z \gtrsim 2$ correspond to present-day dwarf galaxies (Ouchi et al.,

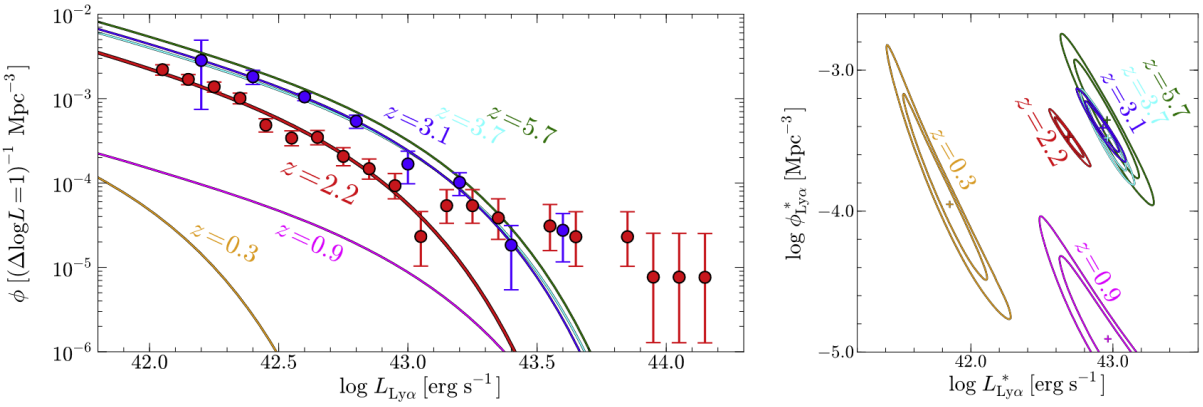


Figure 1.3: Left: LAE LFs with the solid curves representing best-fit Schechter functions derived with fixed $\alpha = -1.8$, corresponding to the best-fit faint end slope at $z = 2.2$. Right: uncertainty contours for the $\phi^*_{\mathrm{Ly}\alpha}$ and $L^*_{\mathrm{Ly}\alpha}$ Schechter parameters, where the inner and outer contours represent 68 % and 90 % confidence levels respectively. The data and parameters come from (Cowie et al., 2010; $z = 0.3$), (Barger et al., 2012; $z = 0.9$), (Konno et al., 2016; $z = 2.2$), (Ouchi et al., 2008; $z = 3.1$, 3.7, and 5.7) respectively. (Figure from Konno et al., 2016).

2020), whereas LAEs with $L_{\mathrm{Ly}\alpha}$ in excess of $L_{\mathrm{Ly}\alpha} \gtrsim 10^{43.3}$ erg s$^{-1}$ at $2.2 \lesssim z \lesssim 3.3$ almost exclusively host faint AGNs (Ouchi et al., 2008; Konno et al., 2016; Spinoso et al., 2020). These faint AGNs, which peak in number density in this redshift range, may provide considerable ionizing UV background radiation (Giallongo et al., 2015). At these redshifts, the faint AGNs manifest a bright end "Hump" in the LAE LF ($z = 2.2$ sample in Figure 1.3), which has since been upgraded to a turnover luminosity with opposite slopes at high $L_{\mathrm{Ly}\alpha}$ (Liu et al., 2022) and developed into a separate Schechter function (Spinoso et al., 2020). The Hump has been observed up to $z \sim 6.6$ (Matthee et al., 2015) but not confirmed to be dominated by faint AGNs, which would help better constrain their ionization contribution.

While a single Schechter does not provide a good fit over the entire luminosity range, Gronke et al., 2015 showed with their phenomenological model that it does provide a good fit for $10^{41} - 10^{44}$ erg s$^{-1}$ at $3 < z < 6$. Which is further corroborated by Herenz et al., 2019, who showed that three non-parametric methods were in excellent agreement with each other and the parametric Schechter function between $10^{42.2} \leq L_{\mathrm{Ly}\alpha}$ erg s$^{-1}$ $\leq 10^{43.5}$. Gronke et al. furthermore argue that a low luminosity turnover (at $10^{40} \lesssim L^{\alpha}_{\mathrm{Ly}\alpha}$ erg s$^{-1}$ $\lesssim 10^{41}$) – after which the LAE LF precipitously drops to zero – may correspond to a flattening of the UV LF of LBGs (at $-12 > M_{\mathrm{UV}} > 14$). In addition, they show that the faint end slope of LAE LF is steeper than that of the LBG UV LF, with a median $\alpha < -2.0$ at $z \gtrsim 4$.

The validity of these models are challenging to ascertain, as it is difficult to constrain the LAE LF for such low luminosities, yet large enough volume to get a handle on uncertainties. In the blank MUSE *Hubble* Ultra-Deep Field, the LAE LF has been probed down to $L_{\mathrm{Ly}\alpha} \gtrsim 10^{41.5}$ erg s$^{-1}$ for $2.9 \leq z \leq 6.9$ in 10 hours (30 hours in the deepest region) of integration (Drake et al., 2017), and even at 140 h there is likely still a significant fraction of LAEs that remain undetected (Bacon et al., 2023, hereafter BA23). Comparatively, using cluster fields with significant lensing, Vieuville et al., 2019 could constrain the LAE LF down to $L_{\mathrm{Ly}\alpha} \gtrsim 10^{40.5}$ erg s$^{-1}$ with maximum exposures of 7 hours. And more recently the LAE LF been probed down to $L_{\mathrm{Ly}\alpha} \geq 10^{39}$ erg s$^{-1}$ by observing 17 clusters for $\sim \langle 7 \rangle$ hours (15 hours maximum) (Thai et al., 2023). Thai et al., 2023 found their LAE LF agrees with blank field observations for $L_{\mathrm{Ly}\alpha} > 10^{42}$ erg s$^{-1}$ and obtain a redshift averaged faint end slope of $\alpha \sim -2$, as well as a significant flattening for $L_{\mathrm{Ly}\alpha} < 10^{41}$ erg s$^{-1}$. This is largely in line with Gronke et al., 2015, although Thai et al. does point out that Bouwens et al., 2022 ruled out a turnover trend for the UV LF for $M_{\mathrm{UV}} > -13.1, -14.3$ at $z \sim 3, 6$ respectively, noting that additional data is required to make any statistically significant inference of a turnover trend for the LAE LF.

This shows the power of IFUs in cluster fields at constraining the faint end slope. The WCCS may contribute to this by observing more than double the amount of clusters, probing a considerably larger co-moving volume, albeit with a brighter flux limit (Section 2.1).

### *Biases*

It is important to account for any bias that may affect the LAE LF in order to have any confidence in the inferred results. This can be quantified using a *selection function* $f_{\mathcal{S}}(\mathbf{q})$: the probability that an object (e.g., an LAE) with attributes $\mathbf{q}$ will end up in the final sample $\mathcal{S}$ (Rix et al., 2021). It can be decomposed into two parts: an initial characterization of the detection efficiency and corresponding completeness, followed by the sub-sample selection from all detections based on $\mathbf{q}$.

The first part is largely instrument and observation specific, whilst the subsequent step most certainly will depend on the detection method used. For emission line source detections in IFUs, the most important attributes are the wavelength of the detection and line flux, forming $f_{\mathcal{S}}(\lambda, F^{\mathrm{line}}_{\mathrm{Ly}\alpha})$ (Herenz, 2023). $f_{\mathcal{S}}(\lambda, F^{\mathrm{line}}_{\mathrm{Ly}\alpha})$ can be estimated empirically using insert and recovery experiments (Herenz et al., 2019), but detection methods that enforce a prior belief about what the signal looks like can utilize this to formulate an analytical expression for $f_{\mathcal{S}}(\lambda, F^{\mathrm{line}}_{\mathrm{Ly}\alpha})$. 3DMTO does not make any prior assumptions about what an LAE looks like, so will likely have to estimate the selection empirically. Recently Herenz, 2023 (LSDCat2.0, matched filtering) also presented a selection function that also accounts for the possible spatial–spectral template mismatch

compared to the idealized point source assumption. This is an important issue to consider, as failure to account for deviation from the point-source assumption results in an overestimation of survey depth, translating into underestimation of the LAE LF that is most pronounced at the faint end (Drake et al., 2017; Herenz et al., 2019).

Further aspects that may need to be accounted for are, e.g., the Eddington-Malmquist bias, lensing, IGM line of sight bias, and cosmic variance.

The Eddington-Malmquist bias results in more sources *scattering* into the sample $\mathcal{S}$ than out of it, artificially boosting the counts at the faint end of the luminosity range (Herenz et al., 2019). The authors further note that this bias has not been previously commented upon with regard to LAE LFs, but argue it has to be accounted for in order to robustly constrain the faint end slope.

An additional effect to account for at the faint end is magnification bias, in which the co-moving volume and number density are decreased and increased respectively (Loeb & Furlanetto, 2013; Richard et al., 2021b). The number densities may be increased as sources below the detection threshold are magnified to exceed said threshold. Concurrently, the solid angle within which a source is observed is spatially diluted, reducing the survey area and therefore co-moving volume. If the population of detected lensed galaxies is numerous – the case for the faint end of the LAE LF – the increased number density outweighs the spatial dilution, artificially boosting number densities (Loeb & Furlanetto, 2013).

Moreover, lensing galaxies obscure a considerable amount of spaxels that invalidate the background-limited assumption, from which the survey sensitivity is derived. For the spaxels that include these bright extended sources, the inverse variance (IVAR) contains contributions from the background, a superimposed continuum, the LAE's continuum, and the Ly$\alpha$ emission line of interest; whereas the same Ly$\alpha$ line in a background dominated region only contains IVAR contributions from the signal, the LAE continuum, and the background. These bright-source obscured spaxels should therefore be avoided in the determination of the LAE LF as their S/N is biased low, resulting in an underestimation of the LAE selection function (Herenz, 2023).[5]

The IGM line of sight bias refers to large scale variations in IGM properties that affect the transmission of Ly$\alpha$ photons, i.e., HI density and peculiar velocity with respect to Ly$\alpha$ photons. This bias can be diminished by observing regions of the Universe where the IGM conditions can be assumed independent of each other, such that they are marginalized out when combining the sample.

Cosmic variance (or rather sample variance) refers to the bias of over- or under-dense regions increasing or decreasing the number densities respectively (Loeb & Furlanetto, 2013). It is an additive uncertainty that predominantly becomes important at the faint end where it is relatively more important when compared with the Poisson uncertainty (Garel et al., 2016; Vieuville et al., 2019).

### 1.3.2 Implications of LAEs for the ionization state of the Universe

The debate is still ongoing as to which sources contributed (most) to reionization of the Universe at $z \gtrsim 6$, with likely contributors being both SFGs and AGNs (Wise, 2019). Based on simulations, LAEs can maintain the ionization state of the Universe after the epoch of reionization but are insufficient sources of ionizing radiation at $z \gtrsim 6$ (Yajima et al., 2014). On the other hand, Drake et al., 2017 found from observations that LAEs alone could conceivably maintain an ionized IGM at $z \approx 6$.

As LAEs are simply selected based on detectable Ly$\alpha$ emission, it is important to understand if they are fundamentally dissimilar to other SFGs at the same redshift without strong detections of Ly$\alpha$ (Ouchi et al., 2020). These galaxies are often Lyman-break galaxies (LBGs), characterized by a significantly diminished continuum blueward of Ly$\alpha$. Mori and Umemura, 2006 suggested based on "bottom up" simulations that post-starburst galaxies with ages of $10^9$ yr are LBGs and correspond to "the next phase of LAEs", finding their fully evolved ($z = 0$) properties to be consistent with nearby ellipticals. Later simulations found that LAEs are

[5] Similar to bright sources, along the wavelength direction skylines will locally affect the selection function.

likely merely a subset of LBGs, and depending on the selection of EW(Ly$\alpha$) and $M_{\rm UV}$ may even correspond to the same group of galaxies (Dayal & Ferrara, 2012). Using JWST data, it has more recently been reported that LAEs and LBGs are essentially statistically the same at $z \sim 2.8 - 6.7$ (Iani et al., 2023). In addition, they found that 48 % of their LBGs are starbursts with ages $< 10$ Myr, but contain no detectable Ly$\alpha$, which the authors suggest may be attributed to dust-selective extinction and/or resonant scattering due to a high HI column density (Ouchi et al., 2020), and not necessarily an intrinsic lack of Ly$\alpha$ emission. Moreover, Samui et al., 2009 note that in order to reproduce the LAE LF at high redshift ($z > 5$), their semi-analytical model requires nearly all LBGs to be LAEs, whereas at $z \lesssim 4$, 10 % suffices.

For galaxies to contribute to the ionization of the IGM, their ionizing photons must escape into the IGM. The Ly$\alpha$ escape fraction $f_{\rm esc}^{\rm Ly\alpha}$ is defined as the ratio of the observed Ly$\alpha$ stellar formation rate density ($\rm SFRD_{Ly\alpha}$) over that intrinsically produced,[6] for which the $\rm SFRD_{UV}$ may be taken as a proxy (Hayes et al., 2011). Interestingly, $f_{\rm esc}^{\rm Ly\alpha}$ gradually increases by 2 dex in the range $z \sim 0-6$, likely attributable to a decreasing HI column density towards higher redshift that reduces resonant scattering (Konno et al., 2016). The SFRD is obtained from the luminosity density (LD) through the luminosity–SFR relation. The luminosity density (LD) is obtained by integrating the LF multiplied by the luminosity over the luminosity range, typically from the faintest $L_{\rm Ly\alpha}$ constrained up to infinity. The AGN population is only relevant at high luminosities, such that their contribution to the SFRD is negligible. It is the low luminosity regime, especially the faint end slope, that has a significant impact on the SFRD. To maintain the ionization state of the IGM at a given redshift, a critical SFRD needs to be met, which depends on the escape of UV photons (Thai et al., 2023). Thai et al., 2023 recently showed that by better constraining the faint end of the LAE LF, LAEs may contribute to the ionization state of the Universe significantly more than previously believed.

The WCCS may aid in probing and constructing the (fain end) LAE LF, but its resulting spectra are rich in information as well. The integration time will not be sufficient to reach high enough S/N to qualitatively study the spectrum of an individual LAE, but they may be stacked to infer cosmic averages and/or population properties (Nakajima et al., 2018; Ribeiro et al., 2020; Davis et al., 2021; Naidu et al., 2022; Davis et al., 2023a), which are ultimately of more relevance to determining the contribution of the LAE population to the ionization state of the Universe. Moreover, it has been reported that galaxies which strongly leak LyC photons are also LAEs (Flury et al., 2022).

## 1.4 Prior detection & extraction techniques

Astronomy has long been concerned with the automated detection of sources to empower scientists in their analysis (see, e.g., Masias et al., 2012, for a review). Masias et al. compiled a thorough list of the detection techniques utilized for various astronomical data, the most common of which were thresholding and local peak search. In IFU datacubes, the number of resolution elements is significantly increased, with too many voxels in a single datacube ($\gtrsim 10^8$ voxels) for the (too few) experts to manually sift through every datacube (Fluke et al., 2017). Besides exemplifying the need for automated source detection techniques, the relatively high spatial and spectral resolution of datacubes imply that the same source is spread out over many voxels, making traditional thresholding approaches impractical (Jurek, 2012).

A more refined thresholding approach could be obtained using, e.g., region-based mathematical morphology (e.g., trees) that consider the pixel connectivity at each gray-level in the image. The connected component tree is used by Perret et al., 2010 and Berger et al., 2007 for astronomical source detection on 2D astronomical images and also more recently by Nguyen et al., 2021 for source detection in astronomical multi-band images.

The original MTObjects code is a 2D max-tree based object detection program utilizing a statistical test. MTO does not make any assumption about the signal but simply detects if there are regions in the data that are significantly dissimilar to the expected noise distribution. MTObjects predominantly improved segmentation

[6] An equally valid definition would be $f_{\rm esc}^{\rm Ly\alpha} = L_{\rm Ly\alpha}^{\rm obs} / L_{\rm Ly\alpha}^{\rm int}$.

of fainter extended features compared to other tools (Haigh et al., 2021), like the commonly utilized Source Extractor (or SExtractor; Bertin & Arnouts, 1996). MTO has been extended to multiband images (Nguyen et al., 2021; Faezi et al., 2024) and 3D radio datacubes with early results obtained by Moschini et al., 2014 and later using a more appropriate statistical treatment (Arnoldus, 2015; Barkai et al., 2023). However, Arnoldus' implementation of MTO is specific to radio data and not immediately transferable to the optical due to the different, non-Gaussian, noise properties in radio data (see, e.g., Kazemi & Yatawatta, 2013) compared to the optical (Arnoldus, 2015). We aim to adapt MTO to be used for optical IFU datacubes.[7]

Herenz, 2023 mention that at the time of writing the only freely available tools for object detection in IFU datacubes were ORIGIN (Mary et al., 2020), employing a Generalized Likelihood Ratio approach; the "Source Emission Line Finder" (SELFI; Meillier et al., 2016), a Bayesian method; the "MUSE Line Emission Tracker" (MUSELET; Piqueras et al., 2019), a SExtractor based approach; and their own "Line Source Detection and Cataloguing Tool" (LSDCat(2.0); Herenz & Wisotzki, 2017; Herenz, 2023), a matched filtering approach. These methods are predominantly geared towards specifically detecting (faint and/or compact) emission line sources. Herenz, 2023 also mentioned CubEx (Cantalupo et al., 2018), a code available upon request, as stated in the "code availability" remark in Ginolfi et al., 2022, who showed that CubEx can be configured not only to detect diffuse extended emission (its main purpose), but is also able to detect emission line sources. Whereas MTO makes no a priori assumptions about the morphological voxel representation of a source, none of the aforementioned tools can detect both compact and extended emission sources (in one run) – which can be desirable considering how time-consuming it is to process an entire datacube. MTO achieves this by not discriminating between real sources and artifacts (e.g., cosmic rays or skyline residuals), marking any region found to be statistically significant as a detection, which can be problematic; MTO is also susceptible to detecting blended sources at similar intensity as one detection (Teeninga et al., 2016). Moreover, tools like ORIGIN and LSDCat can also detect absorption features, which MTO currently cannot. Section 6.5 discusses how MTO could be adapted to also handle the absorption case.

Given the ubiquitous nature of LAHs around LAEs, one has to consider if the compact assumption some of the aforementioned tools make may hinder the detection of LAEs, especially when considering that an LAH on average contains 65 % and up to 90 % of the total Ly$\alpha$ flux of an LAE (Leclercq et al., 2017). Mary et al., 2020 note that the surface brightness of the halo component is approximately 2 magnitudes lower than the core component outside of the FSF of the Multi Unit Spectroscopic Explorer at the Very Large Telescope (VLT/MUSE; Bacon et al., 2010), implying that the point-source assumption is unlikely to significantly impede the detection of LAEs. However, the point-source assumption may become an issue when having to extract all the flux belonging to an LAE, which is only exacerbated when considering that many of the LAEs to be detected in the WCCS will be lensed, and LAEs that span sizes larger than the FSF are not uncommon (Richard et al., 2021b, Sec. 5.4).

MTO differs from the aforementioned IFU detection techniques by directly inferring source characteristics like the flux and derived signal-to-noise (S/N or SNR) from the voxel segmentations of the detections instead of a subsequent spectral fitting extraction procedure that may miss extended emission (BA23 Sec. 5.8.1). In 2D, MTO has been shown to recover flux comparable to SExtractor, but the results in Section 5.2 show 3DMTO currently underestimates the flux.

## 1.5 Thesis structure

The prior sections are summarized to formulate the following research goals and questions:

- What are the prospects of detecting LAEs in the WCCS?
- Adapt MTO to 3D optical IFU data, referred to as 3DMTO.

[7] We refer to this implementation of MTO as 3DMTO.

- Can 3DMTO detect and appropriately extract the Ly$\alpha$ emission line?
- Can 3DMTO be used to robustly detect LAEs in the WCCS?

These questions and goals will be considered in the subsequent chapters. In Chapter 2 the data obtained from the WCCS will be detailed, as well as an estimate on the number of LAEs to expect is presented. Chapter 3 provides the theoretical background required for the max-tree, as well as the in Chapter 4 presented detection method and computed attributes. Subsequently, Chapter 5 compares the detections of Ly$\alpha$ by 3DMTO with the catalog of the MUSE eXtremely Deep Field (MXDF; BA23) built from the same datacube. In Chapter 6 we discuss many aspects of the method and data, as well as the results derived from it. And finally, Chapter 7 concludes the thesis and suggests future research possibilities.

Throughout this thesis, we define an LAE as a galaxy with $\mathrm{EW}_0(\mathrm{Ly}\alpha) \lesssim -20$ Å; pkpc, and cMpc, cGpc, correspond to proper and co-moving distances respectively; the word "catalog" exclusively refers to the catalog from BA23 and the word "detection" will be used to indicate 3DMTO detections, unless specified otherwise; and all WEAVE datacubes used were processed using provisional calibration.[8] We adopt the flat *Planck 2018* cosmology with $H_0 = 67.66\,\mathrm{km\,s^{-1}\,Mpc^{-1}}$, $\Omega_m = 0.3111$, $\Omega_\Lambda = 0.6889$ (Planck Collaboration et al., 2020),[9] made available in Python by the Astropy Collaboration et al., 2013, 2018, 2022.

[8] Datacubes built using initial calibration from data taken within the following timeframe 2022/10/25–2023/05/17.

[9] The *exact*, and full list of parameters are those from their *TT, TE, EE + lowE + lensing + BAO* dataset, presented in their Table 2.

# 2 WEAVE Cosmological Clusters Survey

WEAVE has three instrumental modes: multi object spectroscopy, 20 mini-IFUs, and the WEAVE LIFU, all shown in Figure 2.1. The WEAVE LIFU utilizes $\sim$ 550 fibers for a $78'' \times 90''$ field of view, feeding a dual-beam spectrograph through "BLUE" and "RED" arms, respectively corresponding to a wavelength coverage of $\sim 3600 - 5955$ Å and $\sim 5820 - 9490$ Å as shown in Figures 2.2–2.4. The WCCS will use all three of WEAVE's instrument modes, but only data from the WEAVE LIFU will be considered in this thesis. The WEAVE LIFU data is reconstructed into a 3D spatial–spatial–spectral datacube (Section 6.3).

## 2.1 WCCS description and the WEAVE LIFU

The WCCS primary goal is the study of galaxy evolution in cores of cluster in addition to constraining cosmological parameters and global scaling relations. The main targets are $\sim$ 70 Sunyaev-Zeldovich (SZ) effect-selected clusters, of which $\sim$ 40 will be observed using the WEAVE LIFU in the redshift range $0.2 \lesssim z \lesssim 0.5$ (Trager & The WEAVE Science Team, 2019). We aim to evaluate the serendipitous detection potential of (lensed) LAEs using the same data to construct the LAE LF and infer their (Ly$\alpha$) escape fractions.

WCCS will use the WEAVE LIFU in the low resolution mode (Table 2.1) with at least three dithers to obtain full sky coverage in the field of view as the LIFU only has a 55 % filling factor (Jin et al., 2024). The

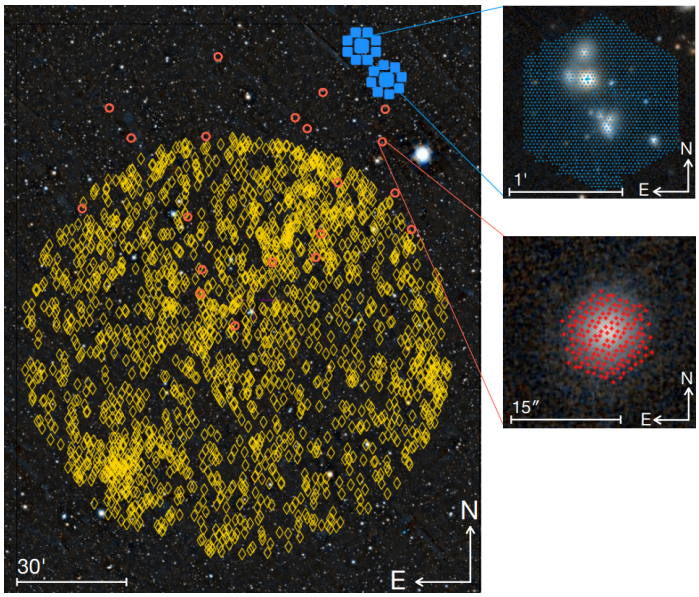


Figure 2.1: The three observing modes of the WEAVE Clusters Survey are shown overlaid on top of an image of the Abell 2142 galaxy cluster. Layer 1 (◇): the WEAVE Nearby Clusters survey using the MOS and mIFU modes in LR. Layer 2 (○): the WEAVE Wide Field Cluster survey utilizes WEAVES's MOS mode in LR. **Layer 3** (■): the Cosmological Clusters survey using the WEAVE **LIFU** in LR. (Figure from Jin et al., 2024).

WEAVE LIFU has a $1''.6$ FSF over the entire wavelength range when dithered with the standard patterns and an LSF full width half maximum (FWHM) of 1.7 Å and 2.75 Å in the RED and BLUE arms respectively (Section 6.3).

Even though LAEs can be spatially extended, at the redshift considered here and the spatial resolution of the WEAVE LIFU, LAEs are essentially point sources. The majority of the flux may be in the halo component but will nevertheless generally be contained within the WEAVE LIFU FSF, as the flux is already contained within MUSE's considerably smaller FSF (Mary et al., 2020). While spatially LAEs are unresolved,

Table 2.1: WCCS LAE relevant science details using the WEAVE LIFU instrument in LR mode.

| WCCS & WEAVE LIFU parameters | | inferred LAE detectability prospects[a] | |
|---|---|---|---|
| Exposure time[b] | 2 h, 4 h | LIFU observed clusters | $\sim 40$ |
| Resolving power $R$ | $\sim 2500$ | fields per cluster | $\langle 1.5 \rangle$ |
| Wavelength coverage[c] | $\sim 3600 - 9490$ Å | LIFU survey area | $\sim 0.025\,\mathrm{deg}^2$ |
| SZ LIFU cluster redshift range | $0.2 \lesssim z \lesssim 0.5$ | LIFU co-moving volume | $\sim 1.3 \times 10^6\,\mathrm{cMpc}^3$ |
| Ly$\alpha$ redshift range | $2.0 \lesssim z \lesssim 6.8$ | Estimated number of LAEs | $\sim 144$ |
| LIFU Field of view | $78'' \times 90''$ | | |

Survey specific details were obtained from Trager and The WEAVE Science Team, 2019.

[a]Note that the inferred quantities ignore any lensing effects.

[b]2 h at lowest redshifts and 4 h at highest redshifts.

[c]There are two small gaps in the spectrum shown in Figures 2.2–2.4.

the spectral resolution of the WEAVE LIFU should allow it to distinguish real emission between sky lines (Bershady, 2010), as well as to discern Ly$\alpha$ spectral features to some degree (e.g., differentiate the blue and red peaks, Runnholm et al., 2021). Moreover, the large wavelength coverage of the WEAVE LIFU greatly alleviates source confusion (with, e.g., H$\alpha$, H$\beta$, [O III]), as many spectral features will be available to determine the redshift of low redshift interlopers (Loeb & Furlanetto, 2013), whereas a high redshift LAE will predominantly only be detectable through Ly$\alpha$ emission (at WCCS's exposure time). A more challenging contaminant could be the [O II] emission line, which appears spectrally isolated similar to Ly$\alpha$ (Nakajima et al., 2018; Davis et al., 2023b), but the [O II] doublet may be resolved and identified by the WEAVE LIFU if the velocity dispersion is low enough (Comparat et al., 2013). Even if the WEAVE LIFU's resolving power is enough to discern Ly$\alpha$ spectral features, the limited exposure time of the WCCS may not provide sufficient S/N for the detailed study the line profile (Weiss et al., 2024), which can however still be studied through stacking (Davis et al., 2023a).

### 2.1.1 Survey limits

We preface this discussion by mentioning that current availability of WEAVE LIFU datacubes is limited at the time of writing, and those available are preliminary with final sensitivity limits that will differ from those reported here.[10] Moreover, as the targets of the WCCS are dense cluster cores, finding any region within the datacubes truly devoid of signal is challenging. Once more datacubes with final calibration are available, more refined survey limits may be determined.

To estimate the $5\sigma$ surface brightness limit, we integrate a $1''$ x $1''$ region binned to 1 Å in the IVAR datacube, take the square root and subsequently multiply by 5. The limiting surface brightness is shown in Figure 2.2, in addition to the limits for MUSE and PMAS/PPak[11] at nominal wavelengths for comparison, scaled to match the WCCS exposure time. The procedure for the $5\sigma$ limiting line flux (Figure 2.3) is largely the same, except that we now integrate over a $2\farcs0$ x $2\farcs0$ region, binned to 2 Å and 3 Å for the BLUE and RED arms respectively. The difference in the wavelength direction arises from the fact that the FWHMs of the LSF in the BLUE and RED arm differ. The $5\sigma$ line flux limit is determined as a conservative estimate because the FSF drops precipitously beyond $1\farcs6$ (Section 6.3).

Even though LAEs are not the main survey target, the 3D nature of IFUs facilitate serendipitous discovery, as no preselection is required. Under the assumption of spatially and spectrally unresolved LAEs, we can use the luminosity distance to determine the $5\sigma$ limiting luminosity at which an LAE is still detectable as a function of redshift from the limiting line flux (Figure 2.4). Over the majority of the Ly$\alpha$ redshift range, the

[10]The flux calibration has been improved since the "V2" datacubes used here.

[11]The precursor to WEAVE's LIFU on the 3.5 m Calar Alto telescope.

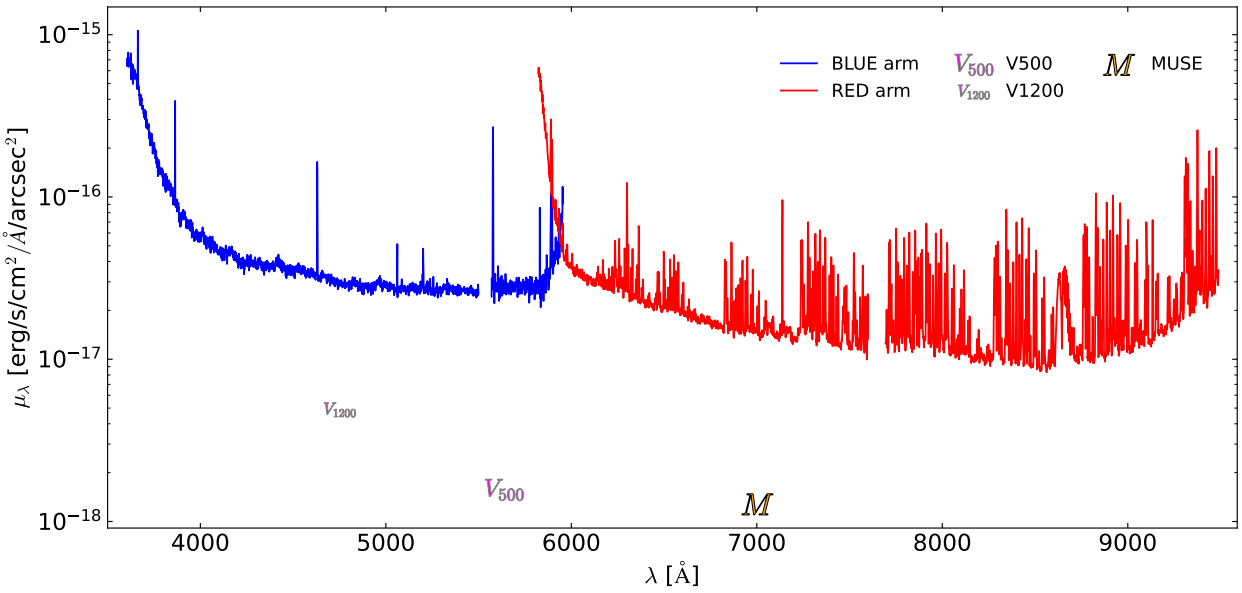


Figure 2.2: $5\sigma$ sky noise surface brightness limit measured in an empty region of the sky, for WEAVE LIFU `stackcube_3006749.fit` (BLUE arm) and `stackcube_3006748.fit` (RED arm) respectively. The limits of MUSE (Richard et al., 2021b) and V500/V1200 (PMAS/PPak; Husemann et al., 2013) are scaled to match the exposure time of the 1020 s exposure time of the WEAVE LIFU data, assuming $\mu_\lambda$ scales with the square root of the exposure time.

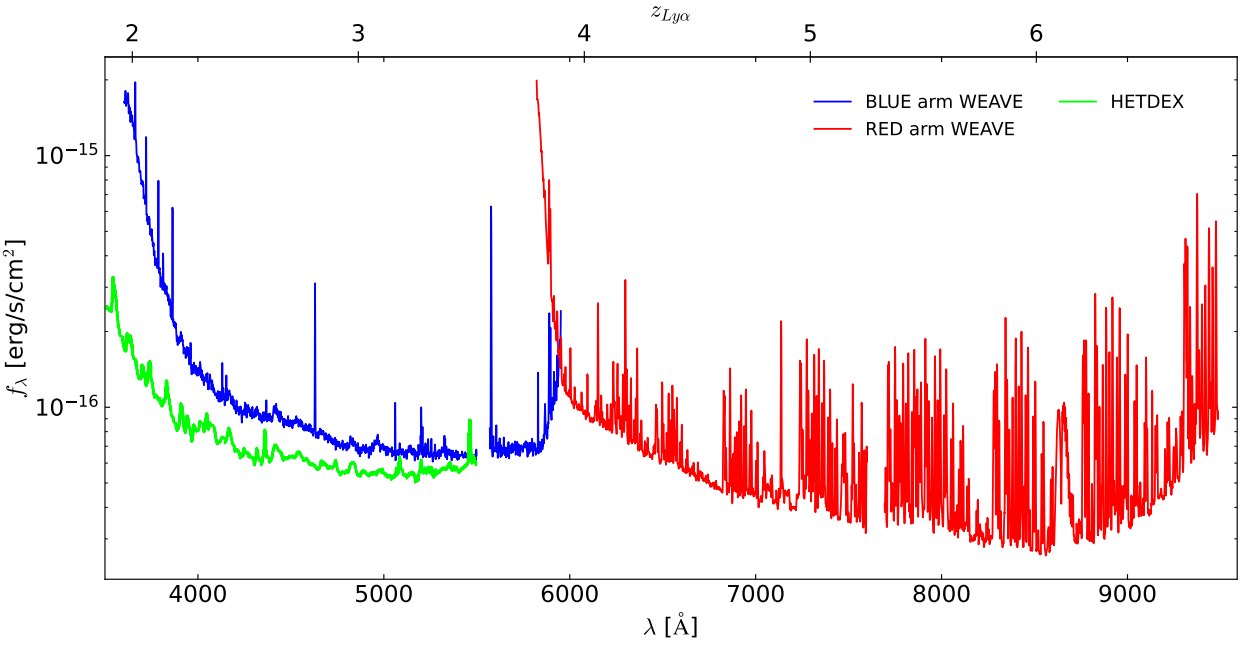


Figure 2.3: The $5\sigma$ line flux limit, integrated over $2''.0$ x $2''.0$ by 2 Å (BLUE arm) and 3 Å (RED arm) apertures, for WEAVE LIFU `stackcube_3006749.fit` and `stackcube_3006748.fit` respectively. The green curve is the HETDEX $5\sigma$ sky noise flux per spectral resolution element for a 360 s exposure (adapted from Hill et al., 2021), scaled such that the minimum is at $5 \times 10^{-17}$ erg s$^{-1}$ cm$^{-2}$, their faintest detectable line under good conditions.

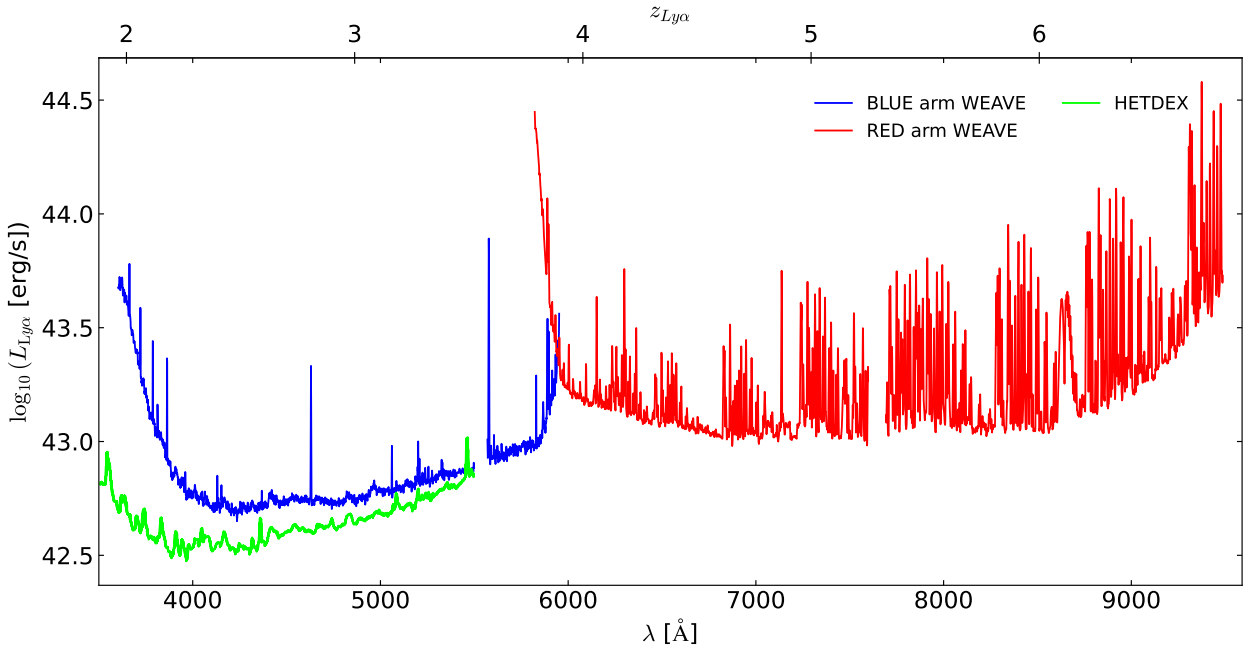


Figure 2.4: The $5\sigma$ limiting luminosity, corresponding to the $5\sigma$ limiting line flux of Figure 2.3, for WEAVE LIFU `stackcube_3006749.fit` (BLUE arm) and `stackcube_3006748.fit` (RED arm) respectively. The green curve is the HETDEX limiting luminosity obtained via the corresponding limiting line flux presented in Figure 2.3 (adapted from Hill et al., 2021).

lowest luminosity reached is $L_{\mathrm{Ly}\alpha} \gtrsim 43\,\mathrm{erg\,s^{-1}}$. Additionally, noting that the sensitivity response function of the WEAVE LIFU is not particularly flat, especially flaring up near the edges for both arms, the WCCS is thus limited to the bright end of the LAE LF. However, the faint end may be probed by the unquestionable existence of lensed LAEs when observing cluster cores (Vieuville et al., 2019). Moreover, LAEs dominate the redshift distribution of lensed background galaxies (Richard et al., 2021a), and multiply-imaged LAEs are expected to occur in high density at $1.9 < z < 4$ (Richard et al., 2021b). Although WEAVE covers most of this redshift range, Figure 2.4 shows that the sensitivity steeply decreases by $\sim 1$ dex in luminosity at the lowest redshift compared to the rest of this redshift range. Nonetheless, going into bluer wavelengths closer to cosmic noon considerably increases the number of LAEs, because the luminosity distance is lower, fainter LAEs are more numerous, and the wavelength is relatively devoid of sky-lines (Richard et al., 2021a).

## 2.2 Survey comparison

The exposure time of 1020 s assumed for the survey limits is the effective exposure time of most spaxels, but for some spaxels may be a factor two or three higher owing to the dither strategy (Section 6.3.1). Moreover, a nominal WCCS observation will have a total exposure time of 2 h or 4 h depending on the redshift (Trager & The WEAVE Science Team, 2019), as opposed to the 3060 s total exposure time for the datacubes used to specify the aforementioned survey limits, which effectively serve as lower limits. This makes any direct comparison to other surveys difficult as the effective exposure time of a single source can vary within the FSF.

The eventual goal of determining the LAE LF and inferring ionizing radiation escape fractions from observed lensing clusters is best compared with Vieuville et al., 2019 and Thai et al., 2023, who used MUSE to observed four and seventeen lensing clusters, finding 156 and 600 LAEs, respectively. However, our aim of finding LAEs in WCCS data is most comparable to Richard et al., 2021b, who used MUSE to observe twelve massive lensing clusters, covering $\sim 23$ arcmin$^2$, albeit at a significantly longer exposure time on a larger

telescope and therefore correspondingly lower $5\sigma$ flux limit of $\sim 1 \times 10^{-18}$ erg s$^{-1}$ cm$^{-2}$ at 7000 Å. Richard et al. detected 3300 robust redshifts, of which a considerable $\sim$ 30 % are lensed LAEs. Where the WCCS will not come close to the same flux limit, the increased wavelength coverage, especially into the blue, and covering $\sim$ 3.8x the survey area may result in a comparable amount of (lensed) LAEs. Moreover, WCCS targeting clusters better visible from the Northern Hemisphere, complement MUSE located in the Southern Hemisphere, further mitigating any IGM line of sight bias.

In a single WEAVE LIFU pointing (3 dithers minimum), a cosmological co-moving volume of $\sim 2.2 \times 10^4$ cMpc$^3$ for LAEs is probed. This is roughly a factor two larger than MUSE's $\sim 1.0 \times 10^4$ cMpc$^3$ in one exposure. The total LIFU survey area and wavelength coverage corresponds to a co-moving volume of $\sim 1.3 \times 10^6$ cMpc$^3$ (Table 2.1).

The HETDEX survey (Gebhardt et al., 2021) uses the Visible Integral-field Replicable Unit Spectrograph (VIRUS) instrument (Hill et al., 2021) with the singular purpose of observing a $\sim$ 1 million LAEs by survey end, covering an unprecedented spectroscopic co-moving volume of 10.9 cGpc$^3$. However, the spectral coverage ($1.88 \leq z_{\mathrm{Ly}\alpha} \leq 3.52$) and resolving power are limited ($R \sim 800$).

The HETDEX line flux limit per resolution element in Figure 2.3 is scaled to match their best case line flux limit in order to compare the surveys outright. The limiting flux is similar in amplitude and shape but VIRUS' sensitivity decrease at bluer wavelengths is more gradual compared to that of the WEAVE LIFU. As the sensitivities are comparable in the overlapping range, we calculate a more refined estimate of the number of detectable LAEs to expect by extrapolating the HETDEX goal of $1.1 \times 10^5$ galaxies cGpc$^{-3}$ (Gebhardt et al., 2021) over the WEAVE LIFU's entire wavelength (redshift) range. This results in $\sim$ 144 LAEs, of which $\sim$ 92 ($\sim$ 63.5 %) in the redshift range $3.5 < z \lesssim 6.8$ unreachable by HETDEX.

This calculation does not account for the decreased co-moving volume due to lensing (Vieuville et al., 2019), overlapping of fields, or obscuration by extended cluster members and vastly increased number of sky lines in the red, which all decrease the number of expected LAEs. However, the WEAVE LIFU flux limit is a lower estimate, the LAE LF increases in the additional redshift range of the WEAVE LIFU (Ouchi et al., 2020), and the more numerous faint end may be probed through lensing (Vieuville et al., 2019; Thai et al., 2023). To which extent these effects interact is unknown, but the estimated number of LAEs is likely a lower limit. Moreover, while not matching HETDEX's number of LAEs, the WEAVE LIFU may be able to provide spectroscopic morphological properties of the Ly$\alpha$ line – useful to infer, e.g., the physical conditions (Blaizot et al., 2023) – whereas HETDEX/VIRUS cannot (Gebhardt et al., 2021).

# 3 Mathematical Morphology & the Max-Tree

In an IFU datacube, sources may be spatially overlapping along the line of sight, intertwining their spectra. Moreover, spectral features (e.g., emission lines) may be superimposed on top of the continuum of any source. Therefore, a datacube's two spatial and single spectral axis cannot provide a disentangled description of the observed volume. Complete lattices and their operators – unions, intersections, etc. – are a natural way to deal with the morphology of these superimposed structures in a datacube.

Mathematical Morphology was originally devised using the foundational *erosion* and *dilation* operations that suffer from undesirable irreversible non-edge-preserving properties, i.e., they alter the shape and contours of structures in the data. In order to accurately recover the flux belonging to a source, MTO utilizes edge-*preserving region*-based operations called *connected operators* $\psi$ (Salembier & Wilkinson, 2009; Najman & Talbot, 2010). Instead of pixels or voxels, connected operators act on *flat zones*, which are regions of the space at constant gray-level or intensity, connected by some neighborhood relation (Najman & Talbot, 2010). The edge-preserving property implies that a connected operator cannot transform a flat zone's existing boundary or create a new boundary, but can merge flat zones, removing their boundaries in the process (Salembier & Wilkinson, 2009).

One popular approach of connected operators are tree-based connected operators (Salembier and Wilkinson, 2009, see, e.g., Bosilj et al., 2018 for a review). Since trees are simply a subset of graphs and graphs can conform to the complete lattice structure (Vincent, 1989), Mathematical Morphology can be applied to tree representations of the data (Najman & Cousty, 2014). Noting that an astronomical source is characterized by its emission (ignoring absorption), connecting regions of positive intensity should correspond to sources of emission. A max-tree does precisely that by merging flat zones nested in other flat zones, into a hierarchical collection of nodes.

There are multiple algorithms to compute the max-tree (Carlinet & Geraud, 2014), but we utilize the max-tree algorithm by Berger et al., 2007, implemented in the hierarchical graph analysis Python package (Higra;[12] Perret et al., 2019).

## 3.1 The max-tree

A partially ordered set $L$ can be represented as a *lattice* $(L, \leq)$ (Najman & Talbot, 2010), with *partial order relation* $\leq$, if $\forall\, a, b, c \in L$ the following are satisfied,

$$\begin{array}{lll} \text{reflexivity} & & a \leq a, \\ \text{transitivity} & \text{if} \quad a \leq b \wedge b \leq c & \Rightarrow \quad a \leq c, \\ \text{anti-symmetry} & \text{if} \quad a \leq b \wedge b \leq a & \Rightarrow \quad a = b. \end{array} \tag{3.1}$$

The lattice $L$ can be *completed* ($\mathcal{L}$), if for every non-empty subset $\mathcal{K} \subseteq \mathcal{L}$ the subset admits an infimum $\bigwedge \mathcal{K}$ and supremum $\bigvee \mathcal{K}$, with $\mathcal{L}$ now denoting a *complete lattice* (Ronse, 1990; Lézoray, 2016).

The construction of a max-tree requires a *total order*, as opposed to a partial order. A *total order* can be imposed on $\mathcal{L}$ if $\forall\, a, b \in \mathcal{L}$, $a \leq b \vee b \leq a$ (implicitly implying reflexivity, Equation 3.1), transforming the *complete lattice* into a *complete chain* (Najman & Talbot, 2010). An example of a *complete chain* is the completed real numbers $\overline{\mathbb{R}} = \mathbb{R} \cup \{-\infty, +\infty\}$ (Najman & Talbot, 2010; Serra, 2022).

A datacube can be defined as $D : V \to \mathcal{I}$, which maps the coordinate volume domain $V \subset \overline{\mathbb{R}}^3$ to a *complete chain* $\mathcal{I} \subset \overline{\mathbb{R}}$, the set of gray-level intensities. Typically, intensities of astronomical datacubes are comprised of 32-bit floating point data, where the $\bigwedge \mathcal{I}$ and $\bigvee \mathcal{I}$ simply represent the minimum and maximum intensity respectively.

[12] https://github.com/higra/Higra

The level set $Y_t(D)$ and threshold set $X_t(D)$ of $D$ (Westenberg et al., 2007; Salembier & Wilkinson, 2009) represent the voxel occupancy at or above intensity threshold $t$ respectively,

$$Y_t(D) = \{x \in V \mid D(x) = t\} \qquad \text{and} \qquad X_t(D) = \{x \in V \mid D(x) \geq t\}. \tag{3.2}$$

By subsequently imposing a graph-based path connectivity, any consecutive neighboring voxels belong to the same connected component $CC(X)$ of $X_t(D)$ or *flat zone* of $Y_t(D)$ respectively (Salembier & Wilkinson, 2009). For 3DMTO, we use a 6-connectivity (Kong & Rosenfeld, 1989). As an example, for a Gaussian signal in $D$, a flat zone represents a shell of voxels at constant intensity surrounding the peak of the Gaussian, while the $CC(X)$ represents the sphere of voxels out to the flat zone, i.e., the voxels belonging to the flat zone and those with higher intensities encapsulated within.

A max-tree is an increasing gray-scale connected operator that encodes the hierarchy of connected voxel occupancy for each intensity level of $\mathcal{I}$. The *peak component* $P_t^x$ at gray-level $t \in \mathcal{I}$ and position $x \in V$ refers to the $x$th $CC(X)$ (Westenberg et al., 2007). The max-tree node $C_t^x$ corresponding to $P_t^x$ is then represented by the $CC(X)$ such that $CC(X) \cap Y \neq \emptyset$ (Salembier & Wilkinson, 2009), and linked together following an inclusion relationship as shown in Figure 3.1. The inclusion relation between nodes is as follows: for any

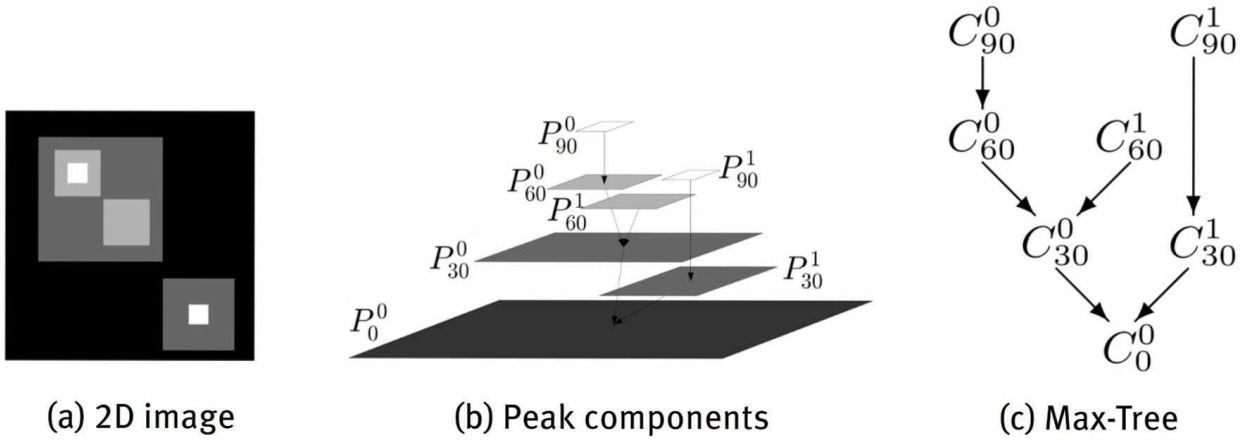


Figure 3.1: Illustrative example of a 2D image and its corresponding max-tree representation. (a) A 2D image with gray-scale intensities ranging from 0 to 90, and its corresponding (b) peak components $P_t^x$, and (c) max-tree nodes $C_t^x$. (Figure from Teeninga et al., 2016).

two nodes $P_{t_1}^x$ and $P_{t_2}^x$ at $t_1 \geq t_2$ respectively, the nodes are either nested, $P_{t_1}^x \subset P_{t_2}^x$, or disjoint $P_{t_1}^x \cap P_{t_2}^x = \emptyset$ (Ghamisi et al., 2015; Gu et al., 2023). Therefore, a (max-)tree is a rooted Directed Acyclic Graph (DAG) (Huang et al., 2003), implying that from the root of the tree to any other particular node, there is only one unique path. Hereafter, $P$ will be used interchangeably with $C$ to mean a max-tree node, where the sub- and super-script may be omitted for notational convenience.

Because the max-tree is a DAG, the inclusion relationship provides a natural interpretability, with terminology reminiscent of family trees, which in addition to some other max-tree properties is described in Table 3.1. The root represents the entire datacube and traversing the tree from root to leafs we first encounter nodes corresponding to entire sources, and their descendants describe even finer regions, e.g., emission features.

We can use the voxels belonging to a particular region of the datacube to compute attributes that describe the region's characteristics. The number of datapoints in a max-tree node is referred to as *area*, a term with an intuitive meaning devised in the 2D image domain but generalizable to any dimension. Furthermore, the *altitude* refers to the threshold level at which the peak component was constructed. These attributes can be defined as follows:

$$\text{area}(P) = \sum_{x \in P} \mathbf{1}_P(x) \qquad \text{and} \qquad \text{altitude}(P_t^x) = t, \tag{3.3}$$

Table 3.1: Descriptions of a few max-tree properties. The third column provides the corresponding equations and example nodes shown in Figure 3.1.

| max-tree property | description | equation/example nodes |
|---|---|---|
| area($P$) | The number of voxels contained in node $P$ | Equation 3.3 |
| altitude($P$) | The gray-level or intensity of voxels unique to node $P$ | Equation 3.3 |
| root node | "Highest" node in the tree, contains entire datacube | $C_0^0$ |
| ancestor nodes | Nodes "above" the current node up to root. The first ancestor is parent($P$) | e.g., $C_{60}^0, C_{30}^0, C_0^0$ for $C_{90}^0$ where parent $\left(C_{90}^0\right) = C_{60}^0$ |
| descendant nodes | Nodes "below" the current node. The first descendants are referred to as children. | e.g., $C_{60}^1, C_{60}^0, C_{90}^0$ for $C_{30}^0$; $C_{60}^0$ and $C_{60}^1$ are children |
| leaf nodes | Endpoints of the tree. They do not have any children and correspond to the smallest regions | $C_{90}^0, C_{90}^1$ |
| branch/object | Hierarchical collection of nodes | e.g., $C_{60}^1 \longrightarrow C_{30}^0 \longrightarrow C_0^0$ |

where $\mathbf{1}_P(x)$ is the *indicator function*: equal to 1 if $x \in P$ and 0 otherwise. The area($P$) and altitude($P$) are both *increasing* attributes, implying that the ordering is upheld such that if a *criterion* $T : CC(X) \longrightarrow \{\texttt{true}, \texttt{false}\}$ holds for a $CC(X)$, it also holds for all $cc$ nested in $CC(X)$ (Salembier & Wilkinson, 2009; Ghamisi et al., 2015).

The max-tree leads to *anti-extensive* connected operators as a $CC(X)$ can only be removed and not created, i.e., $\forall\, \psi(D) \subseteq D$ (Salembier et al., 1998). A (connected) operator is often defined for a binary case but may be generalized into a gray-scale operator through the principle of *threshold decomposition* (Maragos & Ziff, 1990; Salembier & Serra, 1995). This way it can act on all $CC(X)$ at different intensity levels. Breen and Jones, 1996 used the principle of threshold decomposition to establish *attribute openings* and *attribute thinnings* – also referred to as connected *attribute filtering* – to filter connected components based on a criterion devised to retain objects of interest. Shortly thereafter this filtering was similarly applied to (max-)trees by Salembier et al., 1998 and Jones, 1999 and is used by MTO to distinguish between nodes corresponding to objects or noise.

# 4 3DMTO

The max-tree is only an alternative representation of the data in terms of regions, but does not intrinsically decide which regions are significant objects. The following sections describe various aspects of (3D)MTO, like utilizing attribute filtering to distinguish objects from noise and subsequently calculating object properties. 3DMTO is the version of MTO devised in this thesis to be applied to 3D IFU datacubes.

## 4.1 Determining objects

The max-tree representation of a datacube segments all regions into a hierarchical tree of objects or collection of nodes. The first step is to apply background subtraction and truncate the signal to positive values only (Teeninga et al., 2016). In this datacube, emission features of a source will be segmented as separate branches from the node that encapsulates all the flux from a source, i.e., the continuum + emission features. In the ideal case, the max-tree nodes should thus refer to either an emission feature, a total source, noise features, and the entire datacube at the root of the tree. However, artifacts like cosmic rays or sky-subtraction residuals remaining after imperfect data cleaning can also erroneously be marked significant, and absorption features can break an emission source apart into separate objects. The following subsections discuss the part of the MTO algorithm that decides which nodes should be considered significant objects.

### 4.1.1 Power attribute

The power attribute, originally devised by Young and Evans, 2003, is analogous to the source flux or integrated intensity in astronomy. Teeninga et al., 2016 adapted the power to optical astronomy for MTO, introducing the variance $\sigma^2(x)$ as a normalization factor:

$$\text{power}(P) = \sum_{x \in P} \left( \frac{f(x) - \text{altitude}(\text{parent}(P))}{\sigma(x)} \right)^2, \tag{4.1}$$

where $f(x)$ is the intensity in voxel $x$, altitude(parent($P$)) represents the constant *local* background flux of node $P$, and $1/\sigma(x)^2$ is the inverse variance in voxel $x$, obtained from the IVAR datacube.

Because the altitude is an increasing attribute, we can use it to define the local background to be the altitude of a descendant node. altitude(parent($P$)) will always be lower than the altitude of any voxel $x$ in $P$. In Teeninga et al., 2016, the variance was solely the local background variance – which is assumed constant for $x \in P$ – consisting of a local Poisson background component, and a global constant background variance. This is not a valid assumption for IFU datacubes (see Section 6.4 for a discussion). 3DMTO is therefore normalized using the IVAR, i.e., the total variance from all flux contributions.

In the current from of Equation 4.1, the power cannot be efficiently computed using a max-tree, but Appendix A shows how the power can be expanded into its constituents, which can all be efficiently computed using a max-tree.

### 4.1.2 Marking significant nodes

In order to decide if a node $P$ is significant, MTO uses a binary statistical hypothesis test to decide between

- $\mathcal{H}_0$: the node is part of the background distribution.
- $\mathcal{H}_1$: the node significantly deviates from the expected background distribution.

In the optical, Poisson noise dominates and becomes approximately Gaussian for large-enough intensity.The (local) background noise is therefore simply the square root of the background signal. This assumption does

not hold at positions where additional shot-noise by bright sources violates the assumption of a background-limited search (Section 1.3.1). For nodes $P$ that are solely due to Gaussian background noise, the power is essentially the $\chi^2$-test statistic, i.e., the sum of the squared difference between the signal and the background, divided by the background. Therefore, $\text{power}(P) \sim \chi^2(\nu = \text{area}(P))$ with $\nu$ the degrees of freedom (Teeninga et al., 2016). Similarly, for any random voxel $x$ in $P$, the power is $\chi^2(\nu = 1)$ distributed where the summation in Equation 4.1 can be omitted. However, where in Teeninga et al., 2016 the power is normalized by the local background variance, for which the above assumptions are valid, 3DMTO uses the total variance. Section 6.6 further discusses the validity of the assumed $\chi^2$-distribution for IFU data.

To determine if a node is significant, we need to decide if its test statistic is significant. The rejection boundary for some significance level $\alpha$[13] that decides if a node significantly positively deviates from the expected $\chi^2(\nu)$-distribution is given by the Inverse Cumulative Distribution Function: $\text{ICDF}\chi^2(1-\alpha, \nu)$. Figure 4.1 visually illustrates how, for nine degrees of freedom, decreasing $\alpha$ correspondingly increases the rejection boundary ($x$-axis). Therefore, the power required for a node to be marked significant increases. The middle panel represents the power through proxy of the S/N.

A node $P$ is marked significant when $\mathcal{H}_0$ is rejected, i.e., if the test statistic exceeds the rejection boundary, $S(P) : \text{power}(P) > \text{ICDF}\chi^2(1-\alpha, \text{area}(P))$. By assumption, a significant node contributes considerable flux above the background level, i.e., an astronomical source. However, the test does not discriminate what causes the positive deviation with respect to the background distribution (Greenland et al., 2016), and nodes containing artifacts like cosmic rays or sky residuals may be marked significant as well. In addition, the middle panel of Figure 4.1 demonstrates how it can occur that only one peak of the Ly$\alpha$ line is marked significant, whilst the other peak – segmented as a separate object – may not be significant.

### 4.1.3 Objects from significant nodes

A node describes a region in the datacube. A branch of the max-tree therefore describes a hierarchical collection of regions. Numerous nodes within a branch can be significant, therefore Teeninga et al., 2016 define an object to be a significant node with no significant ancestors within the remainder of the same branch. This naturally accounts for the deblending of nested objects, as long as each object can be separately considered significant.

We use this object representation property of the max-tree to filter the data using the max-tree instead of filtering the datacube directly. The specific filtering used is referred to as tree *simplification*, in which nodes that do not meet the criterion $S(P)$ are deemed redundant and removed. The max-tree now only contains significant nodes that correspond to objects, for which we will compute descriptive attributes in the next section.

Teeninga et al., 2016 made use of an additional `move_up` step, introduced to curb the number of erroneously connected voxels that are part of the background. This step is meant to counteract the noise voxels that are attached to objects, freeloading off the power from those objects, by moving the node that marks an object up the branch. However, `move_up` is not an ideal solution and primarily serves a cosmetic purpose, decreasing the extent of the segmentation, and hence is omitted from 3DMTO.

## 4.2 Attributes

Now that regions are filtered based on significance into objects, various attributes used to describe said objects' characteristics can be computed. Three attributes have been defined and used prior in this chapter, namely the altitude($P$) and area($P$) shown in Equation 3.3, and the power($P$) in Equation 4.1. A max-tree can be efficient for computing attributes as it takes into account the gray-level of the segmented voxels belonging to

[13] Not to be confused with the faint end slope of the LAE LF defined in Section 1.3.1.

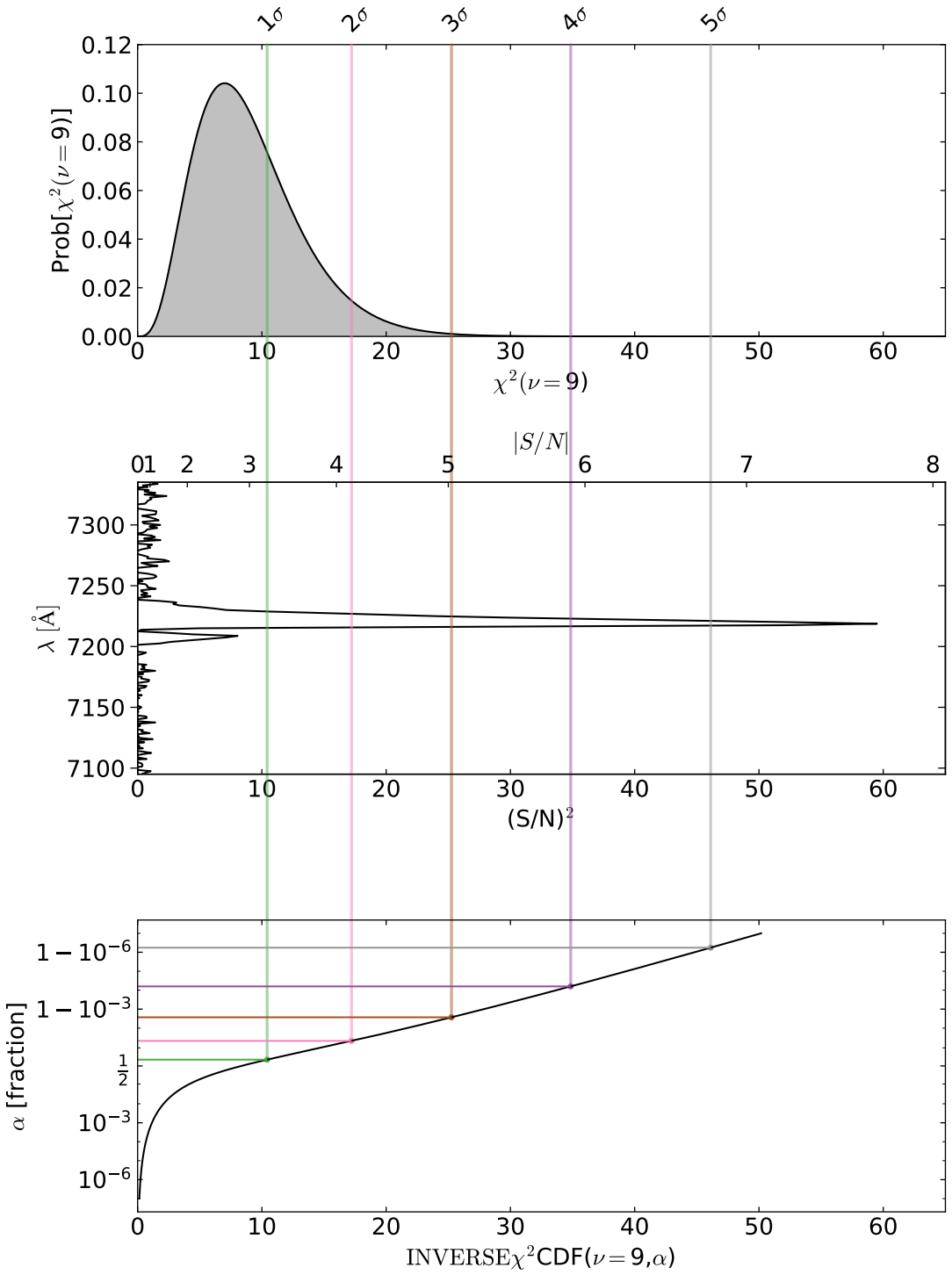


Figure 4.1: Illustrative example of how the rejection boundary compares with a doubly-peaked Ly$\alpha$ line of an LAE from BA23. *Top*: $\chi^2$ probability as a function of $\chi^2$. *Middle*: integrated (nine spaxels) signal-to-noise (squared) along the spectrum of the LAE, centered on the doubly-peaked Ly$\alpha$ line. *Bottom*: significance level $\alpha$ as a function of the rejection boundary. All three panels share the same lower $x$-axis and the upper $x$-axis of the middle panel is scaled by the square root of the lower axis. The $y$-axis in the bottom panel has been *logit*-scaled (Berkson, 1951) to highlight how a minute difference in $\alpha$ increases ICDF$\chi^2$ significantly. The vertical colored lines (all three panels) indicate the rejection boundary or standard deviation of the lower tail probability corresponding to significance level $\alpha$ (lower panel $y$-axis).

an object, and some attributes could be computed during the max-tree build process. Moreover, the nested tree structure allows for simple accumulation of increasing attributes in its branches.

A family of such attributes are geometric moments. We use the first-order geometric moment to define the position of an object in the datacube by computing its weighted centroid,

$$\bar{q} = \frac{\sum_i q_i f(x,y,z)_i}{\sum_i f(x,y,z)_i} \qquad \text{with} \qquad q = \{x, y, z\}, \tag{4.2}$$

where the numerator and denominator are the first and zeroth geometric moments for a 3D volume respectively, and $x, y, z$ represent the voxel coordinates in the datacube. The $x, y, z$ coordinates live in coordinate volume domain $V$ and, using the world coordinate system (WCS) detailed in the FITS header, can be converted to wavelength ($\lambda$), longitude (DEC), and latitude (RA) respectively.

The zeroth order geometric moment, represents the total flux of object $P$. To instead obtain the flux solely belonging to the (component of a) source from detected object $P$, the local background has to be subtracted; that is, any flux not pertaining to the source, e.g., the continuum around an emission line. The source flux, and accompanying uncertainty, are computed by summation over the voxels attributed to $P$ in the signal and IVAR datacube respectively,

$$\mathrm{F}(P) = \sum_{x \in P} [f(x) - \mathrm{altitude}(\mathrm{parent}(P))] \qquad \text{and} \qquad \sigma(P) = \sqrt{\sum_{x \in P} \frac{1}{\sigma(x)^2}}, \tag{4.3}$$

where $1/\sigma(x)^2$ is the IVAR, and the signal-to-noise attribute follows trivially,

$$\mathrm{SNR}(P) = \mathrm{F}(P)/\sigma(P). \tag{4.4}$$

### 4.2.1 scale-invariant attributes

The next set of attributes describe the shape of an object within the datacube and are all scale-invariant, i.e., they are independent of the size of an object. Therefore, they are non-increasing attributes (Breen & Jones, 1996; Salembier & Wilkinson, 2009). We preface this by stating that the voxel length L and the shape of an object in the datacube are not physical. The two spatial axes are not comparable with the spectral axis (see Section 6.7 for a discussion), yet voxel representations potentially remain insightful to distinguish the type of source that corresponds to a particular selection of attributes.

One such attribute is the sphericity index (Wadell, 1933; Cruz-Matías et al., 2019),

$$\mathrm{SI}(P) = \frac{\text{surface area of a sphere with volume equivalent to the object}}{\text{surface area of the object}} = \frac{\sqrt[3]{36\pi\,\mathrm{area}(P)^2}}{\mathrm{SA}}, \tag{4.5}$$

normalized within the interval $(0, 1]$, such that it equals 1 for the most compact possible shape of a perfect sphere, and decreases for less compact shapes. Here SA is the surface area of the object. Currently, SA is approximated by Higra's `attribute_contour_length`,[14] which calculates the number of connected elements not part of the object. This approach suffers from its rough discrete nature and is therefore not entirely appropriate, but it appears to only compress the normalization to $(0, \lesssim 1]$ and does not compromise the interpretability of the sphericity index when considering detections relative to each other within a dataset. More sophisticated estimations of the surface area could be used to combat the inaccurate surface area estimation (Cruz-Matías et al., 2019).

[14] https://higra.readthedocs.io/en/stable/python/tree_attributes.html#higra.attribute_contour_length.

The final four attributes are all derived from the moment-of-inertia tensor. Following Westenberg et al., 2007, the moment-of-inertia tensor can be calculated as

$$\mathbf{I}_{ij}(P) = \begin{cases} \sum_{x \in P} (x_i - \bar{x}_i)(x_i - \bar{x}_i) + \dfrac{\text{area}(P)}{12} & \text{if } i = j, \\ \sum_{x \in P} (x_i - \bar{x}_i)(x_j - \bar{x}_j) & \text{if } i \neq j, \end{cases} \tag{4.6}$$

where $i, j \in \{x, y, z\}$, $\bar{x}_q$ is the weighted centroid of node $P$ for coordinate $q$, and $1/12$ is the moment-of-inertia contribution of an individual cubic voxel, which when multiplied by the total number of voxels area($P$), constitutes a *correction* term for the diagonal entries. The correction term improves the notion of scale invariance and avoids division-by-zero errors in subsequent calculations employing the eigenvalues (Westenberg et al., 2007). By decomposing each component of Equation 4.6 into its constituents, the calculation simply requires the first, second and cross-term moments,[15] and area($P$), all increasing attributes that are easily obtainable using a max-tree.

The first attribute which we compute from $\mathbf{I}(P)$ is the non-compactness (Wilkinson & Westenberg, 2001),

$$\mathcal{N}(P) = \frac{\text{Tr}[\mathbf{I}(P)]}{\text{area}(P)^{5/3}}, \tag{4.7}$$

where Tr[$\mathbf{I}(P)$] is the trace of the moment-of-inertia tensor. $\mathcal{N}(P)$ Is a scale-invariant attribute because $\mathbf{I}(P)$ is proportional to the voxel length L of an object in the datacube like $\mathbf{I}(P) \propto \text{L}^5$, while area($P$) – the volume of the object – is proportional to $\text{L}^3$. For a perfect sphere, $\mathcal{N}(P)$ reaches a minimum of 0.25 and is larger for increasingly more complex structures.

The moment-of-inertia tensor is a positive definite matrix, implying its eigenvalues are real and strictly positive (Sousa & Cortesão, 2019). The eigenvalues represent the variance of the coordinates along the main axes of an object, scaled by volume, and their relations to each other allow an object to be classified by its shape (Najman & Talbot, 2010). Westenberg et al. specified three more scale-invariant attributes, based on the three eigenvalues $\lambda_i(P)$ of the moment-of-inertia tensor, ordered such that $|\lambda_1(P)| \geq |\lambda_2(P)| \geq |\lambda_3(P)|$. These are the *elongation*, *flatness*, and *sparseness*, expressed as the ratios,

$$\mathcal{E}(P) = \left|\frac{\lambda_1(P)}{\lambda_2(P)}\right|, \qquad \mathcal{F}(P) = \left|\frac{\lambda_2(P)}{\lambda_3(P)}\right|, \qquad \text{and} \qquad \mathcal{S}(P) = \frac{\pi}{6 \cdot \text{area}(P)} \prod_{i=1}^{3} d_i(P), \tag{4.8}$$

where $d_i(P) = \sqrt{20|\lambda_i| \,/\, \text{area}(P)}$, the lengths of the principal axes. For perfectly spherical objects $|\lambda_1(P)| = |\lambda_2(P)| = |\lambda_3(P)|$ and trivially $\mathcal{E} = \mathcal{F} = (\mathcal{S}) = 1$, which increase for more complicated (porous) tri-axial shapes. Elongated shapes will have $|\lambda_1(P)| > |\lambda_2(P)| \geq |\lambda_3(P)|$, for which $\mathcal{E} > 1$ and $\mathcal{F} > 1$, but for cylindrical or cigar-shaped objects $\mathcal{F} \approx 1$ (Gazagnes et al., 2021).

The computed attributes are exported to a csv file, as well as an astropy FITS table that preserves units where applicable.

[15] First moments: $\sum x, \sum y, \sum z$; second moments: $\sum x^2, \sum y^2, \sum z^2$; cross-term moments: $\sum x \cdot y, \sum x \cdot z, \sum y \cdot z$.

# 5 Ly$\alpha$-line detection

Unfortunately, due to the limited – and still provisional – WEAVE LIFU data available at the time of writing, we have yet to discover an LAE. So to ascertain the capability of 3DMTO to detect and recover the Ly$\alpha$ emission line, we compare our detections with the source catalog compiled by BA23, which presents a second data release for sources ($\sim 80\,\%$ have $\mathrm{EW}_0(\mathrm{Ly}\alpha) \leq -20\,\mathrm{\AA}$) in the MUSE *Hubble* Ultra-Deep Field survey. Specifically, we made use of the processed and reduced adaptive-optics-assisted MXDF datacube, with a (maximum) depth of 141 h in a circular $\sim$ 1 arcmin diameter footprint (top row of Figure 5.1). Moreover,

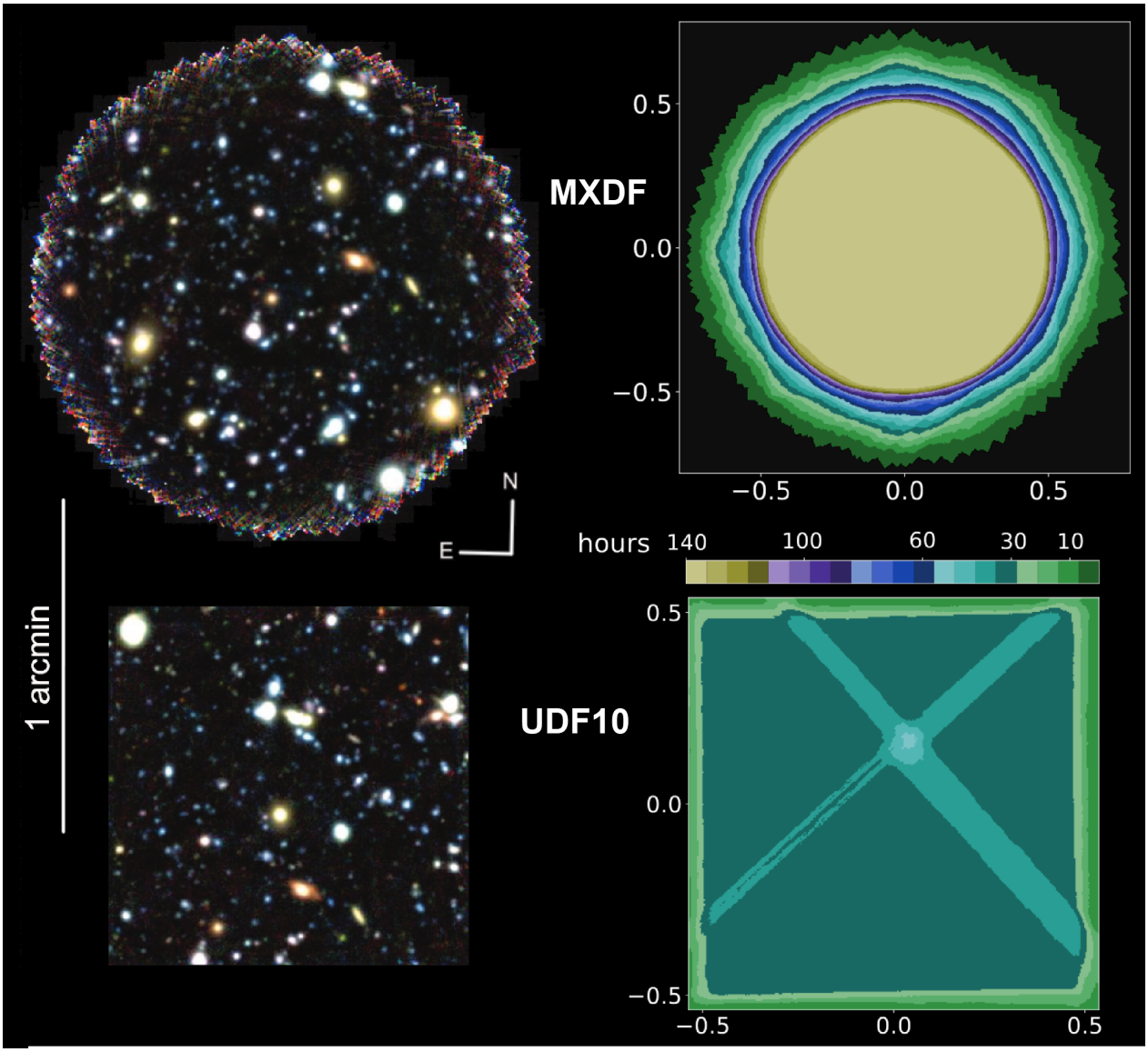


Figure 5.1: Reconstructed pseudo-color images (*left* column) and exposure time maps (*right* column) of MXDF (*top* row) and UDF-10 (*bottom* row) datacubes (BA23) respectively. The axes labels for the exposure time maps are in arcminutes. (Figure adapted from BA23).

they produced a source catalog[16] using detections from ORIGIN and ODHIN (BA23), with all data products

[16] We used the "Main source catalog" version 0.9 in this thesis.

freely available online.[17] They employed a weighted "optimal" extraction, following Horne, 1986, to obtain a reference spectrum for each source. With this in mind, the source properties were derived from either the ORIGIN or ODHIN reference spectrum using pyPlatefit (BA23), based on the redshift solutions provided by pyMarZ, and subsequently verified and reconciled by experts when required. Additionally, they also found a robust correspondence when comparing the catalog with detections from LSDCat.

## 5.1 Detected LAEs

To keep comparisons consistent, only catalog detections with the ORIGIN reference spectra will be compared. Table 5.1 specifies that the LAEs selected from the BA23 catalog are sourced only from the MXDF datacube, with $\mathrm{EW}_0(\mathrm{Ly}\alpha) < -20$ Å, and have confident redshift solutions derived from detections by ORIGIN only. Section 6.1.2 elaborates on the reasoning for these cuts.

Table 5.1: LAE catalog cuts (applied left to right) on the BA23 catalog. The catalog contains 2221 sources: *key* refers to the column in the catalog, *condition* specifies which sources based on that column should be kept, and *remaining sources* indicates the number of sources left after each cut. The key **DATASET** specifies the data(cube) used, **LYALPHA_EMI_EQW** is $\mathrm{EW}_0(\mathrm{Ly}\alpha)$ (Equation 1.1), **ZCONF** indicates the redshift confidence, and **FROM** details the reference extraction used. The shaded cells indicate the LAEs used in subsequent analysis, unless specifically stated otherwise.

| key | **DATASET** | **LYALPHA_EMI_EQW** | **ZCONF** | **FROM** |
|---|---|---|---|---|
| condition | MXDF | $< -20$ Å | $\geq 2$ | ORIGIN |
| remaining sources | 661[a] | 183 | 156 | 133 |

The LAE with "**ID** = 171" falls within the MXDF footprint but not the spectral coverage due to a filter for the laser guided optics, but is accounted for through the **DATASET** condition.

[a] 664 sources remained but 3 additional sources at the edge were removed (see Section 6.1.1).

We ran 3DMTO on the MXDF datacube using $\alpha = 5\times10^{-4}$, resulting in $\sim$ 1898 usable (see Section 6.1.1) detections. We cross-matched 3DMTO's detections with the corresponding source from the catalog based on the RA, DEC, and in the case of Ly$\alpha$ line, also the velocity $V_{\mathrm{Ly}\alpha}$ derived from the redshift. We match a detection if a catalog counterpart exists within $1''$ angular separation, and is offset in velocity space by $< \pm 685\,\mathrm{km\,s^{-1}}$. See Section 6.1.3 for an elaboration on these limits. Substantially increasing the spatial or spectral cross-matching limits does not significantly alter the number of detections (see Section 6.8.2).

Figure 5.2 shows the 3DMTO detections, catalog LAEs, and those cross-matched between the two, in the MXDF footprint. Additionally, 3DMTO found 39 unmatched detections, appearing more sporadically throughout the footprint, e.g., the strip of detections in the bottom left, and are often not real sources (see Section 6.8.3). Curiously, there are LAEs with S/N larger than some LAEs that were cross-matched, yet 3DMTO did not detect emission of any kind for these LAEs, i.e., the red colored □ and ⋈ markers with relatively larger sizes and no ○ or ✖ markers in the vicinity. Another peculiarity is that some unmatched 3DMTO detections seem to be in proximity of LAEs, which are not necessarily cross-matched. A subset of these unmatched detections are at the Ly$\alpha$ wavelength corresponding to the LAE, possibly indicative of extended Ly$\alpha$ emission not connected by 3DMTO and/or captured by the reference extraction (BA23, Sec. 5.8.1).

From the cross-matching, we determined the LAE recall – ratio of LAEs recovered over total LAEs in the selection – for various selection criteria, presented in Table 5.2. Overall, the recall does not vary significantly based on the selection, although the recall is lower for fainter (less negative $\mathrm{EW}_0(\mathrm{Ly}\alpha)$) LAEs than the brighter LAEs by a few percent. Section 6.8.2 further discusses the evolution of recall with Ly$\alpha$ equivalent width.

[17] https://amused.univ-lyon1.fr/project/UDF/HUDF/

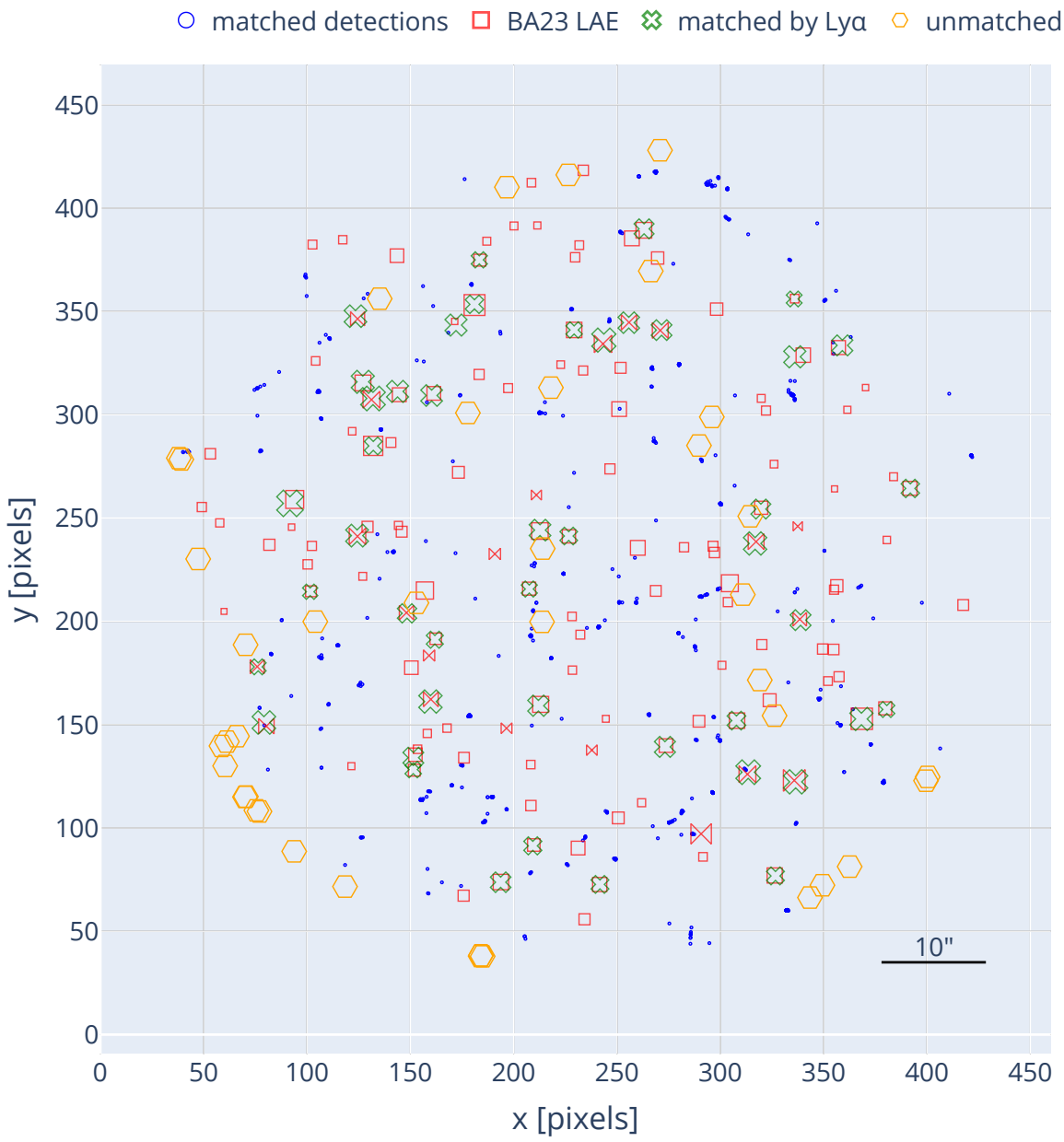


Figure 5.2: The results of the $< 1''$ cross-matching with all catalog sources of BA23 in the MXDF footprint. ○ marks all detections by 3DMTO, where the opacity of the points is such that if it appears solid, there are numerous superimposed detections (of the same source and/or different sources) along the wavelength axis. The □ and ⋈ respectively indicate singly- and doubly-peaked LAEs from the catalog selection presented in Table 5.1. The marker size scales with the S/N reported in the catalog. ✖ corresponds to detections that are matched to catalog LAEs by their Ly$\alpha$ line within $\pm 685\,\mathrm{km\,s^{-1}}$ (see shaded cells of Table 5.2). The marker center corresponds to the centroid of 3DMTO and the size scales with the number of segmented voxels. ⬡ indicates all detections by 3DMTO that were not matched within $< 1''$, and the marker size roughly represents this angular extent.

Doubly-peaked Ly$\alpha$ is consistently recovered with almost double the recall of the total sample, despite 3DMTO possibly only segmenting a single peak (see Section 6.5). Considering this limitation, it is somewhat

Table 5.2: Recall of the cross-matching (within 1″ angular separation and $\pm 685\,\mathrm{km\,s^{-1}}$) against Ly$\alpha$ lines in the BA23 catalog for various selection conditions: **IN_ORI** refers to if the source is matched by ORIGIN (true) or not (false), and **FROM** = ORIGIN specifies that the reference spectrum from ORIGIN was used to derive the galaxy properties. The "sample" row specifies if both singly- and doubly-peaked Ly$\alpha$ (total) or only doubly-peaked Ly$\alpha$ lines (double) are considered. The shaded cells indicate the LAEs used in subsequent analysis, unless specifically stated otherwise. Note that the **DATASET** & **ZCONF** columns in Table 5.1 also apply to all entries in this table.

| condition | | **IN_ORI** true | | **IN_ORI** false | | **FROM** ORIGIN | |
|---|---|---|---|---|---|---|---|
| sample | | total | double | total | double | total | double |
| $EW_0(Ly\alpha) <$ 0 Å | LAEs | 209 | 33 | 8 | 2 | 180 | 22 |
| | matched | 61 | 20 | 2 | 1 | 51 | 14 |
| | recall | 29.19 % | 60.61 % | 25.00 % | 50.00 % | 28.33 % | 63.64 % |
| $EW_0(Ly\alpha) < -20$ Å | LAEs | 153 | 32 | 3 | 2 | 133 | 21 |
| | matched | 54 | 20 | 2 | 1 | 45 | 14 |
| | recall | 35.29 % | 62.50 % | 66.67 % | 50.0 % | 33.83 % | 66.67 % |

surprising that the recall for doubly-peaked Ly$\alpha$ is comparatively high. However, in all cases the doubly-peaked sample had considerably larger mean flux, as well as being limited to the lower redshift regime (Figure 5.4) in the catalog, making them easier to detect. It is noteworthy that the '**IN_ORI** = false' column contains LAEs that were only detected using ODHIN, indicating that 3DMTO detects two (bright) LAEs not detected by ORIGIN.

The left-most column of the shaded cells in Table 5.2 indicate the 45 out of 133 cross-matched LAEs (✖ in Figure 5.2) that we use for the remaining analysis of this chapter.

## 5.2 Ly$\alpha$ flux and S/N recovery

The two main quantities that can be compared for the cross-matched sources are the emission line flux and accompanying S/N. The unequivocal trend visible in Figure 5.3 is that 3DMTO chronically underestimates the flux, which also translates into a S/N deficit. In addition to a deficit, there also appears to be a positively linearly correlated relation, in which the dissonance with respect to the one-to-one relation grows larger with increasing flux and S/N. However, the correlations appear to be heteroscedastic, i.e., the relatively tight correlation seen at lower flux and especially S/N widens with increasing flux and S/N. The deficit does not appear to be exacerbated for doubly-peaked Ly$\alpha$, even though only one peak may be detected. This is not entirely unexpected, as often the red peak dominates (Blaizot et al., 2023), whereas flux blueward of the line center is attenuated by the IGM at all redshifts (Laursen et al., 2011; Gurung-López et al., 2020).

In the left-hand panel of Figure 5.3, there are a few detections that almost agree with the one-to-one relation, but none of their corresponding S/N ratios come close to the one-to-one relation in the right-hand panel. Presumably, this discrepancy is due to the 3D segmentation of the line by 3DMTO being inherently different from ORIGIN's corresponding flux determination. ORIGIN creates a 2D reference spectrum, extending it over the wavelength extent of the line into a tube-like 3D segmentation that is subsequently collapsed down to 1D, in order for the flux to be fit by pyPlatefit. The size of 3DMTO's segmentation, indicated by the size of the marker, does not appear to show strong correlation with flux or S/N ratio, with similar sized markers seen over the entire flux and S/N range. But perhaps unsurprisingly, in the low flux regime ($F_{Ly\alpha}^{MTO} \lessapprox 100 \times 10^{-20}\,\mathrm{erg\,s^{-1}\,cm^{-2}}$) there are only detections with a small number of voxels.

Given that detections are predominantly found below the one-to-one relation, 3DMTO does not seem to capture all the flux. This is most likely caused by incorrect local background subtraction, and any detections above the one-to-one relation appear to originate from under-segmentation or merging of separate detections

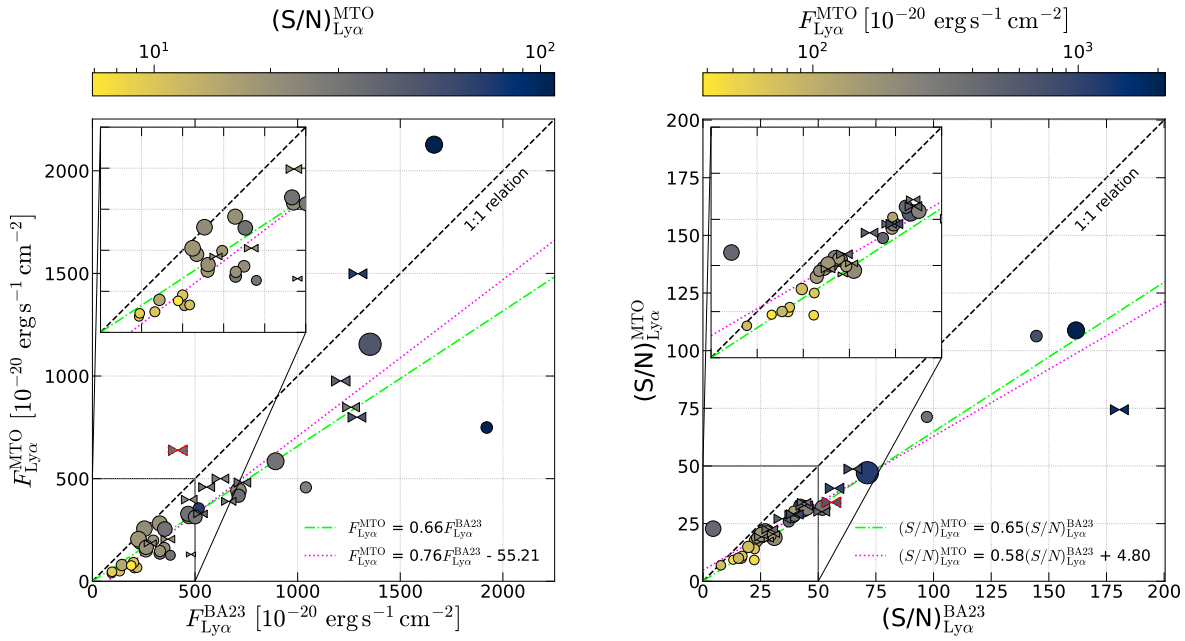


Figure 5.3: Comparing recovered flux and S/N of 3DMTO detections that were 3D matched to the Ly$\alpha$ line of an LAE in the BA23 catalog (see shaded cells of Table 5.2). The retrieved flux (left-hand panel) and S/N (right-hand panel) of 3DMTO ($y$-axis) are plot against the corresponding catalog value ($x$-axis). The color-scale shows the log-scaled quantity obtained by 3DMTO from the opposite panel. The ⧓ and ● markers indicate doubly- and singly-peaked Ly$\alpha$ respectively. The ⧓ marker with the red dotted outline indicates the peculiar cross-match. The size of the markers scales with the number of voxels segmented by 3DMTO. Both panels showcase a black dashed diagonal one-to-one relation, indicating perfect correspondence. The legends show the equations of the linear orthogonal distance regression fits (`scipy.odr.ODR`; Virtanen et al., 2020) with the intercept fixed at the origin (lime green dash-dotted) or as a free parameter (magenta dotted). The ticks in the inset axes correspond to 100 (left) and 10 (right) units respectively.

(see Section 6.6). However, in the left-hand panel of Figure 5.3, except for the peculiar Ly$\alpha$ detection (⧓ marker with the red dotted outline), all detections above the one-to-one relation do not contain considerably more voxels compared to other detections at the same or lower $F^{BA23}_{Ly\alpha}$; whereas in the right-hand panel, the one detection above the one-to-one relation contains significantly more voxels compared to other detections at the same $(S/N)^{BA23}_{Ly\alpha}$. An additional effect for these detections may be that the reference extraction underestimated the total $F^{BA23}_{Ly\alpha}$ (BA23, their Sec. 5.8.1).

## 5.3 Centroid comparison

Three more quantities that can be compared between a BA23 catalog source and cross-matched 3DMTO detection are their 3D centroid coordinates: RA, DEC, and $\lambda_{Ly\alpha}$ or $V_{Ly\alpha}$. The left-hand panel of Figure 5.4 shows that on average, cross-matches are within MUSE's 0.″2 pixel scale with RA and DEC offsets of $0.''05 \pm 0.''20$ and $-0.''01 \pm 0.''16$ respectively. The angular offset does not appreciably differ when considering singly- and doubly-peaked Ly$\alpha$ separately. The spectral offset does however show a clear discrepancy between singly- and doubly-peaked Ly$\alpha$ where, on average, singly-peaked Ly$\alpha$ with an offset of $-0.5 \pm 1.7$ Å ($-24 \pm 80$ km s$^{-1}$) falls within one 1.25 Å spectral resolution element, whereas doubly-peaked Ly$\alpha$ is offset by $3.2 \pm 1.7$ Å ($170 \pm 82$ km s$^{-1}$), almost $\sim 2.5$ spectral resolution elements.[18] Moreover, the doubly-peaked offset is predominantly positive, indicative of a bias in 3DMTO towards the commonly dominating red peak as opposed to the IGM suppressed blue peak. It is worth noting that the scatter is considerable for all offsets.

[18] This was determined excluding the peculiar doubly-peaked Ly$\alpha$ detection at $\sim -600$ km s$^{-1}$.

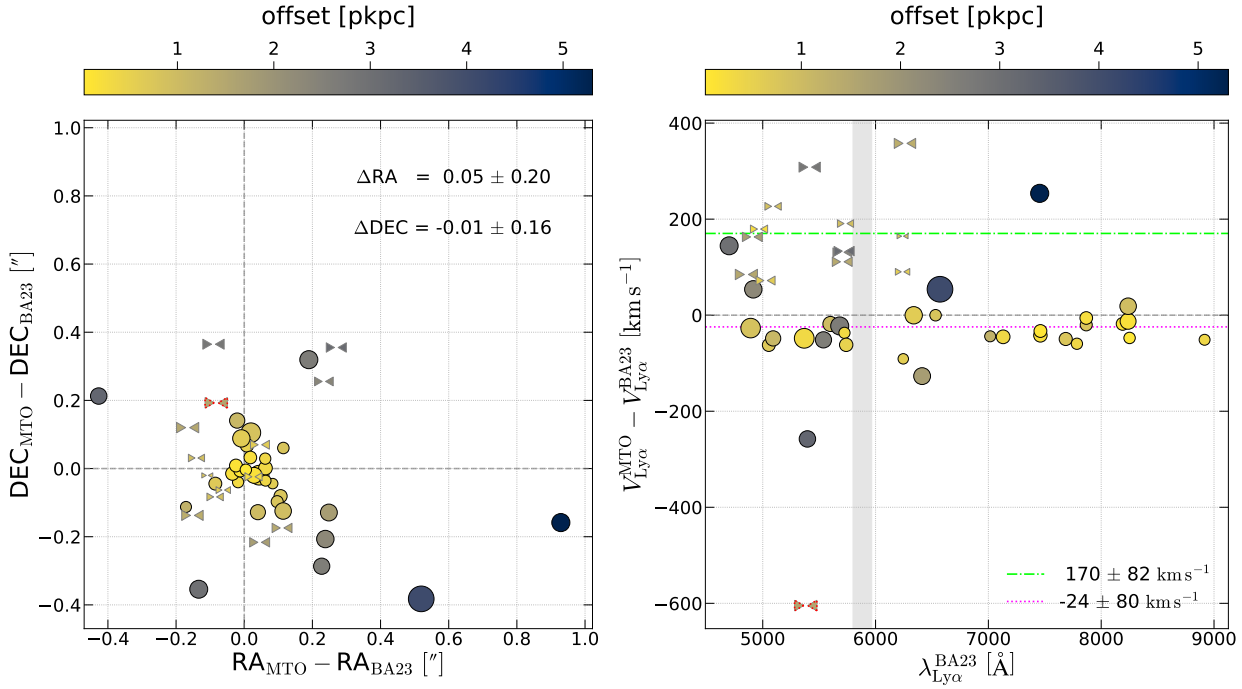


Figure 5.4: Comparing centroids of 3DMTO detections that were 3D matched to the Ly$\alpha$ line of an LAE in the BA23 catalog (see shaded cells of Table 5.2). *Left*: The difference in latitude ($x$-axis) and longitude ($y$-axis) where the center is emphasized by the two coinciding translucent gray dashed lines. *Right*: The velocity offset ($y$-axis) is plot as a function of the catalog wavelength ($x$-axis), with the translucent horizontal gray dashed line indicating perfect correspondence. The magenta dotted and lime green dash-dotted lines specify the mean velocity offset for singly- and doubly-peaked Ly$\alpha$ respectively, where for doubly-peaked Ly$\alpha$ we only consider those with positive velocity offsets ($V_{\mathrm{Ly}\alpha}^{\mathrm{MTO}} - V_{\mathrm{Ly}\alpha}^{\mathrm{BA23}} > 0\,\mathrm{km\,s^{-1}}$). The ⧓⧒ and ● markers indicate doubly- and singly-peaked Ly$\alpha$ respectively. The ⧓⧒ marker with the red dotted outline indicate the peculiar cross-match. The size of the markers scales with the number of voxels segmented by 3DMTO. The colorbar in both panels indicates the physical spatial offset between the centroids. In the right-hand panel, the gray shaded region, covering 5800-5966 Å, indicates the obscuration of the sodium filter that is used in the laser guided observing mode (BA23).

Detections with larger angular offset exclusively contain more voxels than the majority of detections in better agreement with the catalog centroid coordinates. Spectrally, this same trend holds for singly-peaked Ly$\alpha$, but is not as clear for doubly-peaked Ly$\alpha$, unless this offset is considered with respect to the average velocity offset for doubly-peaked Ly$\alpha$ instead of perfect agreement. This is not surprising, given that the (spatial) coordinates are calculated similarly between the datasets using the weighted centroid (Equation 4.2); however 3DMTO calculates the coordinates per detection (i.e., for a Ly$\alpha$ emission feature), whereas BA23 calculates them per source (see Section 6.1.3). The weighted centroid should roughly coincide with the peak coordinates, assuming that only one peak is segmented and the Ly$\alpha$ is spatially unresolved or at least symmetric (BA23). Considering this in addition to the majority of signal being concentrated near the peak voxels, only detections with considerable number of voxels could conceivably segment voxels that are appreciably offset from the peak. However, the spatial offset does appear to be small, and increasing the cross-match radius does not result in a considerable increase in cross-matches.

Another dissimilarity between singly- and doubly-peaked Ly$\alpha$ is that doubly-peaked Ly$\alpha$ is only detected up to $\sim 6300$ Å, whereas singly-peaked Ly$\alpha$ is detected up to $\lessapprox 9000$ Å. The reason for this is that the LAE selection from Table 5.1 only has doubly-peaked LAEs up to $\sim 7000$ Å, and even in the total catalog from BA23, only two additional LAEs slightly exceed this wavelength and one more LAE is found near $\sim 7900$ Å.

## 5.4 Attributes of Ly$\alpha$

One of 3DMTO's benefits is the shape attributes it can compute from the segmentation of a detection. We show a scatter plot matrix of four scale-invariant shape attributes and their "scale" (num_voxels) in Figure 5.5 to show that the cross-matched Ly$\alpha$ inhabit specific regions of attribute space, distinct from the total sample of detections. The attributes selected here are not unique in showing that Ly$\alpha$ has distinct attributes, but their

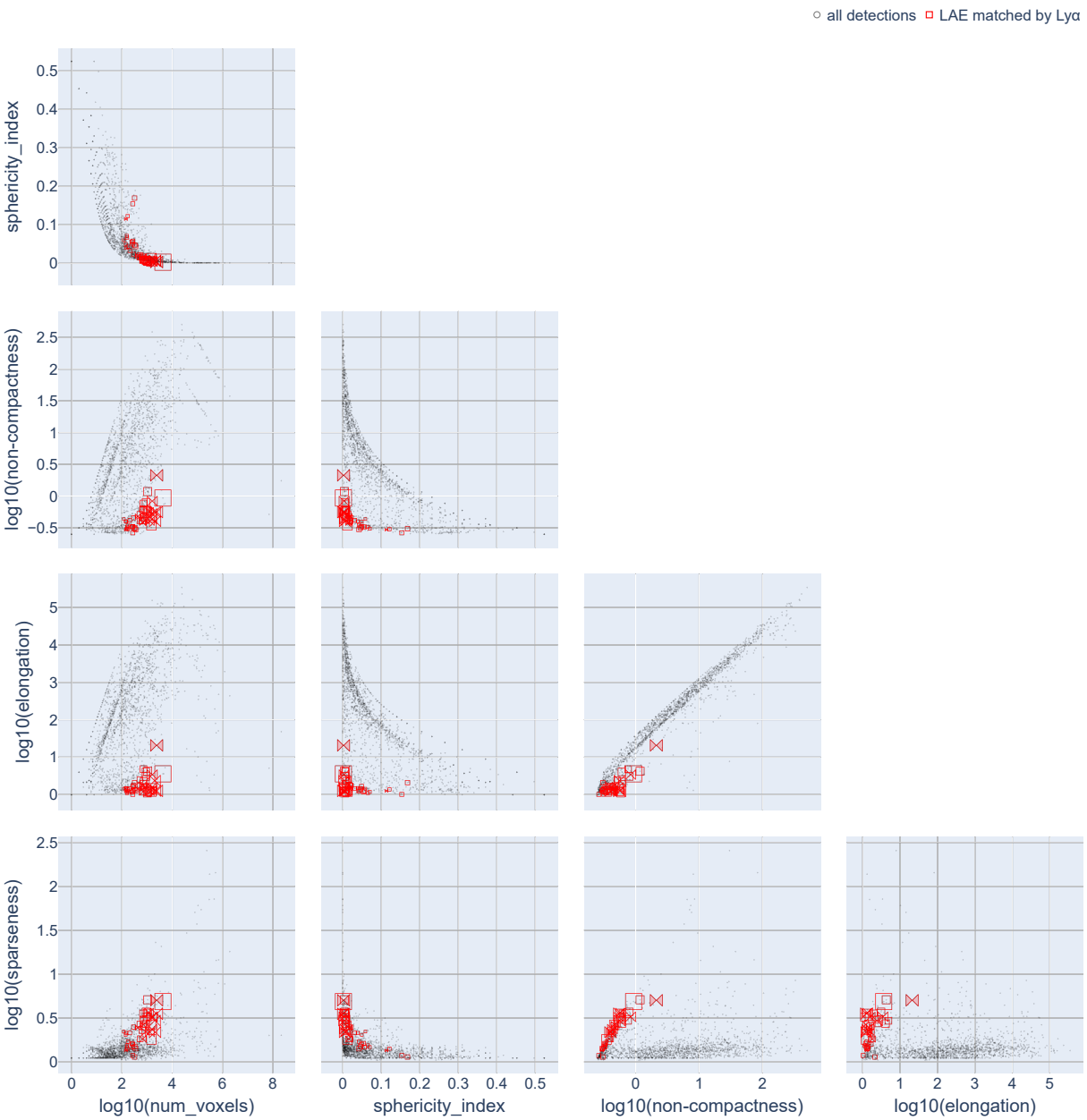


Figure 5.5: Scatter plot matrix comparing shape attributes (see Section 4.2) of 3DMTO detections that were 3D matched to the Ly$\alpha$ line of an LAE from BA23 (□ and ⋈ markers) to all 3DMTO's detections (○ marker). The □ and ⋈ markers indicate singly- and doubly-peaked LAEs respectively from the catalog selection presented in Table 5.1. The ⋈ filled in red shaded markers in each panel indicate the peculiar cross-match. The marker size scales with the number of voxels segmented by 3DMTO.

correlations are among the most prominent in showing this distinction in these data. Especially prominent are

the bimodalities in $\log_{10}$(sparseness) vs. $\log_{10}$(non-compactness) and $\log_{10}$(sparseness) vs. $\log_{10}$(elongation), as well as the separation in $\log_{10}$(elongation) vs. sphericity-index and $\log_{10}$(non-compactness) vs. sphericity-index. The bimodality in $\log_{10}$(sparseness) vs. $\log_{10}$(non-compactness) is particularly strong, even implying that for the same non-compactness, Ly$\alpha$ uniquely attains the highest sparseness. Moreover, for the total sample of detections, non-compactness and elongation are highly correlated, but Ly$\alpha$ detections deviate from this trend, resembling another bimodality. At the same value for elongation, Ly$\alpha$ is generally found to have the highest non-compactness and num_voxels. Similarly, at the same non-compactness, Ly$\alpha$ detections have the largest num_voxels, i.e., the largest segmentation. This disposition does not persist for sphericity-index and sparseness, which are both sandwiched between the total sample of detections.

Where Ly$\alpha$ detections as a whole are limited to a specific region of attribute space, there is no clear separation between singly- and doubly-peaked Ly$\alpha$. Remembering that only one peak may be segmented for a doubly-peaked LAE, and the shape attributes are not flux-weighted, it is not surprising that the shape attributes for singly- and doubly-peaked Ly$\alpha$ are not dissimilar.

Except for the doubly-peaked detection found with a negative velocity offset,[19] doubly-peaked Ly$\alpha$ does appear to be limited to a subregion of the attribute space of singly-peaked Ly$\alpha$, generally found at higher sparseness, and more stringently confined to a lower sphericity-index and higher num_voxels. However, this could simply be due to the smaller sample size of doubly-peaked Ly$\alpha$ (14) compared to singly-peaked Ly$\alpha$ (31), or from the segmentation *bleeding* closer to the line center ($v_{\mathrm{Ly}\alpha}^{trough}$ in Figure 1.2) for doubly-peaked Ly$\alpha$, if the flux level is high enough for the power attribute to still be significant. Another factor could be MUSE's spectral resolution, which roughly doubles over the entire wavelength coverage from R $\lesssim$ 2000 to R $\lesssim$ 4000 (Richard et al., 2021a), altering the observed line profile (Verhamme et al., 2015), which in turn could alter the voxel segmentation for the exact same line observed at different redshift. This could explain why singly-peaked Ly$\alpha$, which is detected out to comparatively higher redshifts, inhabits a larger region of attribute space. If properly segmented doubly-peaked Ly$\alpha$ occupies a distinctly different region of attribute space is unknown.

[19] The, in many panels, lonesome $\bowtie$ red shaded marker in Figure 5.5.

# 6 Discussion

In the preceding chapter, we showed that 3DMTO only detects $\sim 30\,\%$ of all the LAEs in the BA23 MXDF catalog. Moreover, the flux and S/N obtained by 3DMTO for these LAEs are significantly underestimated compared to the catalog. However, the coordinates are largely in agreement between 3DMTO's detections and the catalog. And compared to the total sample of detections, Ly$\alpha$ detections appear to reside in a localized region of attribute space that may allow for selective filtering.

The sources from the BA23 catalog and significance level $\alpha$ used in Chapter 5 are discussed in Sections 6.1 and 6.2 respectively. Section 6.2 furthermore showcases the robustness of attributes as a function of $\alpha$. In Section 6.3 we describe the WEAVE LIFU datacube, and Section 6.4 details how MTO was adapted to accommodate for this data and discusses an alternative background variance estimation approach. Section 6.5 discusses alternatives to the classical connectivity and how to incorporate absorption. Then Section 6.6 discusses the appropriateness of the $\chi^2$ assumption and how the significance test may be altered to improve detection performance and flux recovery. The interpretation of the attributes presented in Section 4.2 are elaborated upon in Section 6.7, and Section 6.8 describes the visualization, purity, completeness, and recall of the detections. Section 6.9 finalizes the discussion by describing the computational performance of 3DMTO.

## 6.1 Catalog (mis)matching

The following subsections will discuss which sources from the BA23 catalog and which 3DMTO detections are considered for the comparison in Chapter 5, as well as detailing the difference in how the centroids were obtained. All **BOLD** faced text corresponds to a column name from the BA23 catalog.

### 6.1.1 Sources dismissed outright

The total catalog by BA23 contains sources from three different datacubes, contained in a $\sim 3\farcm0$ x $3\farcm0$ MOSAIC footprint, within which the two smaller partially overlapping MXDF and UDF-10 field lie (BA23, their Fig. 2). Sources can be detected in multiple datacubes, but the catalog is made up of sources from data with the greatest depth.

Therefore, at the edges of the MXDF, where the exposure time can be lower than that of the other two fields, detections by 3DMTO in the MXDF datacube cannot be directly compared. Detections with an angular separation larger than $40\farcs0$ from the field center celestial coordinates (RA, DEC) = ($53\fdg164\,67$, $-27\fdg785\,37$) (J2000 FK5) (BA23) are removed. This removed 50102 detections from the 52000 total detections by 3DMTO. Of these discarded detections, $\sim 34\,\%$ consisted of only a single voxel, $\sim 60\,\%$ contained fewer voxels than the MXDF PSF, and $\sim 90\,\%$ contained fewer voxels than the LAE with the lowest number of voxels detected. The majority of detections were therefore dubious at best. Presumably, the reason there are so many (tentative) detections is due to the dither strategy resulting in mosaicing edge effects introduced by the rapidly varying exposure time in the outer edges of the MXDF footprint (top right panel in Figure 5.1). As a consequence, on the boundary of dithered exposures, jumps in IVAR (and possibly also intensity) can result in regions with artificially high power that makes them significant enough with respect to the local background to be detected as objects by 3DMTO.

Furthermore, to keep the comparison consistent, we only consider BA23 catalog sources that fall within the aforementioned angular cut. This decreased the number of catalog sources for **DATASET** = "MXDF" down to 661 from 664.

### 6.1.2 Catalog cuts

To ensure we cross-match only LAEs from a single detection method, we clarify two more catalog cuts performed in Table 5.1 in the following two subsections.

#### *Reference spectrum extraction*

BA23 used three separate extraction methods, ORIGIN, ODHIN, and narrowband extraction (NBEXT), from which the source properties are derived using pyPlatefit. In order to keep comparisons consistent, we opted to only compare against the ORIGIN reference extractions (**FROM** = "ORIGIN"), which together with NBEXT are favored over ODHIN extractions for LAEs. ODHIN uses ancillary *Hubble* space telescope (HST) photometry besides the MXDF datacube, giving it an unfair advantage that complicates attempts at direct comparison with 3DMTO. Moreover, the source properties for the majority of LAEs are predominantly derived using ORIGIN's reference extraction (see Table 5.2).

#### *Redshift confidence*

The redshift confidence **ZCONF** takes on the value 1–3 with 1 being low confidence and 3 high confidence. At **ZCONF** = 1, the redshift solution may not always be correct, and an LAE cannot unequivocally be claimed to be detected. For Ly$\alpha$, a **ZCONF** = 2 implies $(S/N)_{Ly\alpha} > 5$ and an asymmetry and width characteristic of Ly$\alpha$ line morphology (e.g., Figure 1.2). These conditions clearly identify the line as Ly$\alpha$ and thus the source as an LAE (if $EW_0(Ly\alpha) < -20$ Å) and thus **ZCONF** is set to $\geq 2$. Moreover BA23 "do not consider the difference between confidence two and three to be critical."

### 6.1.3 Centroid matching

The cross-matching hinges on the fact that the centroids are comparable between 3DMTO and BA23. Overall, the centroid comparison in Section 5.3 shows that this is the case. The cross-match limits are quite robust, i.e., increasing the spatial and/or spectral separation by $\sim 2$x hardly increases the number of detections (see Section 6.8.2).

#### *RA and DEC*

3DMTO does not detect sources outright but emission features, as does ORIGIN, but where ORIGIN also merges detections into sources, 3DMTO currently does not. Therefore, 3DMTO defines the 3D centroid of an LAE based on the centroid of its corresponding Ly$\alpha$ emission feature. BA23 however do not define their 3D centroid based on the Ly$\alpha$ emission line. Moreover, spatially the centroid is determined from a significantly spectrally extended image, obtained by convolving the datacube with *Hubble*'s Advanced Camera for Survey (ACS) *F775W* transmission filter in the spectral direction and the HST ACS PSF in the spatial direction thereafter (BA23, Sec. 4.1). Subsequently, the centroid was obtained from the convolved image by running SExtractor, tuned to match the HST segmentation maps.

Similarly to 3DMTO's Equation 4.2, SExtractor uses the first order moments to obtain the barycenter $x, y$ pixel coordinates,[20] from which the corresponding right ascension and declination can be recovered using the WCS.

For an LAE, Ly$\alpha$ is often also the only prominent detectable emission line at high redshift in the observed optical. In these cases, Ly$\alpha$ is the only signal that biases the centroid – provided that the Ly$\alpha$ line is within, and the continuum is spatially consistent over, the entire spectral coverage of the *F775W* filter.[21] Ribeiro

[20] https://sextractor.readthedocs.io/en/latest/Position.html#barycenter-x-y

[21] At these redshifts, the *F775W* filter captures the UV-continuum of LAEs.

et al., 2020 found that for LAEs with offset Ly$\alpha$ emission, the median, and 16th and 84th percentile Ly$\alpha$-UV-continuum offset is $1.1^{+1.3}_{-0.8}$ pkpc, with the extent of the average offset for LAEs being close to independent of redshift (Lemaux et al., 2021). But overall offsets are not expected to be severe in the MXDF data, with extreme cases likely attributable to mergers or satellite galaxies (BA23, Sec. 6.5).

Nonetheless, Ly$\alpha$ can be detected out to ∼10x the UV-continuum size and exceed 10 pkpc in exponential scale length (Leclercq et al., 2017). Taking all the above in mind, we take a generous $1''$ cross-match limit that ranges from 8.0 pkpc to 5.7 pkpc over the Ly$\alpha$ redshift range of the MUSE instrument. We find for the detected LAEs that the centroid offsets are $0.8^{+1.8}_{-0.5}$ pkpc, but offsets go up to ∼ 5.3 pkpc, which may indicate that some offsets are influenced by mergers or satellite galaxies.

#### *Redshift*

The two peaks of Ly$\alpha$, regardless of detecting one or two peaks, are spectrally considerably offset with respect to the systemic redshift (Section 1.2; Verhamme et al., 2018), so a detection of Ly$\alpha$ by 3DMTO does not correspond to the systemic redshift. In order to cross-match along the spectral axis, we therefore convert the reference redshift **Z** to velocity instead of **ZSYS**. To this end, we ensured that **REFZ** = "LYALPHA" (reference redshift line set) for all LAEs, which just so happens to be the case for all LAEs in the selection presented in Table 5.1.

Note that we thus only match an LAE based on the Ly$\alpha$ emission line and none (if any) of the other emission features. 3DMTO currently also does not consider any absorption features. Often times this is acceptable, as Ly$\alpha$ in emission is the only prominently detectable line at high-redshift, hence it is often used for the reference redshift despite its spectral offset.

Nonetheless, 3DMTO made a few detections that coincide with an LAE but are not cross-matched because the spectral offset is (significantly) larger than $\pm 685\,\mathrm{km\,s^{-1}}$ (□ and ⋈ markers in Figure 5.2 with coincident ∘ markers). Furthermore, 3DMTO detected separately both peaks for the doubly-peaked LAE at $(x, y) = (79, 150)$, presumably because they are both prominent.

In pyPlatefit, **Z** is determined from the peak of the line for singly-peaked Ly$\alpha$, whereas for doubly-peaked Ly$\alpha$ **Z** is determined from the center of the peak separation.[22] To account for this, we take the cross-matching velocity limit to be $\pm 685\,\mathrm{km\,s^{-1}}$, which is $5\sigma$ from the roughly $300 \pm 77\,\mathrm{km\,s^{-1}}$ systemic velocity offset determined by BA23. The aforementioned Ly$\alpha$ redshift differential also explains why compared to singly-peaked Ly$\alpha$, doubly-peaked Ly$\alpha$ is predominantly being detected at greater velocity offsets, as shown in Figure 5.4.

## 6.2 Significance level $\alpha$

The following subsections will describe what value of the significance level is used in Chapter 5, as well as show that the attributes of a detection are invariant to the significance level it is detected at.

### 6.2.1 Value of significance level $\alpha$

The significance level $\alpha$ decides which connected region should be marked an object and subsequently segmented. Intuitively, when $\alpha$ increases, it becomes easier for a region to be erroneously marked an object,[23] but decreasing $\alpha$ results in many missed detections. This first phenomenon is visually apparent in the figures of Appendix C, where for high $\alpha$ many detections appear as *confetti* that quickly dissipate with decreasing $\alpha$. Presumably there will be no value for $\alpha$ at which you have zero false detections and also a 100 % completeness

[22] https://pyplatefit.readthedocs.io/en/latest/tutorial.html#Double-peaked-{\rm-Ly\alpha}-line-profile.

[23] Type-I error: the null hypothesis was rejected when it should have been accepted, i.e., the region is mistakenly marked an object while it belongs to the background.

– there will always be a trade-off. This is further exacerbated when also considering the segmentation and boundaries of detections, important for accurate flux recovery (Haigh et al., 2021).

Teeninga et al., 2016 used a value of $\alpha = 10^{-6}$, however, this estimate was formulated on 2D images with $\sim 10^6$ pixels. The estimate depends on the number of tests performed, which is equal to the number of max-tree nodes, which in turn depends on the number of pixels (voxels in 3D). Based on the assumption of background-limited data where the background is subtracted and truncated to positive values only, the max-tree at most admits $0.5n$ nodes, with $n$ the number of voxels in the datacube. Therefore, at most there will be $0.5n$ significance tests. If the nodes are independent, an upper bound on type-I errors can be expressed as $\alpha\, 0.5n$ (Teeninga et al., 2016). If permitting no more than one type-I error, this corresponds to $\alpha \sim 10^{-8}$ for a typical WEAVE LIFU datacube.

However, Teeninga et al., 2016 showed in their testing that this upper bound was not reached. Furthermore, Barkai et al., 2023, who used the MTO implementation by Arnoldus, 2015 on H I radio cubes ($\sim 10^{-9}$ voxels), only used a significance level of $\alpha = 10^{-5}$. Datacubes derived from IFU or radio observations introduce correlations in the reconstruction process, effectively smoothing the datacube,[24] therefore violating the independence assumption. As a result, a larger $\alpha$ can be used as more voxels are connected, leading to fewer nodes to test. Another reason for the MXDF and WEAVE LIFU datacubes specifically is that not every voxel contains science data due to the spherical (top row in Figure 5.1) and hexagonal (see Figure C.2) footprints respectively. All the voxels in the spaxels in the outer regions, as well as in the spectral gap, will be attributed to the root node, further decreasing the number of nodes to test.

We have yet to confirm a detection of an LAE and its corresponding Ly$\alpha$ signal in a WEAVE LIFU datacube in order to ascertain how the instrumental response affects it. Regardless of the LAE non-detection in WEAVE LIFU data, the complexity and variety of Ly$\alpha$ lines (Verhamme et al., 2006; Blaizot et al., 2023) make producing segmentation maps beyond the scope of this thesis. Moreover, the sample of LAEs with spectra available at the spectral resolution (in excess of) and over the wavelength coverage of WEAVE is limited. Optimizing for segmentation and flux, S/N recovery is therefore not possible. However, recent efforts by the *Lyman Alpha Spectral Database*[25] (Runnholm et al., 2021) may allow for source insertion and recovery experiments (Haigh et al., 2021) specific to real LAEs (Herenz et al., 2019) or simulated ones (Drake et al., 2017; Herenz et al., 2019; Mary et al., 2020).

We used a significance level of $\alpha = 5 \times 10^{-4}$ in Chapter 5 – arbitrarily chosen based on trial and error – corresponding to a theoretical false detection rate of $0.5 \cdot 5 \times 10^{-4} \cdot 8 \times 10^8 \sim 2 \times 10^5$ detections for the MXDF datacube. We observed nowhere near this many (false) detections and retained a high purity, although not source completeness (see Section 6.8.2).

### 6.2.2 Attribute (in)dependence on $\alpha$

It is important to have a handle on how reliable the attributes of a detection are, as well as how invariant they are to the detection parameters. We showed in Section 5.2 that this first point is not satisfactory, as detections of the Ly$\alpha$ line do not accurately capture the total flux and S/N.

For a detection, increasing or decreasing $\alpha$ could move the significant node that marks an object down or up the branch respectively, similar to what `move_up` in Teeninga et al., 2016 does at fixed $\alpha$. Arnoldus, 2015 (their Sec. 5.5) mentioned that segmentation was independent of $\alpha$, and `move_up` dominates the segmentation.

To further ascertain if attributes also remain consistent for 3DMTO as a function of $\alpha$, we proceed as follows. As building the max-tree is independent of $\alpha$, and all attributes are dependent on the voxels segmented, we only need to check if the segmentation does not (significantly) change from one $\alpha$ to another. To this end, we ran 3DMTO on WEAVE LIFU `stackcube_3006749.fit` (BLUE arm) in the reduced wavelength

[24] Arnoldus, 2015 applied a smoothing preprocessing step on top of the inherent correlations present in radio cubes.
[25] https://lasd.lyman-alpha.com/

range $3600 \leq \lambda \left[\text{Å}\right] \leq 5499$ (left-most curve of BLUE arm in Figure 2.2) to diminish detections related to residuals from imperfect skyline removal, which would be far more pronounced in the RED arm. We varied $\alpha$ to obtain 16 datasets of detections with $\alpha \sim \{10^{-1}, 10^{-2}, \ldots, 10^{-16}\}$. Their segmentations are shown in Appendix C. For each dataset we 3D cross-matched the centroid within $0''.5$ angular separation and $\pm 0.5$ Å (one resolution element) to the centroids in the $\alpha = 10^{-16}$ dataset. As reducing $\alpha$ increases the rejection boundary, any detection at a lower $\alpha$ must also be detectable for a higher $\alpha$.

The left panel of Figure 6.1 shows the number of detections for each dataset (left axis), as well as the completeness of the 3D cross-match (right axis). The centroid essentially does not change as a function of $\alpha$, as $\approx 95\,\%$ of the detections for $\alpha = 10^{-16}$ are cross-matched to a detection with $10^{-1} \leq \alpha \lesssim 10^{-8}$, and the correspondence gradually increases to $\approx 100\,\%$ for $10^{-9} \lesssim \alpha \leq 10^{-15}$.

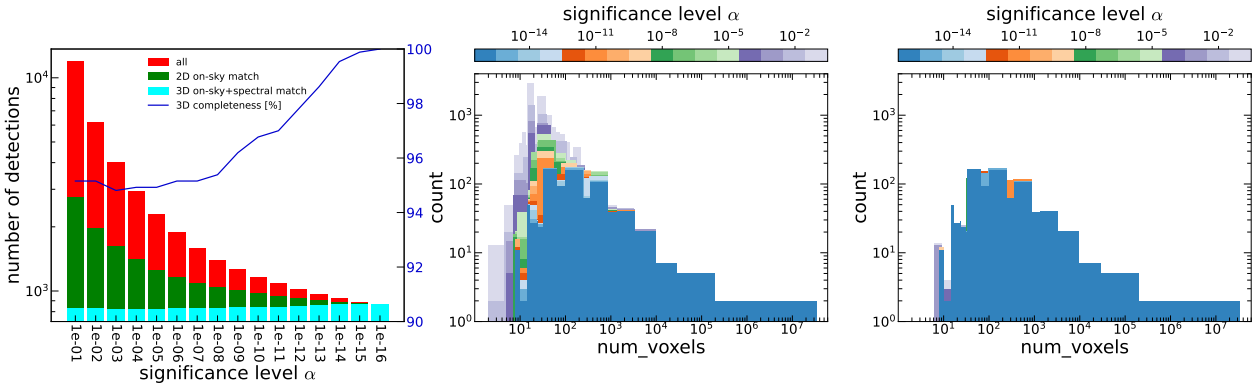


Figure 6.1: Visualizing attribute independence on significance level $\alpha$. *Left*: bar plot of the number of detections (left axis) as a function of $\alpha$ for all detections (red, X hatch pattern), and those cross-matched to a detection in the $\alpha = 10^{-16}$ dataset, either on sky only (green, – hatch pattern), or both spatially and spectrally (cyan, / hatch pattern). The 3D completeness (right axis) indicates how many of the detections in the $\alpha = 10^{-16}$ dataset are both spatially and spectrally cross-matched in each other $\alpha$ dataset. *Middle*: log-log histogram[26] of the number of detections ($y$-axis) containing a certain amount of voxels ($x$-axis) for all detections at each $\alpha$. *Right*: same ($x$, $y$ axes limits) as the *middle* panel, but only for detections 3D cross-matched to a detection in the $\alpha = 10^{-16}$ dataset. The extent of the cross-match is one resolution element of WEAVE LIFU `stackcube_3006749.fit` (BLUE arm), i.e., within $0''.5$ angular separation and 0.5 Å. The colorbars in the *middle* and *right* panel are identical and consist of 16 discrete colors, coinciding with the 16 different significance levels. The 2D on-sky match corresponds to detections possibly belonging to the same source, whilst the 3D spatial and spectral match can coincides with individual emission features.

The consistency of the centroid alone is not enough to claim $\alpha$-independence, as the segmentation could shrink such that the centroid remains the same. The middle panel shows the histograms of the number of voxels segmented for each $\alpha$. The rightmost panel shows the same, but only for the detections that were 3D cross-matched, from which can be concluded that all datasets virtually coincide with the $\alpha = 10^{-16}$ dataset. Only minor discrepancies are apparent, e.g., for num_voxels $\lesssim 10$ voxels in the high $\alpha$ datasets. But detections for these conditions should be avoided anyhow, as detections with such low num_voxels (smaller than the PSF) do not (fully) describe a source, and using a high $\alpha$ will result in more type-I errors. Considering that area($P$) is an increasing attribute, segmented voxels of a detection at a particular $\alpha$ are at the very least also included in the same object detected for a higher $\alpha$. Therefore, there is no redistribution of voxels as a function of $\alpha$ and the segmentation of significant detections is independent of $\alpha$.

The non-evolution with $\alpha$ makes 3DMTO robust, as $\alpha$ only has an effect on the number of (false) detections and not their corresponding attributes. If this is still the case when using an alternative statistical test (see Section 6.6) requires further research.

[26] The bin width varies dynamically according to the "Bayesian Blocks" fitness function to accommodate for the large range in *num_voxels*. For further details see https://docs.astropy.org/en/stable/visualization/histogram.html#bayesian-models.

### 6.2.3 Detections and attributes as a function of $\alpha$

Figure 6.1 shows that the total number of (false) detections gradually decreases with decreasing $\alpha$. Following a similar decrease, the 2D on-sky cross-match (green, – hatch pattern in left panel of Figure 6.1) shows that at higher $\alpha$, 3DMTO finds increasingly more detections along the spectrum of a source. Some of these could correspond to emission lines that are only significant up to an $\alpha < 10^{-16}$.

The attribute space occupied by sources also changes as a function of $\alpha$. Figure 6.2 shows that the evolution of attribute space affects all attributes, where the dark purple detections in large correspond to the 3D cross-matched sources from the prior subsection. The tiny confetti detections seen in Figures C.2–C.4 largely correspond to the detections at low $\log_{10}$(num_voxels), but are not significantly different to the attribute space occupied by detections at a lower $\alpha$, relative to the separation seen in other panels. The most distinctive separation is seen for SNR, which shows a relatively clean horizontal and vertical cut as a function of $\alpha$ for the row and column corresponding to $\log_{10}$(SNR) respectively. This is not surprising given that SNR is related to the equation for power.

Furthermore, $\log_{10}$(elongation), and to a lesser extent $\log_{10}$(non-compactness), appear to be bimodal when graphed against $\log_{10}$(num_voxels), $\log_{10}$(flux), and $\log_{10}$(SNR) for all $\alpha$. What underlying sources correspond to which region of attribute space is yet to be explored. Moreover, the sphericity-index vs. the moment-of-inertia tensor planes appear to have a clear upper boundary. It primarily evolves as a function of $\alpha$ for $\log_{10}$(flatness), and remains fairly constant for the other three attributes. The detections appear to be most loosely constrained by sphericity-index vs. $\log_{10}$(flatness), followed by $\log_{10}$(flatness) vs. $\log_{10}$(sparseness). A bimodality is also observed between the comparisons of all four moment-of-inertia tensor attributes (bottom right corner of Figure 6.2). This bimodality does evolve with $\alpha$, where the majority of detections with low moment-of-inertia tensor attribute values disappear with decreasing $\alpha$, while the detections with larger attribute values all remain for each $\alpha$.

## 6.3 Reconstructed WEAVE LIFU datacube

Ultimately, the WEAVE LIFU datacubes need to be reconstructed from observations captured on a 2D CCD. The spatial and spectral axes introduce local correlations due to rebinning, which result in co-variances (Bacon et al., 2017; Herenz, 2023). Because it is computationally expensive to propagate the entire covariance matrix, the current generation of data reduction (pipelines) may account for it through empirical rescaling of the noise datacube, estimated from pixel-to-pixel variations (Bacon et al., 2017; Herenz & Wisotzki, 2017). We have not accounted for this effect for any of the WEAVE LIFU datacubes used in this thesis, and therefore underestimate the amplitude of the noise by some multiplicative factor (Herenz, 2023). The WEAVE pipeline will account for such covariance when the calibration process is complete (Trager, personal communication).

### 6.3.1 Effect of dithering

Because the filling factor of the WEAVE LIFU is only $\sim 55\,\%$, a particular region on the sky needs to be dithered in order to be fully observed (see inset Layer 3 of Figure 2.1; for a larger version see Figure 17 of Jin et al., 2024). Besides covering the entire region observed on the sky, numerous spaxels will be fed by multiple overlapping fibers, up to the number of dithers taken. As a consequence, not every spaxel in the datacube is exposed the same amount, with the majority of spaxels exposed by a single fiber. The dither and resulting effective exposure pattern are known however and essentially encoded in the IVAR datacube (see the middle panel of Figure 6.3).

In the following, we assume a three-point dither pattern is used for the WCCS. The WEAVE LIFU has $2\farcs6$ diameter fibers, which are dithered in a triangular pattern such that the separation of the same fiber with each exposure is $1\farcs6$. Because the datacube has a spatial pixel scale of $0\farcs5$, which is considerably smaller than a fiber, locally there will be spaxels fed by one and the same fiber, i.e., these spaxels are identical. The FSF

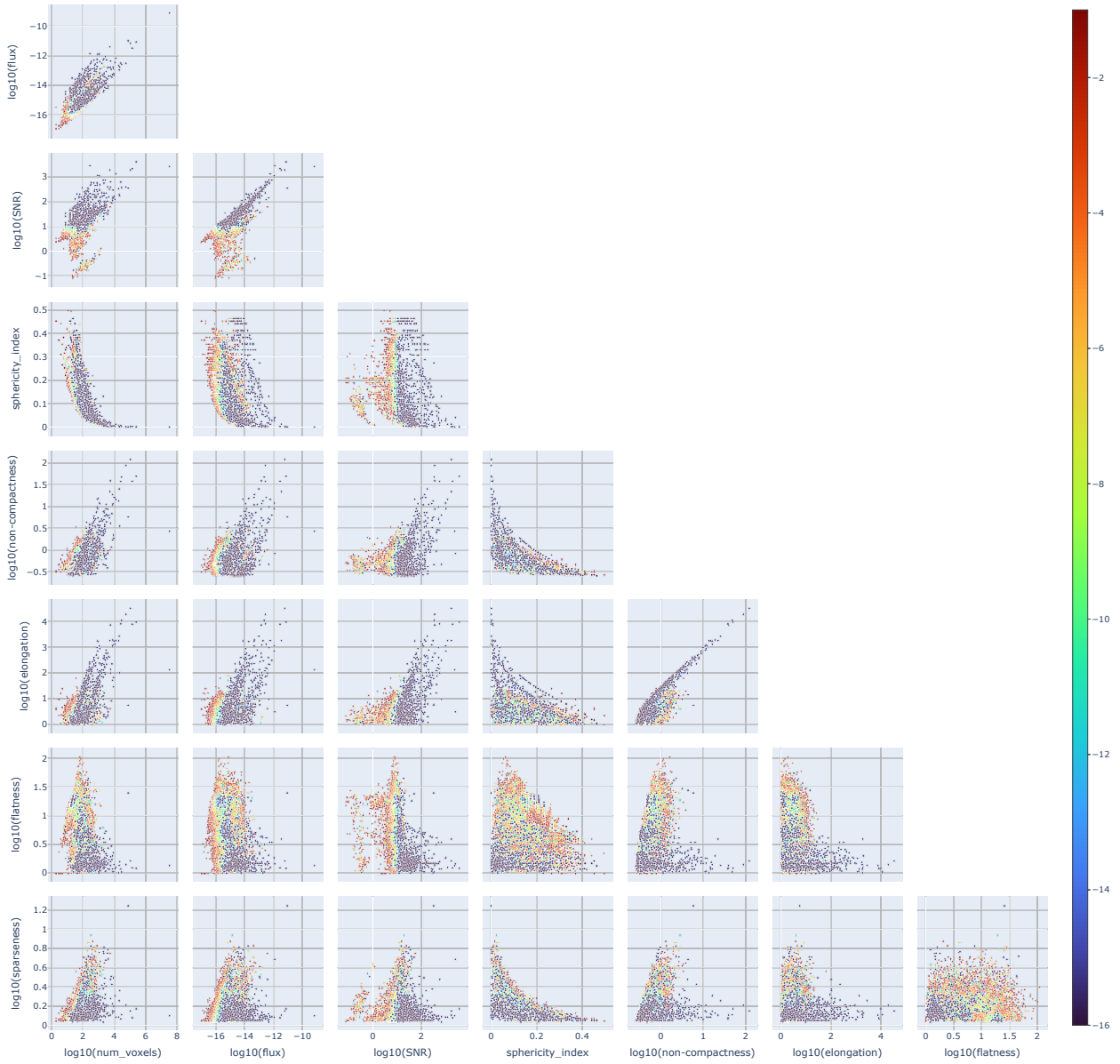


Figure 6.2: Scatter-plot matrix of WEAVE LIFU `stackcube_3006749.fit` (BLUE arm) of various attributes for $\alpha$ in $10^{-16}$–$10^{-1}$, as indicated by the color scale.

is $\sim 1''.6$, constant in the field of view, and slightly hexagonal-shaped with an acute boundary, i.e., one does not need to extend far beyond the FWHM to contain all the light of an FSF-limited source (Trager, personal communication). The LSF for a single-mode fiber fed IFU is Gaussian-like (Robertson, 2013) and for the WEAVE LIFU has a FWHM of $\sim 1.7$ Å and $\sim 2.75$ Å in the BLUE and RED arms respectively. The variation with wavelength in the LSF is yet to be precisely determined but is pretty constant in the BLUE arm based on preliminary inspection.

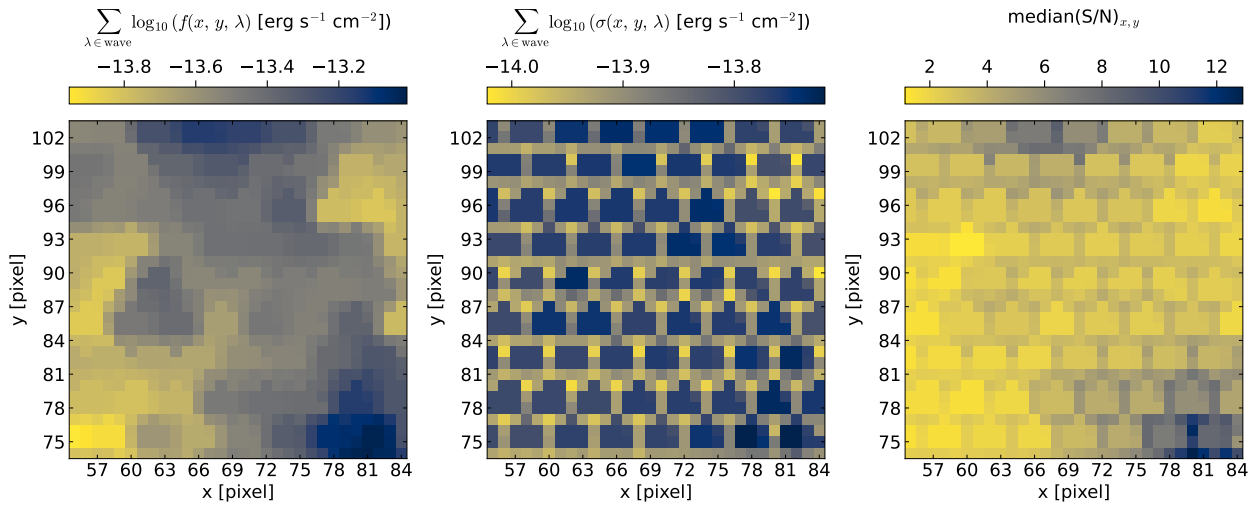


Figure 6.3: Effect of the three dither pattern utilized in the WCCS on WEAVE LIFU `stackcube_3006748.fit` (RED arm). The flux (left), noise (middle), and SNR (right) are aggregated over the entire wavelength range. The flux and noise are summed along each spaxel, and for the S/N we show the median in each spaxel.

## 6.4 Adapting MTO to IFU data

Although MTO is independent of the dimensionality of the underlying data, certain assumptions are nonetheless to be adhered to. For any voxel $x$ in node $P$ we denote the local background variance as $\sigma_{\text{bg-local}}(x)$, and the total variance as $\sigma_{\text{tot}}(x)$. In prior implementations of MTO for optical data, the assumption of background dominated Poissonian noise and constant background value/variance were excellent approximations. This allowed for the following separable definition of the local background variance: $\sigma^2_{\text{bg-local}}(x) = \hat{\sigma}^2_{\text{bg}} + \textit{Poisson noise local background}$, which is constant for node $P$, with $\hat{\sigma}^2_{\text{bg}}$ the constant global background variance (Teeninga et al., 2016).

Considering only the spatial dimension in IFU data, this assumption is not necessarily violated. Herenz, 2023 found that the variance in MUSE datacubes is constant as a function of position (i.e., constant in each spectral plane),[27] however the varying effective exposure time as a function of position in WEAVE LIFU datacubes violates this assumption (Section 6.3.1). Moreover, the $\hat{\sigma}^2_{\text{bg}}$ assumption is invalid for any spectroscopic instrument, as the background variance as a function of wavelength is strongly non-uniform due to skylines and in the neighborhood of bright continuum sources (Herenz & Wisotzki, 2017; Herenz, 2023).

As it is impossible to decompose the local background variance into its constituents without further assumptions, the power (Equation 4.1) needs to be adjusted to include the normalization with the variance inside the summation. To achieve this, we utilize the IVAR datacube that encodes the noise from the background, signal, non-uniform components, and the effective exposure time.[28]

While it is not possible to assume a constant background variance that is valid for the entire datacube, locally an average constant background variance could be considered (Herenz & Wisotzki, 2017) and may be estimated from a descendant node. This would effectively recover the normalization for power as presented in Teeninga et al., 2016, where $\sigma(x) \Rightarrow \sigma_{\text{bg-local}}(x)$ in Equation 4.1. The voxels to which the signal itself belongs obscure, and blend with, the variance contribution of the background. Therefore, the variance contributions are indiscernible without further information. Any descendant node(s) brings with it voxels unique to said node(s), from which $\sigma_{\text{bg-local}}(x)$ can be estimated in some way. These unique voxels at best

[27] If the recommended dithering and rotation strategy is followed.

[28] An important noise component missing for WEAVE LIFU datacubes is the covariance introduced in the reconstruction process mentioned in Section 6.3.

encapsulate all voxels of nodes contained within, but at worst are all biased to one side by a gradient, e.g., due to a (blended) (bright) neighbor or varying continuum. A max-tree inherently does not deal with gradients in this way, because it is built up out of a threshold set of connected voxels at the same intensity. Preferentially, we want to estimate $\sigma_{\text{bg-local}}(x)$ only with unique voxels uniformly detached from the source segmentation but close enough to diminish bias from nearby sources, yet still contribute enough voxels to determine a reliable estimate. Whether this background variance estimation is a viable strategy needs to be further explored.

## 6.5 Adapting the (max)-tree to improve detection and extraction performance

Prior implementations of MTO have all been predominantly concerned with emission. However, the (increased) spectral resolution in optical data allows for both emission and absorption to be studied. The Ly$\alpha$ line is substantially affected by resonant scattering, resulting in (occasionally) two detectable spectrally separated peaks. The separation implies that the max-tree, using a traditional 6-connectivity, will not connect the voxels of the two peaks for flux in excess of that found at $v_{\text{Ly}\alpha}^{\text{trough}}$ in Figure 1.2 (Salembier & Wilkinson, 2009). Moreover, continuum sources may be broken up by absorption features, noise spikes around the outskirts of an emission line at flux levels lower than that of the node marking an object will not be connected, and over-subtraction artifacts like skyline residuals can affect both cases.

To ameliorate this disconnectedness, a *second-generation connectivity* (Salembier & Wilkinson, 2009) that connects signal over gaps in the data is needed. This type of connectivity is referred to as *clustering*-based. Arnoldus, 2015 already utilized such a connectivity for MTO, using a *masked-based connectivity* where the datacube has undergone some arbitrary transformation (Ouzounis & Wilkinson, 2007). More specifically, Arnoldus used *mask-like connectivity*, in which the max-tree is built on a filtered version of the datacube, while the data of the original datacube are used to compute attributes. This way the max-tree is built from a datacube that accentuates and connects the features of interest, while the statistics are computed from the original datacube, required to uphold the validity of the $\chi^2$-test and use of the power attribute (Equation 4.1).

The mask $M$ to build the max-tree from can be obtained by any means, as long as it lives in the same coordinate volume $V$ as the original datacube $D$. Considering we require regions to be connected over gaps in signal, obtaining $M$ by applying an extensive operator to datacube $D$ is most natural. One such operator is the *closing*: $D \bullet B$, where $B$ is a structuring element that governs the maximum extent over which gaps in the signal are connected (Najman & Talbot, 2010). Which specific operation would be best at connecting the regions of interest but does not merge entire sources (which already occurs, see Section 6.8.1) requires further research. Applying the operator to the spectral axis only would connect Ly$\alpha$ peaks while leaving nearly spatially blended sources detached, although care has to be taken in regions with skyline residuals that may also be merged. It may also be interesting to apply the filtering on the counts datacube (before applying the sensitivity response function) or the S/N datacube (which is invariant to the sensitivity response function) to obtain the mask.

Along the spectral direction, a closing-like operator will also fill up absorption features that currently break up a galaxies' continuum, allowing these separated fragments to correctly be connected into a single object. But in order to detect the absorption features directly, we could utilize a *black* top-hat transform $T_b(D) = (D \bullet B) - D$, i.e., the voxel-wise difference between the closing of the datacube and the original datacube (Najman & Talbot, 2010). The transformed datacube has suppressed all emission and transformed the absorption features into emission peak analogues. Running 3DMTO on $T_b(D)$ should then provide detection and extraction of only the absorption features. Unfortunately, this does mean one would have to run 3DMTO once for emission and once for absorption, increasing computation time. However, the datacube is still truncated to positive signal only, implying that the number of nodes in the max-tree of $T_b(D)$ is significantly reduced. This is because only (significant) nodes are computed where there is continuum absorption or a large enough continuum for the negative noise spikes to still be positive.

The max-tree has a min-tree counterpart by the duality $D \longleftrightarrow -D$ (Salembier et al., 1998), describing

darker regions instead of brighter ones, i.e., absorption features instead of emission features. Considering it is inefficient to have to run 3DMTO once for emission and a second time for absorption, another approach could be using the Tree-of-Shapes (Monasse & Guichard, 2000). The Tree-of-Shapes is effectively a merging of the min- and max-tree, thus describing both emission and absorption features. The tree of shapes is a contrast-invariant *self-dual* representation of the datacube (Salembier & Wilkinson, 2009), and is therefore best applied to a continuum-subtracted datacube.

Further research is required to assess the validity of detecting absorption using the approaches discussed, as well as which datacube transformation is best suited to improve detection performance.

## 6.6 Significance tests

Returning to the current implementation of 3DMTO, the significance test is used to decide if a node corresponds to an object, or if it conforms with the expected background distribution. MTO assumes the power is (locally) $\chi^2$-distributed, such that the ICDF$\chi^2(1-\alpha, \nu)$ is an appropriate rejection boundary for the $\chi^2$-statistic. For any node that contains signal, $\sigma_{\text{tot}}(x)$ overestimates the local background variance $\sigma_{\text{bg-local}}(x)$ and therefore Equation 4.1 would underestimate the $\chi^2$-statistic. Additionally, the noise properties in the spectral direction are non-uniform due to telluric line and continuum emission, violating the background-limited assumption in those regions (Section 1.3.1). Moreover, the $\chi^2$ distribution only holds exactly for the nodes that have parent$(P)$ = root (Teeninga et al., 2016). A $\chi^2$-test is therefore perhaps not entirely appropriate.

All the aforementioned issues separately act to artificially increase the effect of the ICDF$\chi^2$ rejection boundary. This will curb the number of false positives, but also increases the number of nodes erroneously marked insignificant. Teeninga et al. introduced "powerAlt", in conjunction with three additional significance tests, to combat this. powerAlt is identical in form to Equation 4.1, but instead of using the direct parent$(P)$ to determine the local background level, the first significant ancestor node $P_{\text{anc}}$ is used. The reasoning was to make the significance level independent of the height of a node in the tree. At best parent$(P) = P_{\text{anc}}$, and at worst parent$(P)$ maximally overestimates the local background level: altitude(parent$(P)$) $\gg$ altitude$(P_{\text{anc}})$. Which in term minimizes the power and therefore powerAlt$(P) \geq$ power$(P)$.

The use of power$(P)$ instead of powerAlt$(P)$ is most likely the cause of the flux and S/N deficit observed between 3DMTO and BA23 in Section 5.2. Figure 6.4 shows the recovered flux and S/N of 3DMTO without subtracting the local background (i.e., no continuum subtraction) compared to the same BA23 catalog quantities as in Figure 5.3, which are continuum subtracted. In Figure 5.3, the majority of 3DMTO flux and S/N lies below the one-to-one relation, whereas in Figure 6.4 the flux and S/N conform much better to the one-to-one relation, albeit with considerable scatter.

Using powerAlt$(P)$ instead of power$(P)$ could increase the object flux in two ways: one is that the local background level may be lower (altitude$(P_{\text{anc}}) \leq$ altitude(parent$(P)$)), and secondly following from that is that the significant node marking an object can be at a lower altitude further down the branch.

When a node marking an object is moved further down the branch, its flux will increase, but so will its segmentation. Supposing the node marking an object does not change when using $P_{\text{anc}}$ as opposed to parent$(P)$, i.e., segmentation remains the same, then altitude$(P_{\text{anc}}) \leq$ altitude$(P)$, and the local background level can only increase both the flux and S/N. However, the second flux contribution comes from moving the node marking the object further down the branch, increasing the voxel segmentation, which therefore also introduces additional noise. Further research is required to see how these two contributions balance, but presumably using $P_{\text{anc}}$ as opposed to parent$(P)$ improves the correspondences for the flux and S/N to their respective one-to-one relations.

We also inspected the 3D segmentations of 3DMTO Ly$\alpha$ detections to rule out over-segmentation (i.e., the signal is broken up) as the cause, or significant contributor of, the flux and S/N deficit. In Section 5.2 we showed that the vast majority of 3DMTO detections underestimated the flux, but their segmentations do not appear to under-represent the signal, as seen from a few example 3D segmentations shown in Figure B.1.

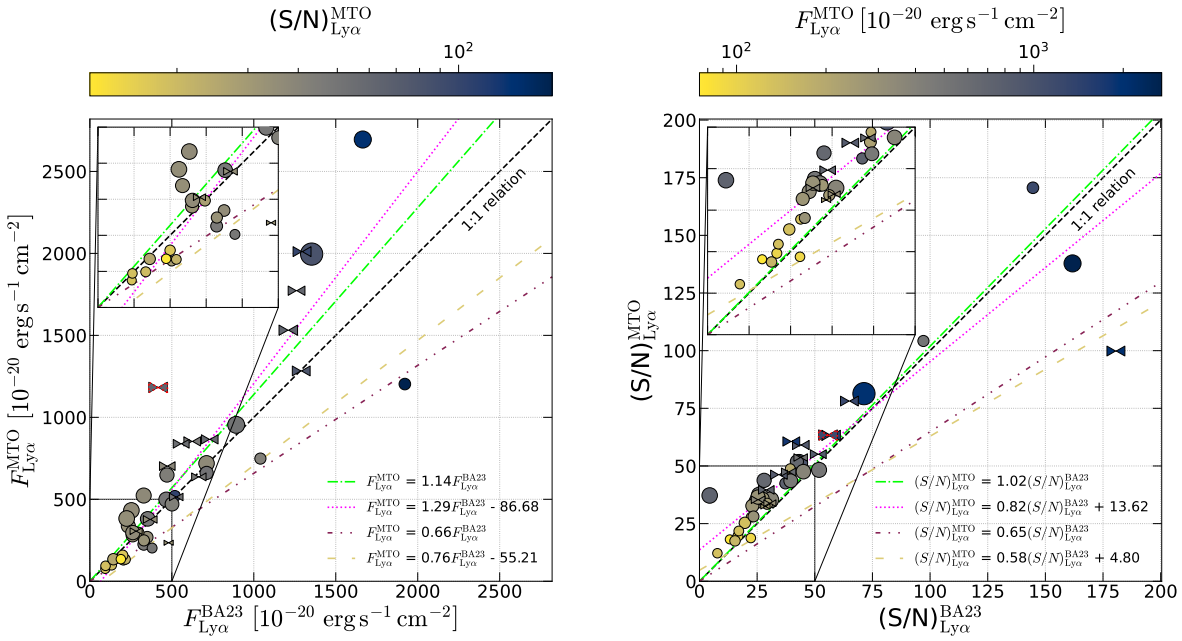


Figure 6.4: Same as Figure 5.3 but using the total flux recovered by 3DMTO, i.e., no local background (continuum) subtraction. For comparison, the purple dash doubly-dotted and yellow loosely dashed legend entries respectively show the equations of the linear ODR fits with the intercept fixed at the origin or as a free parameter from Figure 5.3.

On the other side of the one-to-one relation, the peculiar Ly$\alpha$ detection (▶◀ marker with red dotted outline) is one of the three detections that had a 3DMTO flux in excess of that reported in the catalog. Figure B.2 shows how the excess is attributable to under-segmentation, where the connectivity found a path of voxels away from the signal at high enough intensity for the object to still be significant. It also explains why the detection remains largely isolated in attribute space (Figure 5.5), allowing for possible attribute filtering of these erroneous segmentations. Moreover, it explains why it has the highest velocity offset ($\sim -600\,\mathrm{km\,s^{-1}}$) as the additional voxels skew the centroid further, interestingly, into the IGM suppressed blue part of the electromagnetic spectrum.

Coming back to alternatives to the power($P$) attribute, any hypothesis test using any kind of attribute for which the distribution under the null-hypothesis is known could be used to determine significant nodes to filter the max-tree with (Jones, 1999). Besides the power(Alt) attributes, Sec. 5 of Arnoldus, 2015 discusses some alternative attributes and accompanying statistical models considered for MTO, geared towards but not all specific to radio datacubes. The benefit of the ICDF$\chi^2(1-\alpha,\nu)$ is that it has an analytical form. Any non-analytical rejection boundary will have to be sampled for each significance level using for example Monte Carlo simulations (Teeninga et al., 2016). However, Haigh et al., 2021 found that MTO is consistent across various datasets when using significance test 4 of Teeninga et al., 2016, requiring only small parameter adjustments of MTO's already limited set of parameters.

The benefit of these sampled distributions is that they do not make assumptions about the data, as they are generated from the data. Moreover, we could adjust the hypothesis test to factor in emission line (e.g., in similar vein to ORIGIN, Mary et al., 2020) attribute values, or even (doubly-peaked) Ly$\alpha$ in specific, such that noisy nodes and nodes corresponding to entire sources are rejected. However, this does remove the current morphologically independent voxel representation of a signal by requiring a certain belief about what the signal should look like in the datacube.

## 6.7 Descriptive attributes

Because 3DMTO segments as an integral part of its detection algorithm, it allows for the computation of the flux, morphological shape attributes, and other attributes. The accuracy of these attributes hinges on the segmentation being appropriate. Haigh et al., 2021 found that the 2D implementation of MTO outperforms other common source-extraction tools utilized in 2D photometric data, and Barkai et al., 2023 showed that MTO's segmentation is comparable to other source-finding techniques used in HI radio datacubes.

It also appears that the segmentation is consistent across datasets. Some attributes are instrument specific and depend on the PSF as well as the spatial and spectral resolution, e.g., num_voxels and SNR. But despite vast differences in the instruments and data depth, the shape attributes of MXDF detections shown in Figure 5.5 remain in large part consistent with the attributes from detections obtained from a WEAVE LIFU datacube at similar or lower $\alpha$ (Figure 6.2).

### 6.7.1 Interpretation of attributes

For any particular source, the 3D voxel representation does not resemble a physical structure, so referring to shape attributes in a physical sense is unwarranted. As an example, for a detection corresponding to a source covering the entire wavelength range, the voxel length in the spectral direction is bound to be longest ($|\lambda_1(P)| > |\lambda_2(P)|, |\lambda_3(P)|$). For an emission feature however – depending on the spatial/spectral resolution, LSF, and FSF – it is plausible that the spatial voxel extent is more extended than the spectral voxel extent ($|\lambda_2(P)|, |\lambda_3(P)| > |\lambda_1(P)|$). As the flatness attribute is also computed as a ratio of eigenvalues, it is similarly affected and the meaning of these attributes thus depends on the source underlying the segmentation. Moreover, the meaning of shape-invariant attributes will diminish if the source is morphed by lensing. Nonetheless, the non-physical nature does not mean the attributes are uninformative. It is likely responsible for the bimodality in the many 2D attribute space representations of shape attributes (see e.g., Figure 5.5), presumably corresponding to emission lines and continuum sources respectively.

There should also be a clear difference in (shape) attributes between singly- and doubly-peaked Ly$\alpha$ if 3DMTO properly segments two peaks as a single detection. Section 6.5 discussed how the signal could be recovered in full. In this case, the spectral extent of the detection roughly doubles (Figure 1.2), and under the assumption of no change in the spatial extent, the elongation or flatness will be distinctly different, depending on which voxel axis is longest.[29] Under this same assumption, the sphericity-index and num_voxels should also be lower and higher respectively. Moreover, additional attributes may also be considered that better highlight the intensity variation of doubly-peaked profiles, like the variance or other moments of the voxel distribution. If the attributes of properly connected doubly-peaked Ly$\alpha$ profiles or intensity weighted attributes occupy a new region of attribute space that may or may not overlap with non-Ly$\alpha$ detections is unknown.

Furthermore, it would be interesting to study the segmentation and attributes of the Ly$\alpha$ line for undetected LAEs and how they differ compared to Ly$\alpha$ detected as significant. As the location of these LAEs in the datacube is known from the BA23 catalog, we can recover the attributes for these sources by considering the max-tree segmentation at the corresponding coordinates. In addition, the difference with respect to other (un)detected emission lines is also worth exploring. Techniques like for example machine learning and dimensionality reduction in addition to data clean-up may aid further inference on what (sub)type of sources (or rather their emission features) correspond to which regions of attribute space. There may also be a redshift dependence on the attributes as the same source observed at different redshifts will be subject to a different resolving power, especially relevant over the WEAVE LIFU's extensive wavelength range.

[29] Remember that the ordering of the eigenvalues (which are related to the length of the segmentations along each axis) of the moment-of-inertia tensor matters (see Section 4.2.1).

## 6.8 Detection

Subsections 6.8.1 and 6.8.3 will utilize the descriptive attributes to discuss the visualization of the segmentation and (sources of) false detections respectively, and Subsection 6.8.2 discusses the completeness, purity, and recall of 3DMTO for the MXDF datacube.

### 6.8.1 Visualization

Visualizing the segmentation of a 3D object in the 3D datacube on a 2D page requires compromise. We opted to visualize the segmentation of objects using maximum intensity projection[30] (MIP; Wallis et al., 1989), such that for each pixel only the segmentation belonging to the source with the highest flux along the (aggregated) axis of the datacube is projected, i.e., "hot-spot" imaging. In 2D this suffices in showing (part of) every detection because higher-intensity detections are either isolated or nested in larger fainter segmentations. In 3D this may not suffice as a low-intensity detection may be obscured by a high intensity detection along the projection. This is especially apparent for WEAVE LIFU datacubes with their large spectral extent and relatively low spatial resolution, which makes inferring morphological details from the $x$–$y$ projection difficult (see Appendix C). This will be mitigated to some extent by showing projections along all three axes, but to completely mitigate source obscuration, an interactive exploration of the datacube in which an objects' visibility is determined by attribute filtering of the max-tree could be utilized (e.g., see Westenberg et al., 2007). To add to this, whereas other detection methods generally only provide the extraction aperture, 3DMTO can provide the entire 3D source segmentation encoded in the max-tree structure, which may be saved separately.

Figure 6.5 shows the three MIPs for the $\sim 1$ arcmin$^2$ UDF-10 field observed by MUSE for $\sim 30$ h (bottom row in Figure 5.1). In Figure 6.5b we show that 3DMTO can detect and segment the continuum of a source along the entire spectrum, which may also be isolated from other types of detections by thresholding the flatness attribute (Section 6.7). It moreover shows how imperfect skyline subtraction still causes some spectrally localized but spatially extended features to attach to the segmentation or even merge separate sources into a single detection (same color). This may be ameliorated by using a *contraction*-based mask-like connectivity (Ouzounis & Wilkinson, 2007), which may not be compatible with the clustering-based mask-like connectivity suggested in Section 6.5 to help recover all the flux of an emission line.

Emission features occurring at a specific wavelength can similarly be separated from continuum sources using the non-compactness attribute. These attribute selections are arbitrarily chosen to highlight the discriminative power of attribute filtering, but do not necessarily capture all continuum or emission features respectively.

The clear segmentation of the continuum seen for the MXDF datacube is not observed in the WEAVE LIFU datacubes (Appendix C). Here the segmentation appears significantly more fragmented along the spectral direction, presumably due to the worse noise characteristics compared to the UDF-10 datacube.

### 6.8.2 Purity, completeness, and recall

In order to estimate the detection power of 3DMTO, we define the purity and completeness as follows,

$$\text{purity}\ [\%] = 100 \times \frac{\text{matched detections}}{\text{total detections}}, \qquad \text{completeness}\ [\%] = 100 \times \frac{\text{matched sources}}{\text{total catalog sources}}, \tag{6.1}$$

where we recall that a "detection" by 3DMTO does not necessarily correspond to a "source".

We take the catalog by BA23 as the ground truth,[31] for it has been constructed from the same data we

[30] First introduced as "Maximum Activity Projection" in Wallis et al., 1989.

[31] Note however that this catalog is not complete with respect to photometric and spectroscopic catalogs within the footprint based on other data (BA23).

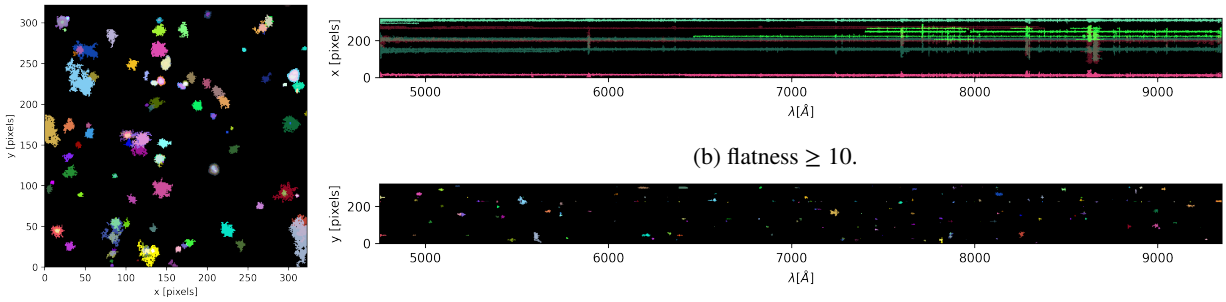


(a) non-compactness $\leq 1$.

(b) flatness $\geq 10$.

(c) non-compactness $\leq 1$.

Figure 6.5: MIP of segmentations for 3DMTO detections in the $\sim 1$ arcmin$^2$ UDF-10 datacube exposed for $\sim 30$ h (bottom row in Figure 5.1), with (a,c) non-compactness $\leq 1$ and (b) flatness $\geq 10$. The colors in (a) correspond to those in (c) but not to those in (b).

ran 3DMTO on. Specifically, we compare the 726 catalog sources[32] with the 1898 3DMTO detections which both fall within the 40.″0 angular separation from the MXDF center defined in Section 6.1.1. We additionally ensured that there were no sources that only contained absorption, as 3DMTO cannot directly detect those.

When cross-matching all 3DMTO detections within 1″ angular separation (○ marker in Figure 5.2), a purity of 97.95 % is reached.[33] However, the matched detections coincide with just 206 unique sources (11.08 % of detections), resulting in a completeness of only 28.37 %. There were also 39 3DMTO detections unmatched (2.05 %), corresponding to the ⬡ marker in Figure 5.2.

Despite using a relatively high significance level of $\alpha = 5 \times 10^{-4}$, the low completeness yet high purity may hint towards 3DMTO being too strict. This *strictness* is attributable to an overestimation of the rejection boundary, presumably in large due to the overestimated local background level (Section 6.6).

In Section 5.1 we defined the recall to be the ratio of LAEs recovered by 3DMTO over the number of LAEs in the BA23 catalog (after selection cuts). Figure 6.6 shows the recall and LAE counts as a function of $\mathrm{EW}_0(\mathrm{Ly}\alpha)$, as the equivalent width is the quantity used to select LAEs. We also explore a wider range of cross-match tolerances to see how big an effect the fiducial angular ($< 1.''0$) and spectral ($V_{\mathrm{Ly}\alpha}^{\mathrm{BA23}} \pm 685\,\mathrm{km\,s^{-1}}$) limits respectively have on our analysis in Chapter 5.

For all cross-matching limits, the recall initially trends upwards until $\mathrm{EW}_0(\mathrm{Ly}\alpha) \gtrsim -100$ Å where it precipitously drops and rises before dropping again after $\mathrm{EW}_0(\mathrm{Ly}\alpha) \lesssim -150$ Å. Thereafter, the recall settles around 30 %, fluctuating by roughly ±5 % for the remaining largely negative $\mathrm{EW}_0(\mathrm{Ly}\alpha)$ sample. This drop in recall at lower equivalent widths (LAEs bright in Ly$\alpha$) is unexpected, as one would intuitively expect brighter signal to be easier to detect. However, this is in line with the priorly established strictness of 3DMTO, and visual inspection of BA23 catalog LAEs in Figure 5.2 shows that many LAEs with large markers (indirectly indicating bright LAEs) are without a 3DMTO counterpart cross-match or detection.

To study the impact of the cross-match, we explore permutations of the following cross-matching limits: we consider spatially the fiducial 1″ and half that 0.″5, and along the spectral direction velocity offsets of $3\sigma$ and $10\sigma$ in addition to the fiducial $5\sigma$ velocity offset (Section 6.1.3). The isolation of the LAEs with respect to any 3DMTO detection already indicates that increasing the cross-matching radius should not affect the recall for these bright LAEs. Figure 6.6 confirms this suspicion, as below $\mathrm{EW}_0(\mathrm{Ly}\alpha) \sim -70$ Å the recall

[32] This number includes sources for which the reference spectrum came from the UDF-10 or MOSAIC datacubes. This impacts the completeness, because sources which where only detectable through emission observed within the wavelength coverage of the sodium filter (Figure 5.4) cannot be detected by 3DMTO in the MXDF datacube. However, if we limit the catalog to the MXDF datacube only, the purity drops to $\sim 91.57$ % (other quantities not as affected) because 3DMTO detects sources with reference spectra from the other datacubes through emission outside of the sodium filter's wavelength coverage which can now not be matched to a catalog source.

[33] Restricting the cross-match to 0.″2 angular separation (roughly one resolution element) still yields 90.20 % purity.

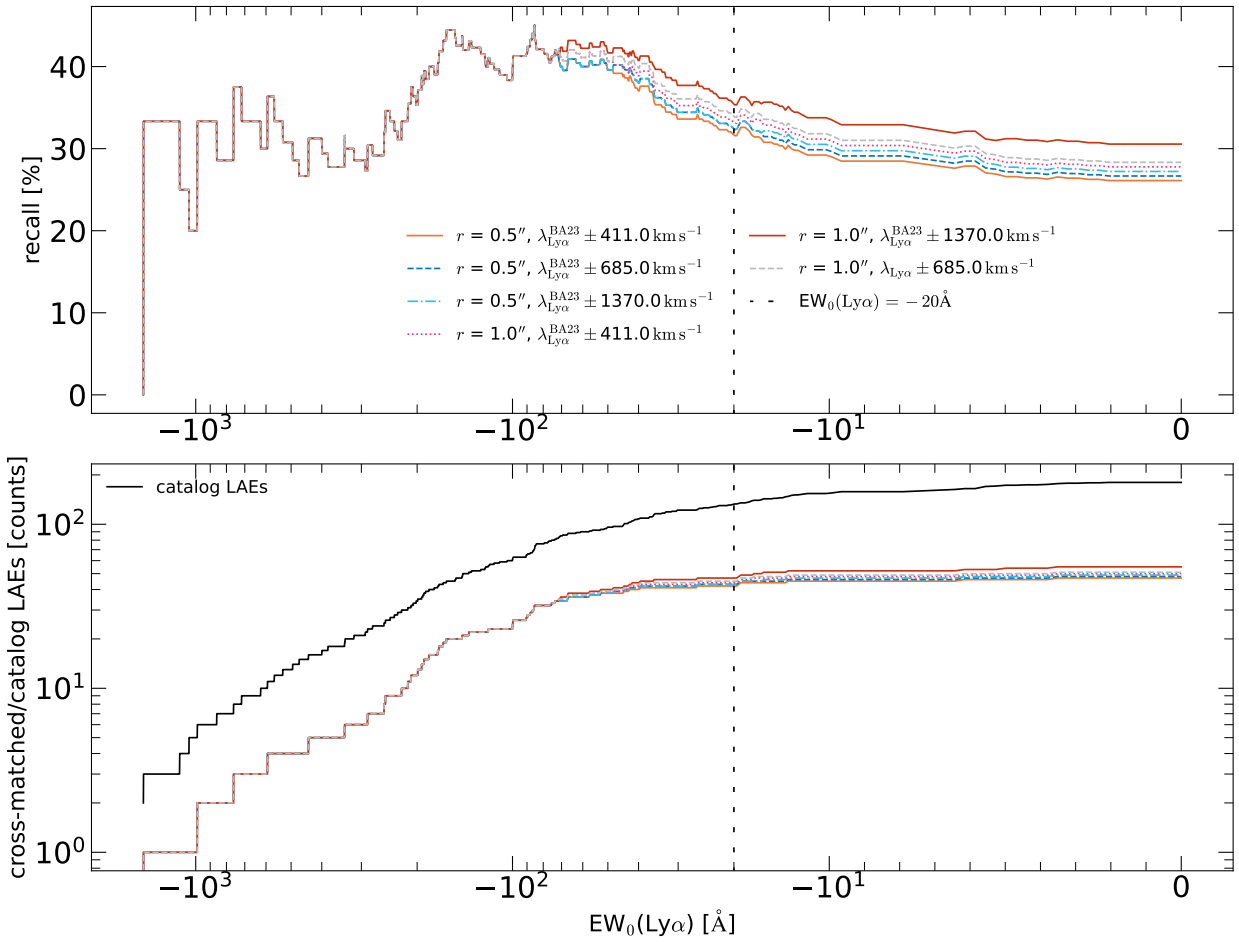


Figure 6.6: *Top*: the recall vs. $EW_0(Ly\alpha)$ for the cross-match between 3DMTO Ly$\alpha$ detections and BA23 catalog LAEs for various cross-match limits. *Bottom*: the number of LAEs in the catalog (black solid line) and number of cross-matched Ly$\alpha$ emission features detected by 3DMTO as a function of $EW_0(Ly\alpha)$. The gray dashed and vertical black dashed line respectively indicate the fiducial cross-match and $< -20$ Å equivalent width cut used for the analysis in Chapter 5.

is the same for all considered cross-matching limits. For LAEs with $EW_0(Ly\alpha) \gtrsim -70$ Å, the recall of the alternative cross-matching limits are gradually split around the fiducial cross-matching limits' recall at less than approximately $\pm 3$ % deviation with respect to the fiducial limits for the faintest LAEs. Therefore, the cross-matching should not have a big influence on the analysis performed in Chapter 5.

### 6.8.3 False detections

Not every detection made by 3DMTO corresponds to a real emission feature, which we will refer to as a false detection. If we assume the BA23 catalog is 100 % complete, the 39 unmatched detections are false detections. This turns out to largely be the case, but fortunately they generally occupy a region of attribute space away from the bulk of real detections, as shown in Figure 6.7. Overall these detections contain significantly more voxels and flux, with some segmentations connected at low altitude($P$) covering the entire datacube along a projection. These may thus easily be identified and removed. However, the subset of unmatched detections with lower num_voxels coincide closer with the bulk of detections (leftmost column of Figure 6.7), but they generally have higher sparseness for the same number of voxels, indicating they are more porous. The easiest

way to identify these false detections seems to be in the $\log_{10}$(non-compactness) vs. $\log_{10}$(elongation) plane, which shows high correlation for the bulk of real detections that the false detections do not follow. However, the unmatched detections with low elongation and non-compactness also corresponds to the detected Ly$\alpha$, as seen in Figure 5.5.

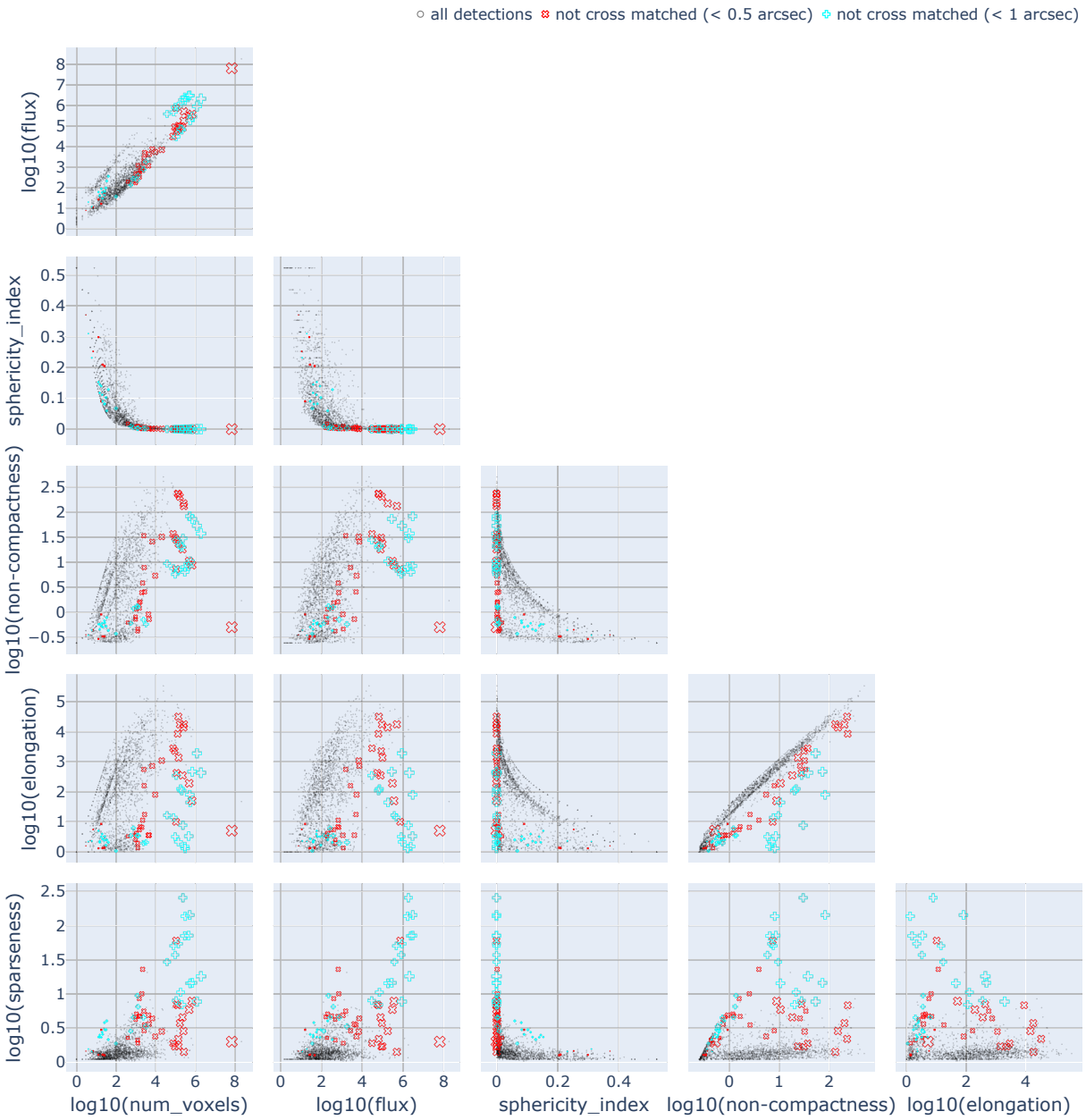


Figure 6.7: Scatter plot matrix of shape attributes for all matched 3DMTO detections (○ marker). The ✚ and ✖ represent 3DMTO detections not matched with any BA23 catalog source within 1″ and 0″.5 angular separation respectively. All ✚ are also included in ✖. The marked size scales with num_voxels.

Identifying regions in attribute space with false detections is easy with a known ground truth, but more sophisticated techniques like machine learning and/or dimensionality reduction are needed to infer more details about what population of detections/sources occupy which region of attribute space when no ground truth is available.

As MTO utilizes a statistical test for significance, data imperfections with respect to the assumptions

of the test lead to unpredictable false detections that are sporadically located in the datacube (Mary et al., 2020). This is what happens in the outer edges of the MXDF data (Section 6.1.1) where mosaicing introduces artifacts, but other artifacts like cosmic rays or skyline residuals also lead to false detections. Moreover, not all false detections are unmatched, with some 3DMTO detections just happening to have spatial centroids that coincide with a BA23 catalog source but have, e.g., unphysically high or low $\log_{10}$(num_voxels). These may be partially accounted for by introducing an additional requirement for a node to contain more voxels than for example the PSF, but this disregards if the number of voxels in the LSF and FSF directions are separately adhered to, but this could be addressed as well. This is currently not implemented as it will be data and/or resolution dependent, and may easily be performed as a post-processing step.

Another source of *false* detections is fragmentation, in which a source is split up into separate detections. The effect is severe in WEAVE LIFU datacubes, with zero sources for which the entire continuum appears segmented (Appendix C). It is noticeable to a lesser extent for the MXDF datacube but did not appear to be much of an issue at all in the 2D case (Teeninga et al., 2016). Presumably this can be attributed to the fluctuating variance in the spectral direction decreasing the power, and to skyline-subtraction residuals breaking up sources. This explains why it is comparatively worse for WEAVE LIFU datacubes with their significantly higher variance compared to the MXDF datacube, owing to the lower exposure time. To quantify this effect, Figure 6.8 shows that in WEAVE LIFU datacubes there are sources with more detections than there are emission features to detect. Something similar occurs for the MXDF datacube and is the reason only 209 sources were matched for 1898 detections, the majority of which disproportionately correspond to a few bright sources. These detections appear to largely be small localized detections, but some may extend up to several 100 Å, presumably originating from fragmentation between and around skyline residuals.

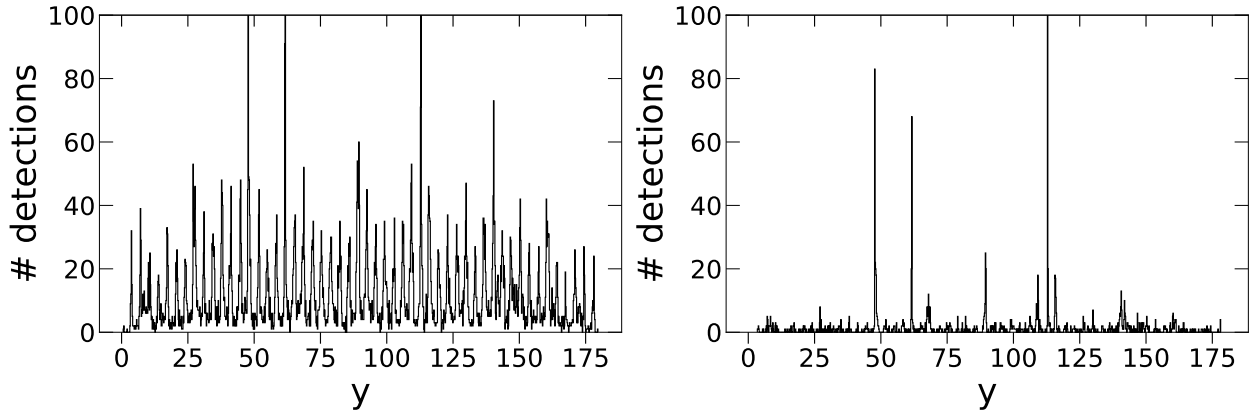


Figure 6.8: The number of detections for each $y$-column in WEAVE LIFU `stackcube_3006748.fit` (RED arm) for $\alpha = 10^{-1}$ (left) and $\alpha = 10^{-7}$ (right). The largest peaks coincide with bright sources with clearly detectable continuum.

The left panel of Figure 6.8 showcases that there appear to be increased detections at regular interval as a function of $y$-position. The effect is highly suppressed with decreasing $\alpha$ (right panel), and the detections likely correspond to the "confetti"-like detections for high $\alpha$ in the figures of Appendix C that also dissipate with decreasing $\alpha$. This effect is unique to the WEAVE LIFU datacubes, and presumably the peaks correspond to nodes which are dominated by voxels belonging to spaxels with three times the effective exposure time compared to their neighbors, owing to the dither strategy as described in the Section 6.3.1. The increased effective exposure time decreases the variance, correspondingly increasing the power. However, with decreasing $\alpha$, the S/N contribution of voxels with three times the effective exposure time is no longer enough to beat the ICDF$\chi^2(\alpha, \nu \sim 1)$. Furthermore, any $n$ surrounding voxels from descendant nodes – which are at lower effective exposure times, and therefore comparatively lower S/N – are unlikely to contribute enough S/N to beat the ICDF$\chi^2(\alpha, \nu = n)$. Moreover, because the neighboring spaxels might be identical and therefore

connected, the number of degrees of freedom quickly grows, increasing the ICDF$\chi^2(\alpha, \nu \gg 1)$ even more. Therefore, the varying exposure time should not be a limiting factor, as the ICDF$\chi^2$ mitigates these detections for sensibly low values of $\alpha$.

## 6.9 Performance

The main goal of this thesis was to apply and examine MTO for 3D IFU data, but having a handle on the expected time it takes to process a datacube is important to know if 3DMTO can be viable in general use.

In Section 6.2.2, 3DMTO was run 16 different times using 16 different significance levels, all of which were timed. The WEAVE LIFU `stackcube_3006749.fit` (BLUE arm) contained 158x181x1900 $\sim 5 \times 10^7$ voxels ($\sim$ 0.22 GB). We performed these timings on a laptop with an *AMD Ryzen 7 5825U* CPU at 2.00 GHz base up to 4 GHz boost, and 32 GB of RAM.

The memory was just enough to avoid having to write data to disk at this datacube size, indicative of suboptimal memory scaling (Carlinet & Geraud, 2014) for the max-tree algorithm by Berger et al., 2007 implemented in Higra. Nonetheless, Carlinet and Geraud did suggest that Berger et al.'s max-tree algorithm is appropriate for floating point data on memory limited systems. Carlinet and Geraud also stated that parallel-merging algorithms of subtrees from subsets of the data become inefficient due to the exponential complexity scaling with intensity levels, but since then work by Moschini et al., 2018 avoids this issue by merging the subtrees based on intensity instead; and more recently, Gazagnes and Wilkinson, 2021 used a distributive-memory approach to combat this limitation. Regardless of whether these approaches prove beneficial for 3DMTO, code optimizations (e.g., improved memory management) are warranted throughout the program.

The timings considered per segment, as well as the accumulated total runtime of 3DMTO, are presented in Table 6.1. The timings for each segment remain consistent across runs, although the first run ($\alpha = 10^{-1}$)

Table 6.1: Runtime performance of (segments of) 3DMTO in seconds, for a sub-cube from WEAVE LIFU `stackcube_3006749.fit` (BLUE arm) containing $\sim 5 \times 10^7$ voxels. The numbers correspond to the mean $\pm$ standard deviation of the 15 times (first run excluded) 3DMTO was run for Section 6.2.2.

| 3DMTO segment | elapsed time [s] |
|---|---|
| create max-tree | $58.8 \pm 0.6$ |
| determining objects | $98 \pm 4$ |
| compute attributes | $40 \pm 2$ |
| generate visualization | $10 \pm 1$ |
| total runtime | $208 \pm 4$ |

took $\sim$25 % longer in the first three segments and has therefore been omitted as an outlier. It is unknown why the first run took considerably longer. An unlikely possibility is the increased number of detections at such a high $\alpha$ increasing the required compute, but no trend is observed for the remaining datasets at lower significance levels. Moreover, the max-tree creation, which is independent of $\alpha$ and utmost consistent for all other runs, took 75.59 s compared to the 58.8 s average. A more likely possibility is the CPU clock boosting up overtime, and conceivably not a caching issue as the process is terminated between each run.

The max-tree creation is most consistent, as it is the only segment that does not change between runs. For the same datacube, the other segments are all affected by $\alpha$, as increasing $\alpha$ decreases the detection limit, thereby increasing the number of detections. Which could affect the computation time for each segment after and including "determining objects", but no trend with $\alpha$ is observed. This consistency is inline with prior studies using MTO (see e.g., Teeninga et al., 2016; Haigh et al., 2021).

To compare against the full extent of the MXDF datacube, the memory of the laptop was insufficient. The MXDF datacube contained over an order of magnitude more voxels (470x470x3721 $\sim 8 \times 10^8$ voxels,

$\sim 3.3$ GB), and required upwards of $\sim 350$ GB of memory. Therefore, we ran the MXDF datacube 3DMTO on the *Norma 3* computer cluster at the Kapteyn institute of the University of Groningen, The Netherlands. The total runtime was $\sim 50$ min, roughly half of which was spent in the "determining objects" segment, with the other half roughly evenly split between "create max-tree" and "compute attributes". The "generate visualization" step has comparatively insignificant runtime.

# 7 Summary

Even after the recent expeditious advancements in terms of LAE observability, the number of Ly$\alpha$ spectra with high enough resolution to resolve the line morphology remains limited. The WCCS will allow for *unbiased* serendipitous discovery of (faint) LAEs through lensing facilitated by the main target galaxy cluster. The exact number of LAEs that will be detected is unknown, but they will aid in studying the faint end of the LAE LF. By observing clusters in different regions of the sky, the WEAVE LIFU marginalizes over IGM sight-lines and will complement recent studies using MUSE located in the Southern Hemisphere.

MTObjects was originally devised for detection of diffuse and extended sources in 2D photometry and has been adapted for detection of LAEs in 3D IFU datacubes, termed 3DMTO. We departed from the constant background variance assumption by substituting it with the more authentic treatment provided by the IVAR datacube. Furthermore, for each detection, 3DMTO computes and catalogs descriptive attributes. The descriptive attributes are utilized to discern the sources underlying a detection.

We compared the detections of 3DMTO to the catalog of the MXDF by BA23, composed largely of sources detected using ORIGIN. Specifically, we assessed the performance of 3DMTO in detecting and recovering the flux of Ly$\alpha$. We only detect $\sim 30\,\%$ of LAEs through Ly$\alpha$, although limiting to doubly-peaked Ly$\alpha$ lines only, roughly doubles the recall. For all but one doubly-peaked profile, the more prominent red peak was found to bias the centroid, which was therefore offset with respect to the wavelength (redshift) reported by BA23. Except for this offset, the centroids of all Ly$\alpha$ detections were coincident with those of BA23 but show considerable scatter. Moreover, for the detected Ly$\alpha$, 3DMTO appears to woefully underestimate the flux and S/N, showing an increasing deficit with increasing flux. Presumably, estimating the local background level from altitude(parent($P$)) is too strict, and altitude($P_{\mathrm{anc}}$) would provide a more authentic local background estimation. The notion of strictness is corroborated by the 97.75 % purity attained in the MXDF, despite of the relatively high significance level $\alpha = 5 \times 10^{-4}$ used. Furthermore, it has been found that the attributes of a significant detection remain robust as a function of significance level $\alpha$.

The descriptive attributes show that Ly$\alpha$ detections are confined to a subset of the entire attribute space of all detections, which also shows a slight overlap with the false unmatched detections. It is also worth noting that there are incorrectly cross-matched detections due to, e.g., fragmentation or *significant* noise regions. Nonetheless, the distinctive yet localized region of attribute space in which Ly$\alpha$ is found shows promise for selective filtering of specific sources underlying a detection.

Despite the differences between the MXDF and WCCS datacubes, the attribute space of detections remain similar, albeit at decreased dynamic range for a WCCS datacube. However, WCCS datacubes show a much higher rate of fragmentation, which in addition to 3DMTO non-detections of Ly$\alpha$ and the ubiquitous flux deficit compared to the BA23 catalog suggest 3DMTO is unfit for reliable detection of LAEs in its current state.

## 7.1 Future work

To improve 3DMTO's detection efficiency, three main issues can be addressed.

Currently, the significance test assumes a worst-case scenario where the background level is chosen to be the first descendant node parent($P$), whereas the first significant ancestor $P_{\mathrm{anc}}$ should provide a more authentic description of the background level. Section 6.6 discusses how utilizing powerAlt($P$) instead of power($P$) will achieve this, but requires the distribution to test against be simulated.

Secondly, the background variance is maximally overestimated by using the IVAR datacube. Section 6.3 discussed how a more representative estimate of the background variance may be obtained from the surrounding voxels in descendant nodes, but care has to be taken that they are not biased by, e.g., a gradient, being too far from the signal, or low number counts.

Lastly, the max-tree only connects voxels at the same intensity level or higher than some threshold $t$. This means that sources are fragmented, i.e., galaxy continua may be broken up by absorption, and doublets (or doubly-peaked Ly$\alpha$) as well as voxels in the outskirts of an emission line affected by negative noise spikes are not connected. This disconnectedness can be mended by replacing the traditional connectivity with a mask-like connectivity, as discussed in Section 6.5. For separated emission lines or continuum, assuming that the signal is spatially coincident at peak intensity, only the spectral axis needs to be connected through clustering-based connectivity. Spatially, sources are already wrongfully merged through skyline residuals (see Section 6.8.1) and may need to be subject to contraction-based connectivity to be separated. To figure out which tree mask may be most appropriate, ground-truth-based segmentation masks together with source insertion and recovery experiments that take into account source segmentation have to be utilized (Haigh et al., 2021).

For applications not considered in this thesis, Section 6.5 discussed how 3DMTO can also be improved by incorporating the detection of absorption features. The datacube would have to undergo a black top-hat transformation, or the max-tree would have to be substituted for the Tree-of-Shapes. Both should be trivial to implement into the existing codebase, but likely come with increased computational costs. We do note that all aforementioned adjustments remain applicable also to the min-tree and Tree-of-Shapes.

It is also worth exploring to what extent the same flux deficit is observed for lines other than Ly$\alpha$, and more importantly which region of attribute space they would occupy. Despite the peculiar line morphology of Ly$\alpha$, current attributes look only at the unweighted 3D segmentation of a detection, which may not be appreciably different between emission lines for nearly unresolved sources.

Another interesting point is how the reference spectrum by ORIGIN compares with the spectrum 3DMTO recovers. For an emission line, 3DMTO will only segment voxels over the spectral extent of the line, so a descendant node that covers a larger spectral extent will have to be used in order to showcase the continuum. Which and if a descendant node is appropriate could for instance be obtained by testing if a current node is appreciably different from its parent node and if it conforms to the expected background distribution.

Moreover, visually inspecting the 3D segmentation of 3DMTO for detected Ly$\alpha$ lines also sheds more clarity on which flux is missed. It is additionally worth exploring if the attributes of the appropriate segmentation (e.g., those from BA23) appreciably differ from 3DMTO's.

To achieve and facilitate these scientific inferences, it may be useful to utilize an interactive max-tree exploration tool to visualize the segmentations (Westenberg et al., 2007).

# Acknowledgements

I would like to recognize that the presence of family and friends has provided an unspoken yet invaluable peace of mind throughout the duration of this thesis.
My appreciation goes out to my supervisors for being more patient with me than was probably appropriate: Prof. Dr. Scott Trager and Dr. Michael Wilkinson. Scott, together with his research group, provided an environment that made me feel at ease whether progress went smoothly or not, allowing for healthy discussion. For more implementation specific aspects of the thesis I had the pleasure to indulge in insightful conversations with Michael. I would further like to express my gratitude to Ph.D. student Mohammad Faezi for providing the initial code and sitting down with me on various occasions to help me with issues I ran into throughout the duration of this thesis.
Furthermore, the WEAVE team and BA23 are applauded for producing and providing datacubes (used in this thesis) succulent in astronomical information that were great fun to explore.
Lastly, I would also like to thank Prof. Dr. Reynier Peletier for being willing to serve as the 2nd examiner.

*Software*: `Higra` (Perret et al., 2019), `SciPy` (Virtanen et al., 2020), `NumPy` (Harris et al., 2020), `Astropy` (Astropy Collaboration et al., 2013, 2018, 2022), `Matplotlib` (Hunter, 2007), `Plotly` (Plotly Technologies Inc., 2015), `K3D` (Trzesiok, 2023), `Jupyter Notebook` (Kluyver et al., 2016), `WebPlotDigitizer` (Rohatgi, 2022)

# Bibliography


Arnoldus C. (2015). "A max-tree-based astronomical source finder". Master's thesis. Groningen, The Netherlands: University of Groningen, Bernoulli institute. eprint: https://fse.studenttheses.ub.rug.nl/id/eprint/13308.

Astropy Collaboration, Price-Whelan A. M., Sipőcz B. M., et al. (2018). "The Astropy Project: Building an Open-science Project and Status of the v2.0 Core Package". In: *The Astronomical Journal* 156.3, p. 123. DOI: 10.3847/1538-3881/aabc4f.

Astropy Collaboration, Price-Whelan A. M., Lim P. L., et al. (2022). "The Astropy Project: Sustaining and Growing a Community-oriented Open-source Project and the Latest Major Release (v5.0) of the Core Package". Version 6.0.1. In: *The Astrophysical Journal* 935.2, p. 167. DOI: 10.3847/1538-4357/ac7c74.

Astropy Collaboration, Robitaille T. P., Tollerud E. J., et al. (2013). "Astropy: A community Python package for astronomy". In: *Astronomy & Astrophysics* 558, A33. DOI: 10.1051/0004-6361/201322068.

Bacon R., Accardo M., Adjali L., et al. (2010). "The MUSE second-generation VLT instrument". In: *Ground-based and Airborne Instrumentation for Astronomy III*. Vol. 7735. SPIE, pp. 131–139. DOI: 10.1117/12.856027.

Bacon R., Brinchmann J., Conseil S., et al. (2023). "The MUSE Hubble Ultra Deep Field surveys: Data release II". In: *Astronomy & Astrophysics* 670, A4. DOI: 10.1051/0004-6361/202244187.

Bacon R., Conseil S., Mary D., et al. (2017). "The MUSE Hubble Ultra Deep Field Survey - I. Survey description, data reduction, and source detection". In: *Astronomy & Astrophysics* 608, A1. DOI: 10.1051/0004-6361/201730833.

Barger A. J., Cowie L. L., & Wold I. G. B. (2012). "A Flux-Limited Sample Of z ∼ 1 Ly$\alpha$ Emitting Galaxies in the Chandra Deep Field South". In: *The Astrophysical Journal* 749.2, p. 106. DOI: 10.1088/0004-637X/749/2/106.

Barkai J. A., Verheijen M. A. W., Talavera E., et al. (2023). "A comparative study of source-finding techniques in HI emission line cubes using SoFiA, MTObjects, and supervised deep learning". In: *Astronomy & Astrophysics* 670, A55. DOI: 10.1051/0004-6361/202244708.

Berger C., Geraud T., Levillain R., et al. (2007). "Effective Component Tree Computation with Application to Pattern Recognition in Astronomical Imaging". In: *2007 IEEE International Conference on Image Processing*. Vol. 4, IV–41 – IV–44. DOI: 10.1109/ICIP.2007.4379949.

Berkson J. (1951). "Why I Prefer Logits to Probits". In: *Biometrics* 7.4, pp. 327–339. DOI: 10.2307/3001655.

Bershady M. A. (2010). "3D spectroscopic instrumentation". In: *3D Spectroscopy in Astronomy*. Ed. by E. Mediavilla, F. Sánchez, J. Cepa-Nogué, et al. Vol. XVII. Canary Islands Winter School of Astrophysics. Cambridge: Cambridge University Press, pp. 87–125. DOI: 10.1017/CBO9780511770654.004.

Bertin E. & Arnouts S. (1996). "SExtractor: Software for source extraction." In: *Astronomy and Astrophysics Supplement Series* 117, pp. 393–404. DOI: 10.1051/aas:1996164.

Blaizot J., Garel T., Verhamme A., et al. (2023). "Simulating the diversity of shapes of the Lyman-$\alpha$ line". In: *Monthly Notices of the Royal Astronomical Society* 523.3, pp. 3749–3772. DOI: 10.1093/mnras/stad1523.

Boksenberg A. (1985). "The William Herschel telescope". In: *Vistas in Astronomy* 28, pp. 531–553. DOI: 10.1016/0083-6656(85)90074-1.

Bond N. A., Gawiser E., Guaita L., et al. (2012). "Evolution in the Continuum Morphological Properties of Ly$\alpha$-Emitting Galaxies from z = 3.1 to z = 2.1". In: *The Astrophysical Journal* 753.2, p. 95. DOI: 10.1088/0004-637X/753/2/95.

Bosilj P., Kijak E., & Lefèvre S. (2018). "Partition and Inclusion Hierarchies of Images: A Comprehensive Survey". In: *Journal of Imaging* 4.2, p. 33. DOI: 10.3390/jimaging4020033.

Bosman S. E. I., Kakiichi K., Meyer R. A., et al. (2020). "Three Ly$\alpha$ Emitting Galaxies within a Quasar Proximity Zone at z ∼ 5.8". In: *The Astrophysical Journal* 896.1, p. 49. DOI: 10.3847/1538-4357/ab85cd.

Bouwens R. J., Illingworth G., Ellis R. S., et al. (2022). "z ∼ 2–9 Galaxies Magnified by the Hubble Frontier Field Clusters. II. Luminosity Functions and Constraints on a Faint-end Turnover". In: *The Astrophysical Journal* 940.1, p. 55. DOI: 10.3847/1538-4357/ac86d1.

Breen E. J. & Jones R. (1996). "Attribute Openings, Thinnings, and Granulometries". In: *Computer Vision and Image Understanding* 64.3, pp. 377–389. DOI: 10.1006/cviu.1996.0066.

Bunker A. J., Saxena A., Cameron A. J., et al. (2023). "JADES NIRSpec Spectroscopy of GN-z11: Lyman-$\alpha$ emission and possible enhanced nitrogen abundance in a z = 10.60 luminous galaxy". In: *Astronomy & Astrophysics* 677, A88. DOI: 10.1051/0004-6361/202346159.

Cantalupo S., Pezzulli G., Lilly S. J., et al. (2018). "The large- and small-scale properties of the intergalactic gas in the Slug Ly$\alpha$ nebula revealed by MUSE Heii emission observations". In: *Monthly Notices of the Royal Astronomical Society* 483.4, pp. 5188–5204. DOI: 10.1093/mnras/sty3481.

Carlinet E. & Geraud T. (2014). "A Comparative Review of Component Tree Computation Algorithms". In: *IEEE Transactions on Image Processing* 23.9, pp. 3885–3895. DOI: 10.1109/tip.2014.2336551.

Comparat J., Kneib J.-P., Bacon R., et al. (2013). "Measuring galaxy [O ii] emission line doublet with future ground-based wide-field spectroscopic surveys". In: *Astronomy & Astrophysics* 559, A18. DOI: 10.1051/0004-6361/201322452.

Cowie L. L., Barger A. J., & Hu E. M. (2010). "Low-Redshift Ly$\alpha$ Selected Galaxies From GALEX Spectroscopy: a Comparison With Both UV-Continuum Selected Galaxies and High-Redshift Ly$\alpha$ Emitters". In: *The Astrophysical Journal* 711.2, p. 928. DOI: 10.1088/0004-637X/711/2/928.

Cruz-Matías I., Ayala D., Hiller D., et al. (2019). "Sphericity and roundness computation for particles using the extreme vertices model". In: *Journal of Computational Science* 30, pp. 28–40. DOI: 10.1016/j.jocs.2018.11.005.

Davis D., Gebhardt K., Cooper E. M., et al. (2021). "Detection of Lyman Continuum from 3.0 < z < 3.5 Galaxies in the HETDEX Survey". In: *The Astrophysical Journal* 920.2, p. 122. DOI: 10.3847/1538-4357/ac1598.

Davis D., Gebhardt K., Cooper E. M., et al. (2023a). "HETDEX Public Source Catalog 1—Stacking 50,000 Lyman Alpha Emitters". In: *The Astrophysical Journal* 954.2, p. 209. DOI: 10.3847/1538-4357/ace4c2.

Davis D., Gebhardt K., Cooper E. M., et al. (2023b). "The HETDEX Survey Emission-line Exploration and Source Classification". In: *The Astrophysical Journal* 946.2, p. 86. DOI: 10.3847/1538-4357/acb0ca.

Dayal P. & Ferrara A. (2012). "Ly$\alpha$ emitters and Lyman-break galaxies: dichotomous twins". In: *Monthly Notices of the Royal Astronomical Society* 421.3, pp. 2568–2579. DOI: 10.1111/j.1365-2966.2012.20486.x.

Dijkstra M. (2014). "Ly$\alpha$ Emitting Galaxies as a Probe of Reionisation". In: *Publications of the Astronomical Society of Australia* 31, e040. DOI: 10.1017/pasa.2014.33.

Dijkstra M., Prochaska J. X., Ouchi M., et al. (2019). *Lyman-alpha as an Astrophysical and Cosmological Tool. Swiss Society for Astrophysics and Astronomy*. Ed. by A. Verhamme, P. North, S. Cantalupo, et al. Vol. 46. Saas-Fee Advanced Course. Berlin, Heidelberg: Springer. DOI: 10.1007/978-3-662-59623-4.

Drake A. B., Garel T., Wisotzki L., et al. (2017). "The MUSE Hubble Ultra Deep Field Survey - VI. The faint-end of the Ly$\alpha$ luminosity function at 2.91 < z < 6.64 and implications for reionisation". In: *Astronomy & Astrophysics* 608, A6. DOI: 10.1051/0004-6361/201731431.

Eisenhauer F. (2010). "Science motivation for integral field spectroscopy and Galactic studies". In: *3D Spectroscopy in Astronomy*. Ed. by E. Mediavilla, F. Sánchez, J. Cepa-Nogué, et al. Vol. XVII. Canary Islands Winter School of Astrophysics. Cambridge: Cambridge University Press, pp. 158–199. DOI: 10.1017/CBO9780511770654.006.

Faezi M. H., Peletier R., & Wilkinson M. H. F. (2024). "Multi-Spectral Source-Segmentation using Semantically-Informed Max-Trees". In: *IEEE Access*. In press. DOI: 10.1109/ACCESS.2024.3403309.

Fluke C. J., Parrington L., Hegarty S., et al. (2017). "Sports Stars: Analyzing the Performance of Astronomers at Visualization-based Discovery". In: *Publications of the Astronomical Society of the Pacific* 129.975, p. 058009. DOI: 10.1088/1538-3873/aa5385.

Flury S. R., Jaskot A. E., Ferguson H. C., et al. (2022). "The Low-redshift Lyman Continuum Survey. II. New Insights into LyC Diagnostics". In: *The Astrophysical Journal* 930.2, p. 126. DOI: 10.3847/1538-4357/ac61e4.

Furtak L. J., Plat A., Zitrin A., et al. (2022). "A double-peaked Lyman-$\alpha$ emitter with a stronger blue peak multiply imaged by the galaxy cluster RXC J0018.5+1626". In: *Monthly Notices of the Royal Astronomical Society* 516.1, pp. 1373–1385. DOI: 10.1093/mnras/stac2169.

Garel T., Guiderdoni B., & Blaizot J. (2016). "Lyman-$\alpha$ emitters in the context of hierarchical galaxy formation: predictions for VLT/MUSE surveys". In: *Monthly Notices of the Royal Astronomical Society* 455.4, pp. 3436–3452. DOI: 10.1093/mnras/stv2467.

Gazagnes S., Chisholm J., Schaerer D., et al. (2020). "The origin of the escape of Lyman $\alpha$ and ionizing photons in Lyman continuum emitters". In: *Astronomy & Astrophysics* 639, A85. DOI: 10.1051/0004-6361/202038096.

Gazagnes S., Koopmans L. V. E., & Wilkinson M. H. F. (2021). "Inferring the properties of the sources of reionization using the morphological spectra of the ionized regions". In: *Monthly Notices of the Royal Astronomical Society* 502.2, pp. 1816–1842. DOI: 10.1093/mnras/stab107.

Gazagnes S. & Wilkinson M. H. F. (2021). "Distributed Connected Component Filtering and Analysis in 2D and 3D Tera-Scale Data Sets". In: *IEEE Transactions on Image Processing* 30, pp. 3664–3675. DOI: 10.1109/TIP.2021.3064223.

Gebhardt K., Cooper E. M., Ciardullo R., et al. (2021). "The Hobby-Eberly Telescope Dark Energy Experiment (HETDEX) Survey Design, Reductions, and Detections". In: *The Astrophysical Journal* 923.2, p. 217. DOI: 10.3847/1538-4357/ac2e03.

Ghamisi P., Dalla Mura M., & Benediktsson J. A. (2015). "A Survey on Spectral-Spatial Classification Techniques Based on Attribute Profiles". In: *IEEE Transactions on Geoscience and Remote Sensing* 53.5, pp. 2335–2353. DOI: 10.1109/TGRS.2014.2358934.

Giallongo E., Grazian A., Fiore F., et al. (2015). "Faint AGNs at z > 4 in the CANDELS GOODS-S field: looking for contributors to the reionization of the Universe". In: *Astronomy & Astrophysics* 578, A83. DOI: 10.1051/0004-6361/201425334.

Ginolfi M., Piconcelli E., Zappacosta L., et al. (2022). "Detection of companion galaxies around hot dust-obscured hyper-luminous galaxy W0410-0913". In: *Nature Communications* 13.1, p. 4574. DOI: 10.1038/s41467-022-32297-x.

Greenland S., Senn S. J., Rothman K. J., et al. (2016). "Statistical tests, P values, confidence intervals, and power: a guide to misinterpretations". In: *European Journal of Epidemiology* 31.4, pp. 337–350. DOI: 10.1007/s10654-016-0149-3.

Gronke M., Dijkstra M., Trenti M., et al. (2015). "Connecting faint-end slopes of the Lyman $\alpha$ emitter and Lyman-break galaxy luminosity functions". In: *Monthly Notices of the Royal Astronomical Society* 449.2, pp. 1284–1290. DOI: 10.1093/mnras/stv329.

Gu Y., Sun Z., Xiao X., et al. (2023). *Dual Structure-Preserving Image Filterings for Semi-supervised Medical Image Segmentation*. Tech. rep. DOI: 10.48550/arXiv.2312.07264.

Guaita L., Acquaviva V., Padilla N., et al. (2011). "Ly$\alpha$-Emitting Galaxies at z = 2.1: Stellar Masses, Dust, and Star Formation Histories from Spectral Energy Distribution Fitting". In: *The Astrophysical Journal* 733.2, p. 114. DOI: 10.1088/0004-637X/733/2/114.

Gurung-López S., Orsi Á. A., Bonoli S., et al. (2020). "Ly$\alpha$ emitters in a cosmological volume II: the impact of the intergalactic medium". In: *Monthly Notices of the Royal Astronomical Society* 491.3, pp. 3266–3289. DOI: 10.1093/mnras/stz3204.

Haigh C., Chamba N., Venhola A., et al. (2021). "Optimising and comparing source-extraction tools using objective segmentation quality criteria". In: *Astronomy & Astrophysics* 645, A107. DOI: 10.1051/0004-6361/201936561.

Harris C. R., Millman K. J., Walt S. J. van der, et al. (2020). "Array programming with NumPy". Version 1.26.4. In: *Nature* 585.7825, pp. 357–362. DOI: 10.1038/s41586-020-2649-2.

Hayes M. (2015). "Lyman Alpha Emitting Galaxies in the Nearby Universe". In: *Publications of the Astronomical Society of Australia* 32, e027. DOI: 10.1017/pasa.2015.25.

Hayes M., Schaerer D., Östlin G., et al. (2011). "On the Redshift Evolution of the Ly$\alpha$ Escape Fraction and the Dust Content of Galaxies". In: *The Astrophysical Journal* 730.1, p. 8. DOI: 10.1088/0004-637X/730/1/8.

Herenz E. C. (2016). "Detecting and understanding extragalactic Lyman $\alpha$ emission using 3D spectroscopy". doctoralthesis. Universität Potsdam. URL: https://publishup.uni-potsdam.de/frontdoor/index/index/docId/10234.

— (2023). "Revisiting the emission line source detection problem in integral field spectroscopic data". In: *Astronomische Nachrichten* 344.5, e20220091. DOI: 10.1002/asna.20220091.

Herenz E. C. & Wisotzki L. (2017). "LSDCat: Detection and cataloguing of emission-line sources in integral-field spectroscopy datacubes". In: *Astronomy & Astrophysics* 602, A111. DOI: 10.1051/0004-6361/201629507.

Herenz E. C., Wisotzki L., Saust R., et al. (2019). "The MUSE-Wide Survey: A determination of the Lyman $\alpha$ emitter luminosity function at $3 < z < 6$". In: *Astronomy & Astrophysics* 621, A107. DOI: 10.1051/0004-6361/201834164.

Hill G. J., Lee H., MacQueen P. J., et al. (2021). "The HETDEX Instrumentation: Hobby-Eberly Telescope Wide-field Upgrade and VIRUS". In: *The Astronomical Journal* 162.6, p. 298. DOI: 10.3847/1538-3881/ac2c02.

Horne K. (1986). "An Optimal Extraction Algorithm for CCD Spectroscopy". In: *Publications of the Astronomical Society of the Pacific* 98.604, p. 609. DOI: 10.1086/131801.

Huang X., Fisher M., & Smith D. J. (2003). "An Efficient Implementation of Max Tree with Linked List and Hash Table". In: *7th International Conference on Digital Image Computing: Techniques and Applications, DICTA*. Ed. by C. Sun, H. Talbot, S. Ourselin, et al. Sydney, Australia: CSIRO Publishing, pp. 299–308. URL: https://ueaeprints.uea.ac.uk/id/eprint/23500/ (visited on 12/08/2023).

Hunter J. D. (2007). "Matplotlib: A 2D Graphics Environment". Version 3.8.4. In: *Computing in Science & Engineering* 9.3, pp. 90–95. DOI: 10.1109/MCSE.2007.55.

Husemann B., Jahnke K., Sánchez S. F., et al. (2013). "CALIFA, the Calar Alto Legacy Integral Field Area survey: II. First public data release". In: *Astronomy & Astrophysics* 549, A87. DOI: 10.1051/0004-6361/201220582.

Iani E., Caputi K. I., Rinaldi P., et al. (2023). *MIDIS. JWST NIRCam and MIRI unveil the stellar population properties of Ly$\alpha$-emitters and Lyman-Break galaxies at $z \sim 3-7$*. Tech. rep. DOI: 10.48550/arXiv.2309.08515.

Jin S., Trager S. C., Dalton G. B., et al. (2024). "The wide-field, multiplexed, spectroscopic facility WEAVE: Survey design, overview, and simulated implementation". In: *Monthly Notices of the Royal Astronomical Society* 530.3, pp. 2688–2730. DOI: 10.1093/mnras/stad557.

Jones R. (1999). "Connected Filtering and Segmentation Using Component Trees". In: *Computer Vision and Image Understanding* 75.3, pp. 215–228. DOI: 10.1006/cviu.1999.0777.

Jurek R. (2012). "The Characterised Noise Hi Source Finder: Detecting Hi Galaxies Using a Novel Implementation of Matched Filtering". In: *Publications of the Astronomical Society of Australia* 29.3, pp. 251–261. DOI: 10.1071/AS11044.

Katz H., Rosdahl J., Kimm T., et al. (2023). *The Sphinx Public Data Release: Forward Modelling High-Redshift JWST Observations with Cosmological Radiation Hydrodynamics Simulations*. Tech. rep. DOI: 10.48550/arXiv.2309.03269.

Kazemi S. & Yatawatta S. (2013). "Robust radio interferometric calibration using the t-distribution". In: *Monthly Notices of the Royal Astronomical Society* 435.1, pp. 597–605. DOI: 10.1093/mnras/stt1347.

Kerutt J., Wisotzki L., Verhamme A., et al. (2022). "Equivalent widths of Lyman $\alpha$ emitters in MUSE-Wide and MUSE-Deep". In: *Astronomy & Astrophysics* 659, A183. DOI: 10.1051/0004-6361/202141900.

Kikuchihara S., Harikane Y., Ouchi M., et al. (2022). "SILVERRUSH. XII. Intensity Mapping for Ly$\alpha$ Emission Extending over 100-1000 Comoving Kpc around z ∼ 2-7 LAEs with Subaru HSC-SSP and CHORUS Data". In: *The Astrophysical Journal* 931.2, p. 97. DOI: 10.3847/1538-4357/ac69de.

Kikuta S., Ouchi M., Shibuya T., et al. (2023). "SILVERRUSH. XIII. A Catalog of 20,567 Ly$\alpha$ Emitters at z = 2-7 Identified in the Full-depth Data of the Subaru/HSC-SSP and CHORUS Surveys". In: *The Astrophysical Journal Supplement Series* 268.1, p. 24. DOI: 10.3847/1538-4365/ace4cb.

Kluyver T., Ragan-Kelley B., Pérez F., et al. (2016). *Jupyter Notebooks—a publishing format for reproducible computational workflows*. Version 7.1.3, pp. 87–90. DOI: 10.3233/978-1-61499-649-1-87.

Kobayashi M. A. R., Totani T., & Nagashima M. (2007). "Ly$\alpha$ Emitters in Hierarchical Galaxy Formation". In: *The Astrophysical Journal* 670.2, p. 919. DOI: 10.1086/522200.

Kong T. Y. & Rosenfeld A. (1989). "Digital topology: Introduction and survey". In: *Computer Vision, Graphics, and Image Processing* 48.3, pp. 357–393. DOI: 10.1016/0734-189X(89)90147-3.

Konno A., Ouchi M., Nakajima K., et al. (2016). "Bright and Faint Ends of Ly$\alpha$ Luminosity Functions at z = 2 Determined by the Subaru Survey: Implications for AGNs, Magnification Bias, and ISM H I Evolution". In: *The Astrophysical Journal* 823.1, p. 20. DOI: 10.3847/0004-637X/823/1/20.

Laursen P., Sommer-Larsen J., & Razoumov A. O. (2011). "Intergalactic Transmission and its Impact on the Ly$\alpha$ Line". In: *The Astrophysical Journal* 728.1, p. 52. DOI: 10.1088/0004-637X/728/1/52.

Leclercq F., Bacon R., Verhamme A., et al. (2020). "The MUSE Hubble Ultra Deep Field Survey - XIII. Spatially resolved spectral properties of Lyman $\alpha$ haloes around star-forming galaxies at z > 3". In: *Astronomy & Astrophysics* 635, A82. DOI: 10.1051/0004-6361/201937339.

Leclercq F., Bacon R., Wisotzki L., et al. (2017). "The MUSE Hubble Ultra Deep Field Survey - VIII. Extended Lyman-$\alpha$ haloes around high-z star-forming galaxies". In: *Astronomy & Astrophysics* 608, A8. DOI: 10.1051/0004-6361/201731480.

Lemaux B. C., Fuller S., Bradač M., et al. (2021). "The size and pervasiveness of Ly $\alpha$-UV spatial offsets in star-forming galaxies at z $\sim$ 6". In: *Monthly Notices of the Royal Astronomical Society* 504, pp. 3662–3681. DOI: 10.1093/mnras/stab924.

Lézoray O. (2016). "Complete lattice learning for multivariate mathematical morphology". In: *Journal of Visual Communication and Image Representation* 35, pp. 220–235. DOI: 10.1016/j.jvcir.2015.12.017.

Li W., Wang Z., Li L., et al. (2019). "Feature Extraction for Hyperspectral Images Using Local Contain Profile". In: *IEEE Journal of Selected Topics in Applied Earth Observations and Remote Sensing* 12.12, pp. 5035–5046. DOI: 10.1109/jstars.2019.2951437.

Liu C., Gebhardt K., Cooper E. M., et al. (2022). "The Active Galactic Nuclei in the Hobby-Eberly Telescope Dark Energy Experiment Survey (HETDEX). II. Luminosity Function". In: *The Astrophysical Journal* 935.2, p. 132. DOI: 10.3847/1538-4357/ac8054.

Loeb A. & Furlanetto S. R. (2013). "Surveys of High-Redshift Galaxies". In: *The First Galaxies in the Universe*. Princeton University Press. DOI: 10.1515/9781400845606.

Loomis R. A., Öberg K. I., Andrews S. M., et al. (2018). "Detecting Weak Spectral Lines in Interferometric Data through Matched Filtering". In: *The Astronomical Journal* 155.4, p. 182. DOI: 10.3847/1538-3881/aab604.

Lyman T. (1906). "The Spectrum of Hydrogen in the Region of Extremely Short Wave-Lengths". In: *The Astrophysical Journal* 23, p. 181. DOI: 10.1086/141330.

Maragos P. & Ziff R. (1990). "Threshold superposition in morphological image analysis systems". In: *IEEE Transactions on Pattern Analysis and Machine Intelligence* 12.5, pp. 498–504. DOI: 10.1109/34.55110.

Marques-Chaves R., Álvarez-Márquez J., Colina L., et al. (2020). "The discovery of the most UV–Ly $\alpha$ luminous star-forming galaxy: a young, dust- and metal-poor starburst with QSO-like luminosities". In: *Monthly Notices of the Royal Astronomical Society: Letters* 499.1, pp. L105–L110. DOI: 10.1093/mnrasl/slaa160.

Mary D., Bacon R., Conseil S., et al. (2020). "ORIGIN: Blind detection of faint emission line galaxies in MUSE datacubes". In: *Astronomy & Astrophysics* 635, A194. DOI: 10.1051/0004-6361/201937001.

Masias M., Freixenet J., Lladó X., et al. (2012). "A review of source detection approaches in astronomical images". In: *Monthly Notices of the Royal Astronomical Society* 422.2, pp. 1674–1689. DOI: 10.1111/j.1365-2966.2012.20742.x.

Matthee J., Sobral D., Hayes M., et al. (2021). "The X-SHOOTER Lyman $\alpha$ survey at z = 2 (XLS-z2) I: what makes a galaxy a Lyman $\alpha$ emitter?" In: *Monthly Notices of the Royal Astronomical Society* 505.1, pp. 1382–1412. DOI: 10.1093/mnras/stab1304.

Matthee J., Sobral D., Santos S., et al. (2015). "Identification of the brightest Ly$\alpha$ emitters at z = 6.6: implications for the evolution of the luminosity function in the reionization era". In: *Monthly Notices of the Royal Astronomical Society* 451.1, pp. 400–417. DOI: 10.1093/mnras/stv947.

Meillier C., Chatelain F., Michel O., et al. (2016). "SELFI: an object-based, Bayesian method for faint emission line source detection in MUSE deep field data cubes". In: *Astronomy & Astrophysics* 588, A140. DOI: 10.1051/0004-6361/201527724.

Mitchell P. D., Blaizot J., Cadiou C., et al. (2021). "Tracing the simulated high-redshift circum-galactic medium with Lyman $\alpha$ emission". In: *Monthly Notices of the Royal Astronomical Society*. DOI: 10.1093/mnras/stab035.

Monasse P. & Guichard F. (2000). "Fast computation of a contrast-invariant image representation". In: *IEEE Transactions on Image Processing* 9.5, pp. 860–872. DOI: 10.1109/83.841532.

Morales A. M., Mason C. A., Bruton S., et al. (2021). "The Evolution of the Lyman-alpha Luminosity Function during Reionization". In: *The Astrophysical Journal* 919.2, p. 120. DOI: 10.3847/1538-4357/ac1104.

Mori M. & Umemura M. (2006). "The evolution of galaxies from primeval irregulars to present-day ellipticals". In: *Nature* 440.7084, pp. 644–647. DOI: 10.1038/nature04553.

Moschini U., Meijster A., & Wilkinson M. H. F. (2018). "A Hybrid Shared-Memory Parallel Max-Tree Algorithm for Extreme Dynamic-Range Images". In: *IEEE Transactions on Pattern Analysis and Machine Intelligence* 40.3, pp. 513–526. DOI: 10.1109/TPAMI.2017.2689765.

Moschini U., Teeninga P., Wilkinson M. H., et al. (2014). "Towards better segmentation of large floating point 3D astronomical data sets: first results". In: *Proceedings of the 2014 conference on Big Data from Space (BiDS'14)*. Publications Office of the European Union, pp. 232–235. DOI: 10.2788/1823.

Mukherjee T., Zafar T., Nanayakkara T., et al. (2023). *Compact to extended Lyman-$\alpha$ emitters in MAGPI: strong blue peak emission at $z \gtrsim 3$*. Tech. rep. DOI: 10.48550/arXiv.2311.07019.

Naidu R. P., Matthee J., Oesch P. A., et al. (2022). "The synchrony of production and escape: half the bright Ly$\alpha$ emitters at z $\approx$ 2 have Lyman continuum escape fractions $\approx$50". In: *Monthly Notices of the Royal Astronomical Society* 510.3, pp. 4582–4607. DOI: 10.1093/mnras/stab3601.

Najman L. & Cousty J. (2014). "A graph-based mathematical morphology reader". In: *Pattern Recognition Letters*. Advances in Mathematical Morphology 47, pp. 3–17. DOI: 10.1016/j.patrec.2014.05.007.
Najman L. & Talbot H., eds. (2010). *Mathematical Morphology. From Theory to Applications*. ISTE Ltd and John Wiley & Sons, Inc. DOI: 10.1002/9781118600788.
Nakajima K., Fletcher T., Ellis R. S., et al. (2018). "The mean ultraviolet spectrum of a representative sample of faint z ∼ 3 Lyman alpha emitters". In: *Monthly Notices of the Royal Astronomical Society* 477.2, pp. 2098–2111. DOI: 10.1093/mnras/sty750.
Nakajima K., Ouchi M., Shimasaku K., et al. (2011). "Average Metallicity and Star Formation Rate of Ly$\alpha$ Emitters Probed by a Triple Narrowband Survey". In: *The Astrophysical Journal* 745.1, p. 12. DOI: 10.1088/0004-637X/745/1/12.
Nakane M., Ouchi M., Nakajima K., et al. (2023). *Ly$\alpha$ Emission at $z = 7 - 13$: Clear Ly$\alpha$ Equivalent Width Evolution Indicating the Late Cosmic Reionization History*. Tech. rep. DOI: 10.48550/arxiv.2312.06804.
Nguyen T. X., Chierchia G., Razim O., et al. (2021). "Object Detection With Component-Graphs in Multi-Band Images: Application to Source Detection in Astronomical Images". In: *IEEE Access* 9, pp. 156482–156491. DOI: 10.1109/ACCESS.2021.3128519.
Niemeyer M. L., Komatsu E., Byrohl C., et al. (2022). "Surface Brightness Profile of Lyman-$\alpha$ Halos out to 320 kpc in HETDEX". In: *The Astrophysical Journal* 929.1, p. 90. DOI: 10.3847/1538-4357/ac5cb8.
Osterbrock D. E. (1962). "The Escape of Resonance-Line Radiation from an Optically Thick Nebula." In: *The Astrophysical Journal* 135, p. 195. DOI: 10.1086/147258.
Östlin G. (2009). "What can Lyman $\alpha$ observations of nearby galaxies tell us about the high redshift Universe?" In: *New Astronomy Reviews*. Understanding Ly Emitters 53.3, pp. 44–46. DOI: 10.1016/j.newar.2009.04.004.
Ouchi M., Ono Y., & Shibuya T. (2020). "Observations of the Lyman-$\alpha$ Universe". In: *Annual Review of Astronomy and Astrophysics* 58.1, pp. 617–659. DOI: 10.1146/annurev-astro-032620-021859.
Ouchi M., Shimasaku K., Akiyama M., et al. (2008). "The Subaru/XMM-Newton Deep Survey (SXDS). IV. Evolution of Ly$\alpha$ Emitters from z = 3.1 to 5.7 in the 1 deg$^2$ Field: Luminosity Functions and AGN". In: *The Astrophysical Journal Supplement Series* 176.2, p. 301. DOI: 10.1086/527673.
Ouzounis G. K. & Wilkinson M. H. F. (2007). "Mask-Based Second-Generation Connectivity and Attribute Filters". In: *IEEE Transactions on Pattern Analysis and Machine Intelligence* 29.6, pp. 990–1004. DOI: 10.1109/TPAMI.2007.1045.
Partridge R. B. & Peebles P. J. E. (1967). "Are Young Galaxies Visible?" In: *The Astrophysical Journal* 147, p. 868. DOI: 10.1086/149079.
Perret B., Chierchia G., Cousty J., et al. (2019). "Higra: Hierarchical Graph Analysis". Version 0.6.8. In: *SoftwareX* 10, p. 100335. DOI: 10.1016/j.softx.2019.100335.
Perret B., Lefèvre S., Collet C., et al. (2010). "Connected Component Trees for Multivariate Image Processing and Applications in Astronomy". In: *2010 20th International Conference on Pattern Recognition*. ISSN: 1051-4651, pp. 4089–4092. DOI: 10.1109/ICPR.2010.994.
Piqueras L., Conseil S., Shepherd M., et al. (2019). "MPDAF–A Python Package for the Analysis of VLT/MUSE Data". In: *Astronomical Data Analysis Software and Systems XXVI*. Vol. 521. Astronomical Society of the Pacific. San Francisco, p. 545.
Planck Collaboration, Aghanim N., Akrami Y., et al. (2020). "Planck 2018 results - VI. Cosmological parameters". In: *Astronomy & Astrophysics* 641, A6. DOI: 10.1051/0004-6361/201833910.
Plotly Technologies Inc. (2015). *Collaborative data science*. Version 5.21.0. URL: https://plot.ly.
Pritchet C. J. (1994). "The Search For Primeval Galaxies". In: *Publications of the Astronomical Society of the Pacific* 106.704, p. 1052. DOI: 10.1086/133479.
Raiter A., Schaerer D., & Fosbury R. a. E. (2010). "Predicted UV properties of very metal-poor starburst galaxies". In: *Astronomy & Astrophysics* 523, A64. DOI: 10.1051/0004-6361/201015236.
Ribeiro B., Fèvre O. L., Paulino-Afonso A., et al. (2020). *The VIMOS Ultra-Deep Survey: the Ly$\alpha$ emission line morphology at $2 < z < 6$*. Tech. rep. DOI: 10.48550/arXiv.2007.01322.
Richard J., Bacon R., Blaizot J., et al. (2021a). *BlueMUSE: Project Overview and Science Cases*. Tech. rep. DOI: 10.48550/arXiv.1906.01657.
Richard J., Claeyssens A., Lagattuta D., et al. (2021b). "An atlas of MUSE observations towards twelve massive lensing clusters". In: *Astronomy & Astrophysics* 646, A83. DOI: 10.1051/0004-6361/202039462.
Rix H.-W., Hogg D. W., Boubert D., et al. (2021). "Selection Functions in Astronomical Data Modeling, with the Space Density of White Dwarfs as a Worked Example". In: *The Astronomical Journal* 162.4, p. 142. DOI: 10.3847/1538-3881/ac0c13.
Robertson J. G. (2013). "Quantifying Resolving Power in Astronomical Spectra". In: *Publications of the Astronomical Society of Australia* 30, e048. DOI: 10.1017/pasa.2013.26.
Rohatgi A. (2022). *WebPlotDigitizer*. Version 4.6. URL: https://automeris.io/WebPlotDigitizer.
Ronse C. (1990). "Why mathematical morphology needs complete lattices". In: *Signal Processing* 21.2, pp. 129–154. DOI: 10.1016/0165-1684(90)90046-2.
Runnholm A., Gronke M., & Hayes M. (2021). "The Lyman Alpha Spectral Database (LASD)". In: *Publications of the Astronomical Society of the Pacific* 133.1021, p. 034507. DOI: 10.1088/1538-3873/abe3ca.
Salembier P., Oliveras A., & Garrido L. (1998). "Antiextensive connected operators for image and sequence processing". In: *IEEE Transactions on Image Processing* 7.4, pp. 555–570. DOI: 10.1109/83.663500.
Salembier P. & Serra J. (1995). "Flat zones filtering, connected operators, and filters by reconstruction". In: *IEEE Transactions on Image Processing* 4.8, pp. 1153–1160. DOI: 10.1109/83.403422.

Salembier P. & Wilkinson M. H. F. (2009). "Connected Operators: A review of region-based morphological image processing techniques". In: *IEEE signal processing magazine* 26.6, pp. 136–157. DOI: 10.1109/MSP.2009.934154.
Samui S., Srianand R., & Subramanian K. (2009). "Understanding the redshift evolution of the luminosity functions of Lyman $\alpha$ emitters". In: *Monthly Notices of the Royal Astronomical Society* 398.4, pp. 2061–2068. DOI: 10.1111/j.1365-2966.2009.15245.x.
Scarlata C., Colbert J., Teplitz H. I., et al. (2009). "The Effect of Dust Geometry on the Ly$\alpha$ Output of Galaxies". In: *The Astrophysical Journal* 704.2, p. L98. DOI: 10.1088/0004-637X/704/2/L98.
Schaerer D. (2003). "The transition from Population III to normal galaxies: Ly$\alpha$ and He II emission and the ionising properties of high redshift starburst galaxies". In: *Astronomy & Astrophysics* 397.2, pp. 527–538. DOI: 10.1051/0004-6361:20021525.
Schechter P. (1976). "An analytic expression for the luminosity function for galaxies." In: *The Astrophysical Journal* 203, pp. 297–306. DOI: 10.1086/154079.
Serra J. (2022). "Mathematical Morphology". In: *Encyclopedia of Mathematical Geosciences*. Ed. by B. S. Daya Sagar, Q. Cheng, J. McKinley, et al. Encyclopedia of Earth Sciences Series. Cham: Springer, pp. 1–16. DOI: 10.1007/978-3-030-26050-7_22-2.
Smith A., Kannan R., Tacchella S., et al. (2022). "The physics of Lyman-$\alpha$ escape from disc-like galaxies". In: *Monthly Notices of the Royal Astronomical Society* 517.1, pp. 1–27. DOI: 10.1093/mnras/stac2641.
Sobral D., Matthee J., Darvish B., et al. (2018). "The nature of luminous Ly $\alpha$ emitters at $z \sim 2-3$: maximal dust-poor starbursts and highly ionizing AGN". In: *Monthly Notices of the Royal Astronomical Society* 477.2, pp. 2817–2840. DOI: 10.1093/mnras/sty782.
Sousa C. D. & Cortesão R. (2019). "Inertia Tensor Properties in Robot Dynamics Identification: A Linear Matrix Inequality Approach". In: *IEEE/ASME Transactions on Mechatronics* 24.1, pp. 406–411. DOI: 10.1109/TMECH.2019.2891177.
Spinoso D., Orsi A., López-Sanjuan C., et al. (2020). "J-PLUS: Unveiling the brightest end of the Ly$\alpha$ luminosity function at $2.0 < z < 3.3$ over 1000 deg$^2$". In: *Astronomy & Astrophysics* 643, A149. DOI: 10.1051/0004-6361/202038756.
Sternberg S. R. (1986). "Grayscale morphology". In: *Computer Vision, Graphics, and Image Processing* 35.3, pp. 333–355. DOI: 10.1016/0734-189X(86)90004-6.
Teeninga P., Moschini U., Trager S. C., et al. (2013). "Bi-variate statistical attribute filtering: A tool for robust detection of faint objects". In: *11th International Conference "Pattern Recognition and Image Analysis. New Information Technologies" (PRIA-11-2013)*, pp. 746–749.
Teeninga P., Moschini U., Trager S. C., et al. (2016). "Statistical attribute filtering to detect faint extended astronomical sources". In: *Mathematical Morphology — Theory and Applications* 1.1. DOI: 10.1515/mathm-2016-0006.
Thai T. T., Tuan-Anh P., Pello R., et al. (2023). "Probing the faint-end luminosity function of Lyman-alpha emitters at $3 < z < 7$ behind 17 MUSE lensing clusters". In: *Astronomy & Astrophysics* 678, A139. DOI: 10.1051/0004-6361/202346716.
Trager S. C. & The WEAVE Science Team (2019). "The WEAVE Survey Plan". WEAVE Survey Consortium. Review Version: (18/11/2019).
Trzesiok A. (2023). *K3D-tools/K3D-jupyter*. Version 2.16.1. URL: https://github.com/K3D-tools/K3D-jupyter.
Van Breukelen C., Jarvis M. J., & Venemans B. P. (2005). "The luminosity function of Ly$\alpha$ emitters at $2.3 < z < 4.6$ from integral-field spectroscopy". In: *Monthly Notices of the Royal Astronomical Society* 359.3, pp. 895–905. DOI: 10.1111/j.1365-2966.2005.08916.x.
Verhamme A., Garel T., Ventou E., et al. (2018). "Recovering the systemic redshift of galaxies from their Lyman alpha line profile". In: *Monthly Notices of the Royal Astronomical Society: Letters* 478.1, pp. L60–L65. DOI: 10.1093/mnrasl/sly058.
Verhamme A., Schaerer D., & Maselli A. (2006). "3D Ly$\alpha$ radiation transfer - I. Understanding Ly$\alpha$ line profile morphologies". In: *Astronomy & Astrophysics* 460.2, pp. 397–413. DOI: 10.1051/0004-6361:20065554.
Verhamme A., Orlitová I., Schaerer D., et al. (2015). "Using Lyman-$\alpha$ to detect galaxies that leak Lyman continuum". In: *Astronomy & Astrophysics* 578, A7. DOI: 10.1051/0004-6361/201423978.
Vieuville G. d. L., Bina D., Pello R., et al. (2019). "Faint end of the $z \sim$ 3-7 luminosity function of Lyman-alpha emitters behind lensing clusters observed with MUSE". In: *Astronomy & Astrophysics* 628, A3. DOI: 10.1051/0004-6361/201834471.
Vincent L. (1989). "Graphs and mathematical morphology". In: *Signal Processing*. Special Issue on Advances in Mathematical Morphology 16.4, pp. 365–388. DOI: 10.1016/0165-1684(89)90031-5.
Virtanen P., Gommers R., Oliphant T. E., et al. (2020). "SciPy 1.0: fundamental algorithms for scientific computing in Python". Version 1.13.0. In: *Nature Methods* 17.3, pp. 261–272. DOI: 10.1038/s41592-019-0686-2.
Wadell H. (1933). "Sphericity and Roundness of Rock Particles". In: *The Journal of Geology* 41.3, pp. 310–331. DOI: 10.1086/624040.
Wallis J. W., Miller T. R., Lerner C. A., et al. (1989). "Three-dimensional display in nuclear medicine". In: *IEEE Transactions on Medical Imaging* 8.4, pp. 297–230. DOI: 10.1109/42.41482.
Weinberger L. H., Kulkarni G., Haehnelt M. G., et al. (2018). "Lyman-$\alpha$ emitters gone missing: the different evolution of the bright and faint populations". In: *Monthly Notices of the Royal Astronomical Society* 479.2, pp. 2564–2587. DOI: 10.1093/mnras/sty1563.
Weiss L. H., Davis D., Gebhardt K., et al. (2024). "Absorption Troughs of Ly$\alpha$ Emitters in HETDEX". In: *The Astrophysical Journal* 962.2, p. 102. DOI: 10.3847/1538-4357/ad1b51.

Westenberg M. A., Roerdink J. B. T. M., & Wilkinson M. H. F. (2007). "Volumetric Attribute Filtering and Interactive Visualization Using the Max-Tree Representation". In: *IEEE Transactions on Image Processing* 16.12, pp. 2943–2952. DOI: 10.1109/TIP.2007.909317.

Wilkinson M. H. F. & Westenberg M. A. (2001). "Shape Preserving Filament Enhancement Filtering". In: *Medical Image Computing and Computer-Assisted Intervention – MICCAI 2001*. Ed. by W. J. Niessen & M. A. Viergever. Lecture Notes in Computer Science. Berlin, Heidelberg: Springer, pp. 770–777. DOI: 10.1007/3-540-45468-3_92.

Wise J. H. (2019). "Cosmic reionisation". In: *Contemporary Physics* 60.2, pp. 145–163. DOI: 10.1080/00107514.2019.1631548.

Wisotzki L., Bacon R., Brinchmann J., et al. (2018). "Nearly all the sky is covered by Lyman-$\alpha$ emission around high-redshift galaxies". In: *Nature* 562.7726, pp. 229–232. DOI: 10.1038/s41586-018-0564-6.

Wofford A., Leitherer C., & Salzer J. (2013). "Ly$\alpha$ Escape From z $\sim$ 0.03 Star-Forming Galaxies: the Dominant role of Outflows". In: *The Astrophysical Journal* 765.2, p. 118. DOI: 10.1088/0004-637X/765/2/118.

Yajima H., Li Y., Zhu Q., et al. (2014). "Escape of Ly$\alpha$ and continuum photons from star-forming galaxies". In: *Monthly Notices of the Royal Astronomical Society* 440.1, pp. 776–786. DOI: 10.1093/mnras/stu299.

Young N. & Evans A. N. (2003). "Psychovisually tuned attribute operators for pre-processing digital video". In: *IEE Proceedings - Vision, Image and Signal Processing* 150.5, pp. 277–286. DOI: 10.1049/ip-vis:20030768.

Zitrin A., Labbé I., Belli S., et al. (2015). "Ly$\alpha$ Emission From a Luminous z = 8.68 Galaxy: Implications for Galaxies as Tracers of Cosmic Reionization". In: *The Astrophysical Journal Letters* 810.1, p. L12. DOI: 10.1088/2041-8205/810/1/L12.

# A Power formula

The formula for the power can be expanded as follows,

$$\begin{aligned}
\text{power}(P) &= \sum_{x\in P}\left(\frac{f(x)-\text{altitude}(\text{parent}(P))}{\sigma(x)}\right)^2 \\
&= \sum_{x\in P}\left(\frac{f(x)^2}{\sigma(x)^2} - 2\cdot\frac{f(x)\cdot\text{altitude}(\text{parent}(P))}{\sigma(x)^2} + \frac{\text{altitude}(\text{parent}(P))^2}{\sigma(x)^2}\right) \\
&= \sum_{x\in P} f(x)^2\frac{1}{\sigma(x)^2} - 2\cdot\text{altitude}(\text{parent}(P))\sum_{x\in P} f(x)\frac{1}{\sigma(x)^2} + \text{altitude}(\text{parent}(P))^2\sum_{x\in P}\frac{1}{\sigma(x)^2} \\
&= \sum_{x\in P} f(x)^2\cdot\text{IVAR}(x) - 2\cdot\text{altitude}(\text{parent}(P))\sum_{x\in P} f(x)\cdot\text{IVAR}(x) \\
&\quad + \text{altitude}(\text{parent}(P))^2\sum_{x\in P}\text{IVAR}(x),
\end{aligned} \tag{A.1}$$

where $\text{IVAR}(x) = 1/\sigma(x)^2$ and $\text{altitude}(\text{parent}(P))$ is the constant background flux which can therefore be taken outside the summation.

# B 3D Segmentation examples

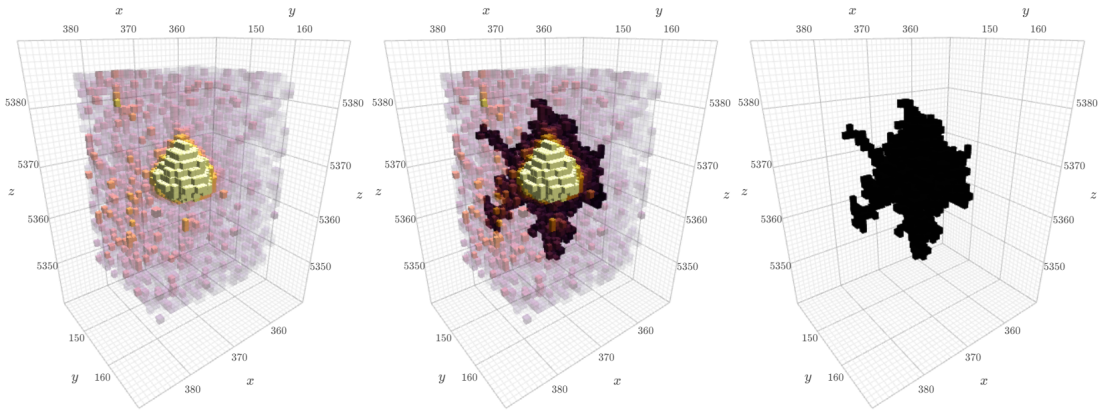

(a.I) Signal. (a.II) Signal + segmentation. (a.III) Segmentation.

(a) Segmentation of the strongest detected line. Signal linearly scaled and clipped between $0 - 2 \times 10^{-20}$ erg s$^{-1}$ cm$^{-2}$ Å.

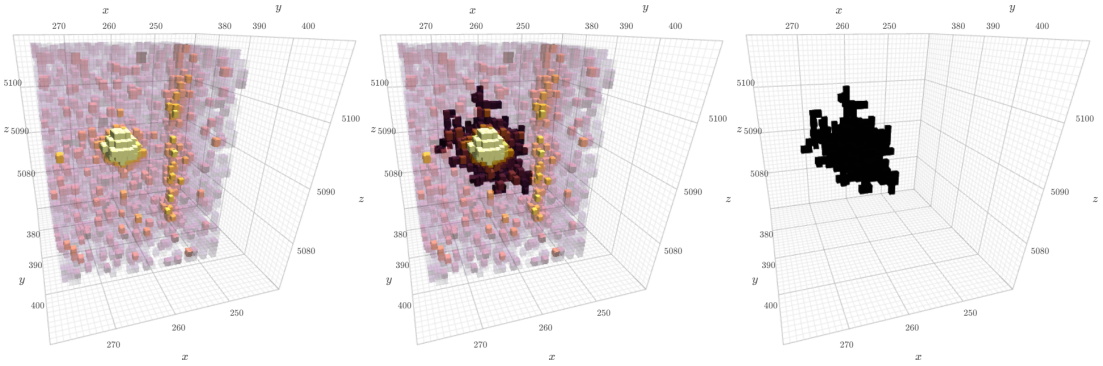

(b.I) Signal. (b.II) Signal + segmentation. (b.III) Segmentation.

(b) Segmentation of a random Ly$\alpha$ detection. Signal linearly scaled and clipped between $0 - 2 \times 10^{-20}$ erg s$^{-1}$ cm$^{-2}$ Å.

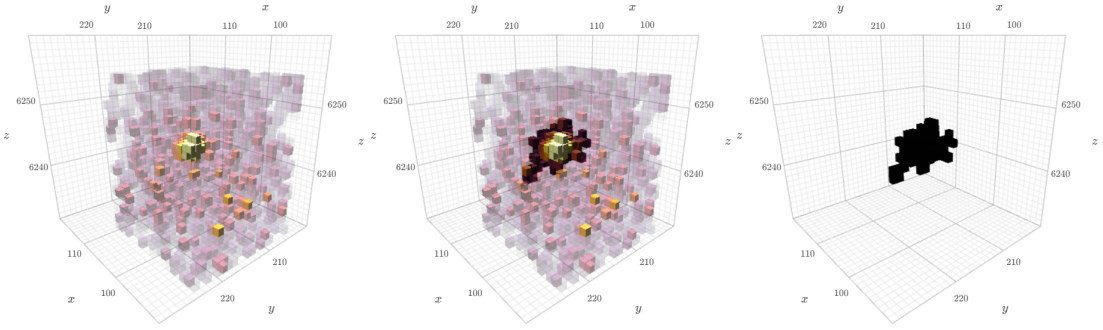

(c.I) Signal. (c.II) Signal + segmentation. (c.III) Segmentation.

(c) Segmentation of the faintest Ly$\alpha$ detection. Signal linearly scaled and clipped between $0 - 1.2 \times 10^{-20}$ erg s$^{-1}$ cm$^{-2}$ Å.

Figure B.1: 3D segmentations of the strongest, a random, and the faintest 3DMTO Ly$\alpha$ detections, with $x$ and $y$ indicating the spatial pixel coordinates and $z$ the wavelength in angstrom of the MXDF datacube. The signal is maximum intensity projected (Section 6.8.1).

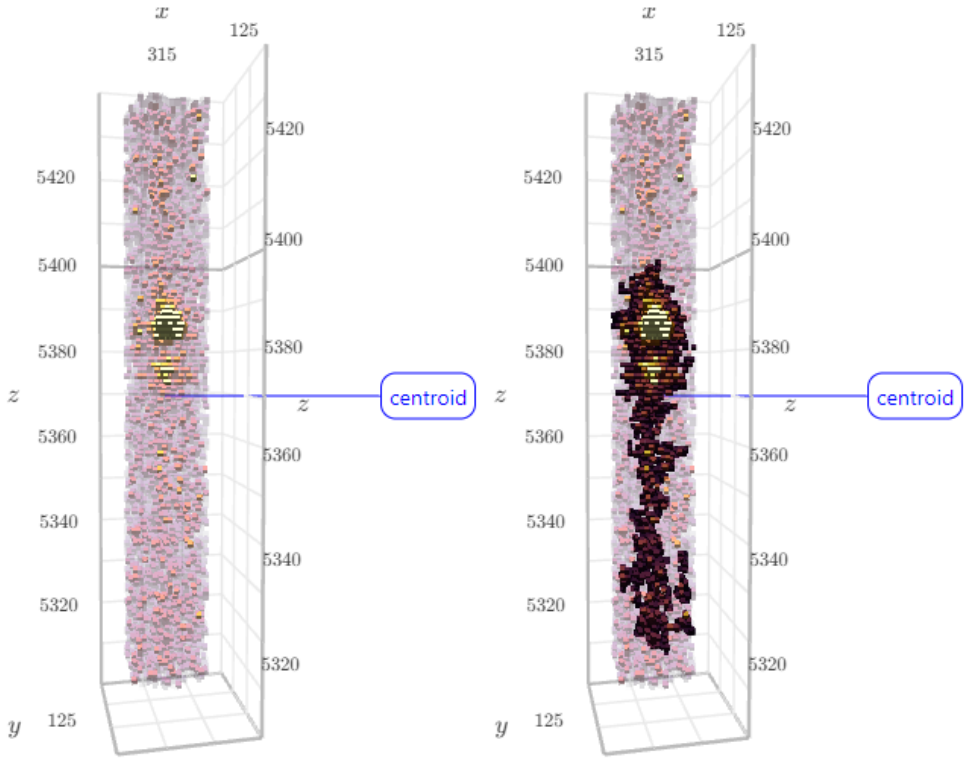


(a) Signal.

(b) Signal + segmentation.

(c) Segmentation.

Figure B.2: 3D visualization of the "peculiar" Ly$\alpha$ detection with $x$ and $y$ indicating the spatial pixel coordinates and $z$ the wavelength in angstrom of the MXDF datacube. The signal is linearly scaled, clipped between $0 - 1 \times 10^{-20}$ erg s$^{-1}$ cm$^{-2}$ Å, and maximum intensity projected (Section 6.8.1).

# C $\alpha$-dependence

Segmentations from the WEAVE LIFU `stackcube_3006749.fit` (BLUE arm) of the Abell 2142 galaxy cluster (Figure C.1) as a function of significance level $\alpha$. Note that the colors (different values of $\alpha$) are not

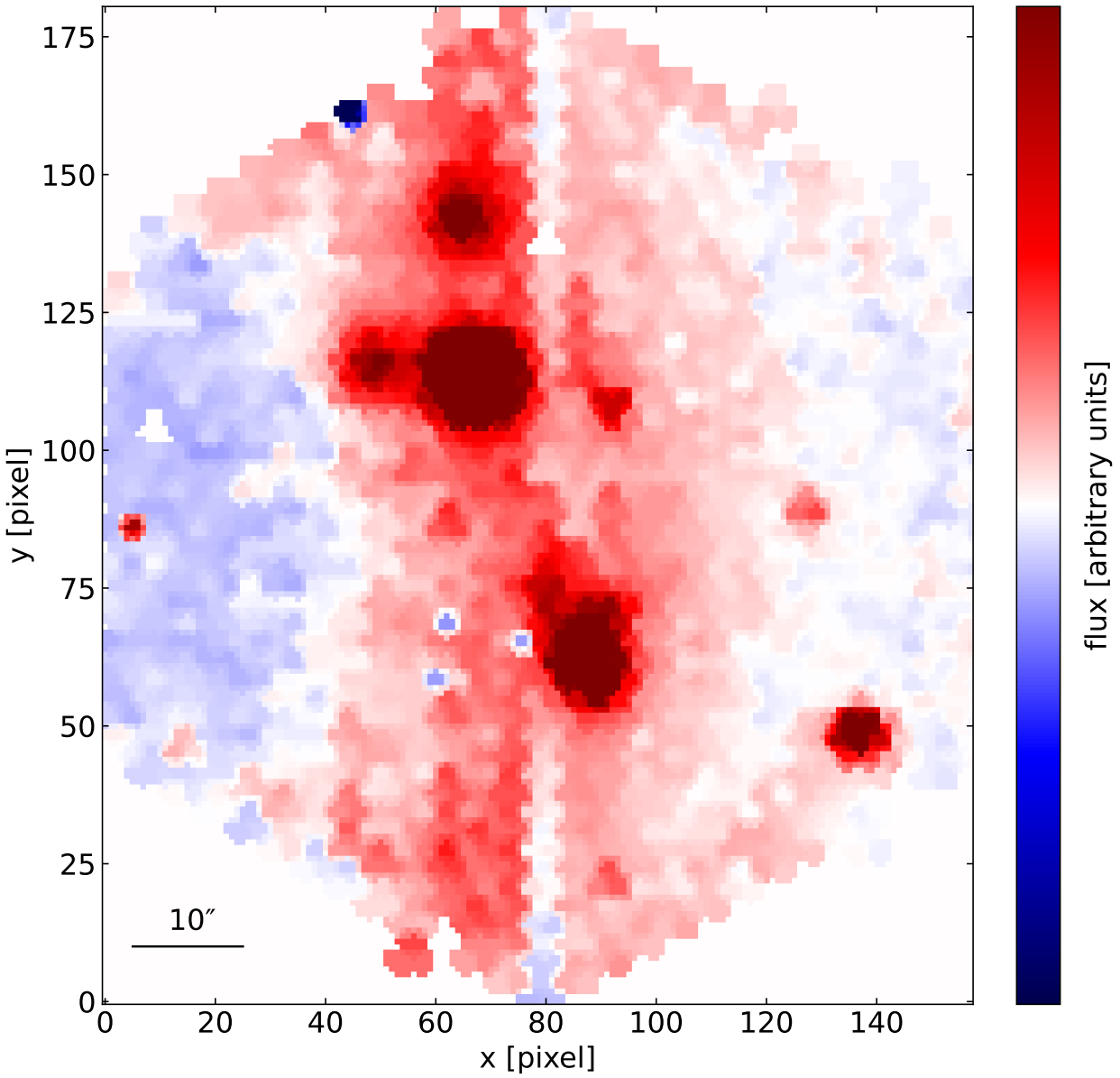


Figure C.1: Background subtracted white light image of WEAVE LIFU `stackcube_3006749.fit` (BLUE arm), obtained by collapsing the wavelength dimension. The dichotomous colorbar is centered on zero flux. Additionally, the flux is clipped at both extrema.

necessarily consistent for each panel within the same figure, but are consistent for the same value of $\alpha$ between all three Figures C.2–C.4. As expected, the number of (tentative "confetti"-like) detections decreases with decreasing $\alpha$.

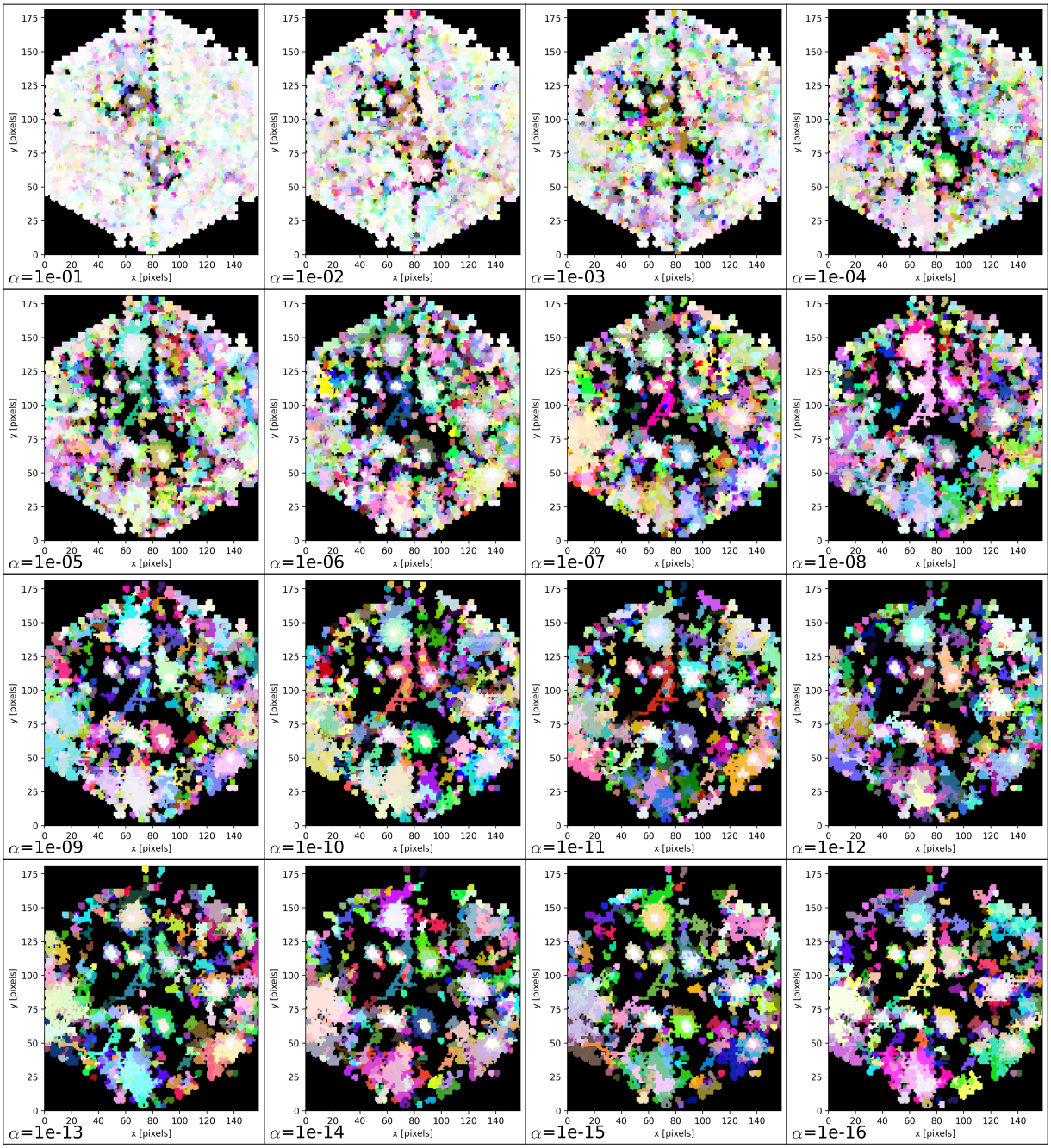


Figure C.2: MIP source segmentation in the x–y plane of WEAVE LIFU `stackcube_3006749.fit` (BLUE arm), for various values of the significance level $\alpha$.

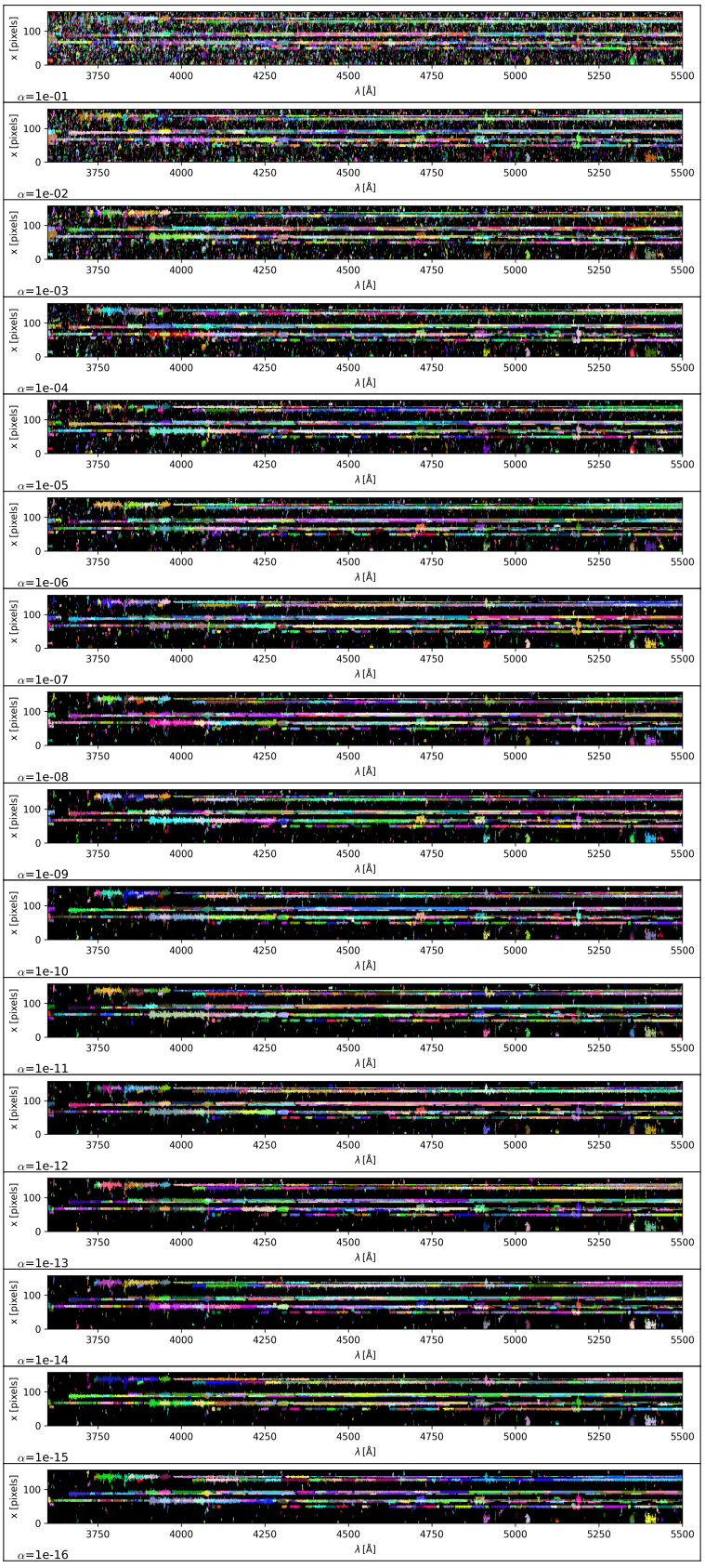


Figure C.3: MIP source segmentation in the x–$\lambda$ plane of WEAVE LIFU `stackcube_3006749.fit` (BLUE arm), for various values of the significance level $\alpha$.

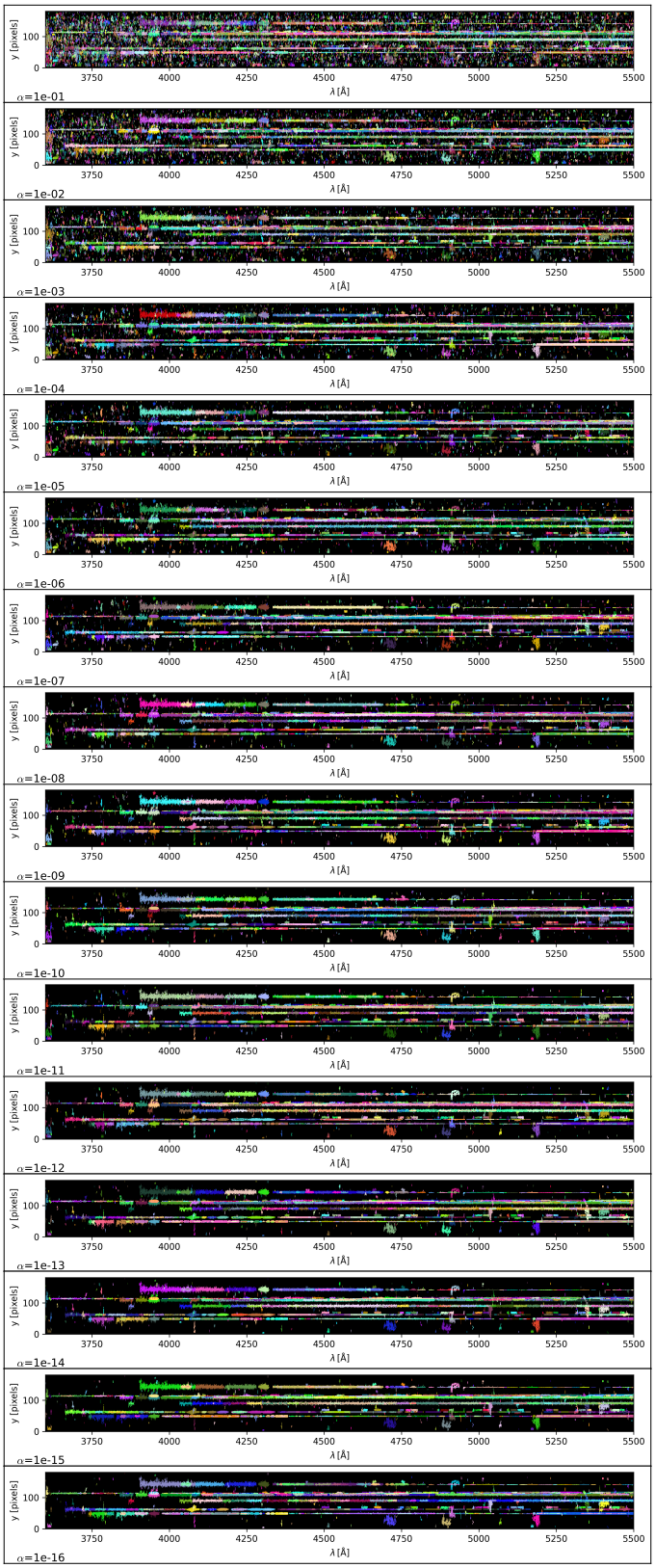


Figure C.4: MIP source segmentation in the y–$\lambda$ plane of WEAVE LIFU `stackcube_3006749.fit` (BLUE arm), for various values of the significance level $\alpha$.